



저작자표시-비영리-변경금지 2.0 대한민국

이용자는 아래의 조건을 따르는 경우에 한하여 자유롭게

- 이 저작물을 복제, 배포, 전송, 전시, 공연 및 방송할 수 있습니다.

다음과 같은 조건을 따라야 합니다:



저작자표시. 귀하는 원저작자를 표시하여야 합니다.



비영리. 귀하는 이 저작물을 영리 목적으로 이용할 수 없습니다.



변경금지. 귀하는 이 저작물을 개작, 변형 또는 가공할 수 없습니다.

- 귀하는, 이 저작물의 재이용이나 배포의 경우, 이 저작물에 적용된 이용허락조건을 명확하게 나타내어야 합니다.
- 저작권자로부터 별도의 허가를 받으면 이러한 조건들은 적용되지 않습니다.

저작권법에 따른 이용자의 권리는 위의 내용에 의하여 영향을 받지 않습니다.

이것은 [이용허락규약\(Legal Code\)](#)을 이해하기 쉽게 요약한 것입니다.

[Disclaimer](#)

물리학박사 학위 논문

**GROWTH AND CHARACTERIZATION OF MONOLAYER
TRANSITION METAL DICHALCOGENIDES:
TOWARDS ARTIFICIAL BROADBAND NONLINEAR 2-D
MATERIAL**

울산대학교 대학원
물리학과
LE CHINH TAM

**GROWTH AND CHARACTERIZATION OF MONOLAYER
TRANSITION METAL DICHALCOGENIDES:
TOWARDS ARTIFICIAL BROADBAND NONLINEAR 2-D
MATERIAL**

A thesis submitted in partial fulfillment of the requirement for the Degree of
Doctor of Philosophy to the Department of Physics,
University of Ulsan, Korea

By
LE CHINH TAM

November, 2017

**GROWTH AND CHARACTERIZATION OF MONOLAYER
TRANSITION METAL DICHALCOGENIDES:
TOWARDS ARTIFICIAL BROADBAND NONLINEAR 2-D
MATERIAL**

지도교수 김용수

이논문을 물리학박사 학위 논문으로 제출함

2017년 11월

울산대학교 대학원

물리학과

**GROWTH AND CHARACTERIZATION OF MONOLAYER
TRANSITION METAL DICHALCOGENIDES:
TOWARDS ARTIFICIAL BROADBAND NONLINEAR 2-D
MATERIAL**

**This certifies that the dissertation of
LE CHINH TAM is approved by**

Committee Chairman: Assoc. Prof. YONG SOO KIM

Committee Member: Assit. Prof. JOON IK JANG

Committee Member: Assit. Prof. SONNY RHIM

Committee Member: Prof. YOUNG HO UM

Committee Member: Prof. MAENG-JE SEONG

Department of Physics

University of Ulsan, Korea

November, 2017

LE CHINH TAM 의
물리학박사 학위 논문을 인준함

심사위원 김용수



심사위원 임성현

심사위원 장준익

인

심사위원 업영호

심사위원 성맹제

인

울산대학교 대학원

물리학과

2017년 11월

Contents:

List of Abbreviations	9
List of Figures.....	11
Acknowledgements	17
Abstract.....	18
Chapter 1: Introduction of monolayer TMDCs.....	20
1.1 History of development:	20
1.2 Structural properties:	20
1.3 Synthesis approaches of monolayer TMDCs:	22
1.3.1 Chemical vapor deposition (CVD) growth:	22
1.3.2 Pulsed laser deposition (PLD) assisted method:	24
1.4 Optical characterization of 2-D semiconductor:	24
1.4.1 Neutral exciton:.....	24
1.4.2 Charged excitons (trions) and biexciton:	27
1.4.3 Basic structural analysis of monolayer TMDCs	28
1.5 Nonlinear optical theory: second harmonic generation (SHG).....	28
1.5.1 Sum and difference frequency generation	30
1.5.2 Second harmonic generation:.....	31
1.5.3 Phase- matching:.....	32
1.5.4 Multiphoton absorption (MPA):	33
Chapter 2: Photosensitivity Study of Metal-Semiconductor-Metal Photodetector Based on Chemical Vapor Deposited Monolayer MoS₂	34
2.1 Introduction	34
2.1.1 Overview.....	34
2.1.2 Motivation.....	34
2.2 Experimental details.....	35
2.3 Result and discussion	36

2.3.1	Structural characterization of MoS ₂ film	36
2.3.2	Electrical characterization.....	39
2.4	Chapter summary	43
Chapter 3: Near bandgap second-order nonlinear optical characteristics of MoS₂ monolayer transferred on transparent substrates		44
3.1	Introduction:	44
3.1.1	Overview:.....	44
3.1.2	Motivation:.....	44
3.2	Results and discussion.....	45
3.3	Chapter summary	56
Chapter 4: Nonlinear optical characteristic of monolayered MoSe₂		57
4.1	Introduction	57
4.1.1	Overview.....	57
4.1.2	Motivation.....	58
4.2	Experimental methods.....	59
4.3	Result and discussion	59
4.4	Chapter summary	69
Chapter 5: Impact of selenium doping on resonant second harmonic generation in monolayer MoS₂.....		70
5.1	Introduction	70
5.1.1	Overview.....	70
5.1.2	Motivation.....	70
5.2	Result and discussion	72
5.2.1	The growth of monolayer MoS _{2(1-x)} Se _{2x} alloys:	72
5.3	Chapter summary:	85
Chapter 6: Preliminary results of broadband resonant second harmonic generation of artificially stacked heterostructures		86
6.1	Introduction:	86
6.1.1	Overview.....	86

6.1.2	Motivation.....	86
6.2	Result and discussion	88
6.3	Chapter summary:	99
	Conclusion:	101
	Publication:.....	103
A.	Peer reviewed papers.....	103
B.	International Conference Meetings	105
	References	110

List of Abbreviations

2D	Two-dimensional
2PA	Two-photon absorption
AFM	Atomic force microscope
CCD	Charge-coupled device
CMOS	Complementary metal-oxide semiconductor
CVD	Chemical vapor deposition
CVT	Chemical vapor transport
DFG	Difference frequency generation
DFT	Density functional theory
DI	Deionized
FET	Field-effect transistor
FWHM	Full width at half maximum
HU	Harmonics unit
IR	Infrared
LDA	Local-density approximation
LED	Light-emitting diode
LIDT	Laser-induced damage threshold
MBE	Molecular beam epitaxy
ME	Mechanical exfoliation
MPA	Multiphoton absorption
NBE	Near-band-edge
NIR	Near-infrared
Nd:YAG	Nd-doped yttrium aluminum garnet
NLO	Nonlinear optical
OM	Optical microscope
OPA	Optical parametric amplifier
OPG	Optical parametric generator
OPO	Optical parametric oscillator
PECVD	Plasma-enhanced chemical vapor deposition
PET	Polyethylene terephthalate

PL	Photoluminescence
PLD	Pulsed-laser deposition
PMMA	Polymethyl methacrylate
RMS	Root mean square
SCCM	Standard cubic centimeters per minute
SEM	Scanning electron microscope
SFG	Sum frequency generation
SHG	Second harmonic generation
TEM	Transmission electron microscope
TMDC	Transition metal dichalcogenide
UV	Ultraviolet

List of Figures

Figure 1-1: a) Atomic structure of monolayer MX_2 from side view and top view: hexagonal lattice composed of Mo/W atoms (yellow balls) and S/Se/Te (blue balls) b) schematic illustration of difference in atomic arrangement for two commonly observed phases 1T and 2H.....	21
Figure 1-2: Schematic illustration of chemical vapor deposition approaches using two hot-wall furnaces	23
Figure 1-3 OM images taken at the edge (left) and at the center (right) of a typical CVD-grown sample	24
Figure 1-4 Electronic band structure of typical monolayer TMDC (MoS_2) b) The first Brillouin zone of monolayer MoS_2 where different k points are denoted as M, K, K' c) Schematic picture of finer band structure at K/K' points showing two direct transition at valence band maxima (VBM) and conduction band minima (CBM). Red and blue lines represent the spin-up and spin down states. Red and blue arrows indicate two bright A and B excitons.	27
Figure 2-1 (a) Optical images of as-grown MoS_2 on 300 nm SiO_2/Si substrate at the edge and (b) center of the wafer with the existence of grain boundaries (white arrows). (c) Surface morphology of monolayer MoS_2 at the edge of wafer and (d) the height profile extracted from AFM image	37
Figure 2-2: Raman scattering (a) and PL spectrum (b) measured at the center of MoS_2 film.	38
Figure 2-3: (a) An optical image of MSM photodetector device. (b) Schematic illustration of device structure shown in (a). (c) I-V characteristic curves at various illuminated wavelengths. (d) The wavelength-dependence responsivity under -10 V bias.....	40
Figure 2-4 (a) I-V curve at various optical powers at 475 nm. (b) Photocurrent dependence of input optical power at constant bias voltage, -5 V and -10 V.....	41
Figure 2-5: (a) Photoresponse curve of the device. (b) Photoresponse measured at various applied bias voltage -1 V, -2 V and -3 V. (c) The response time is defined as the time when current increase from 10% to 90% of the photocurrent and the recovery time is defined as	

the period time when current decrease from 90% to 10% of the photocurrent as shown.....	42
Figure 3-1: OM images of transferred MoS ₂ on (a) fused silica, (b) flexible PET substrate and (c) as-grown MoS ₂ . Inset: SEM image of MoS ₂ on fused silica. (d) AFM image (scan range; 5 × 5 μm ²) and its thickness profile at the edge of the as-grown MoS ₂ flake. For clarity, the height profile is plotted across the boundary between the MoS ₂ flake and substrate.....	48
Figure 3-2: (a) Raman and (b) PL spectra of as-grown MoS ₂ on SiO ₂ /Si and both transferred samples (fused silica and PET substrates).	50
Figure 3-3: Broadband SHG responses of single-crystal quartz in transmission (dots) and reflection (circles) modes. The red plot overlaid on the transmission data is a bulk SHG fit that takes into account the spectral Maker fringe effect.	51
Figure 3-4: Broadband SHG response of (a) MoS ₂ on fused silica and (b) MoS ₂ on PET with two collection geometries. The red trace is a ratio of transmitted to reflected SHG.....	53
Figure 3-5: χ ² dispersions calculated based on transmission and reflection geometries from (a) MoS ₂ monolayer sheet on a fused silica substrate and (b) MoS ₂ monolayer sheet on a PET substrate. The red traces are the corresponding PL spectra from Fig. 3-2(b), confirming two-photon exciton resonance of SHG.	55
Figure 4-1: (a) Schematic drawing of two-step PLD growth mechanism PLD and (b) the furnace system for selenization of MoO ₃ film. (c) OM and (d) AFM image of monolayer MoSe ₂ flake from the marked region (red outlined square) in (c) and thickness profile (inset) on the SiO ₂ /Si substrate.....	61
Figure 4-2: (a) Normalized Raman spectrum and (b) photoluminescence spectrum of the monolayer MoSe ₂ flake. (c) Semi-log plot of the PL (red), showing A- and B-exciton levels along with lower-energy tail arising from bound excitons. The B-exciton PL (green) is modeled with a Lorentzian shape. The blue trace is the PL without the B-exciton contribution.	62
Figure 4-3: (a) Experimental setup for NLO study and (b) the azimuthal symmetry of monolayer MoSe ₂ as determined by SHG polarization dependence. Parallel (blue dots) components and perpendicular (red dots) components are shown with the corresponding fitting curves (solid traces).....	65

Figure 4-4 (a) Broadband $\chi(2)$ dispersion of the MoSe ₂ monolayer and (b) MoS ₂ monolayer with superimposed PL spectra (solid red traces). The major excitonic levels are indicated.	67
Figure 4-5: SHG power dependence of MoSe ₂ monolayer (white dots) and MoS ₂ monolayer (black dots) plotted on a log-log scale. The solid red lines are square-law fitting lines.....	69
Figure 5-1: (a) Optical microscopic image (scale bar is 30 μm) and (b) representative AFM image ($x = 0.45$). Normalized (c) Raman spectra and (d) PL spectra for monolayer alloys as a function of Se composition, x . For comparison, the data for PLD-assisted grown MoSe ₂ is plotted together (dark yellow curve).....	73
Figure 5-2: CMOS images of alloy flakes selected for the SHG study. The beam size is $\sim 100 \mu\text{m}$ in diameter as indicated by the circle.	74
Figure 5-3 (a) PL (circles) of monolayer alloy MoS ₂ (0.82)Se ₂ (0.18) with Gaussian fit curves to the A-exciton (blue traces), B-exciton (magenta trace), and trion (green trace) to produce the overall fit (brown trace). (b) A-exciton (squares) and B-exciton (circles) spectral position as a function of x . Also plotted is the energy separation (spin-orbit splitting) between the two exciton states (blue diamonds). Star dots are data from our previous publication regarding the PLD-assisted grown monolayer MoSe ₂	75
Figure 5-4 Room-temperature PL spectra of monolayer ternary alloys	76
Figure 5-5: (a) SHG experimental setup, (b) CMOS images of a targeted sample, and (c) polarization-dependent SHG through 60° rotation of monolayer MoS ₂ (1-x)Se _{2x} ($x=0.18$). Scattered symbols are experimental data and solid traces are corresponding fitting curves. .	78
Figure 5-6: Polarization-dependent SHG through a 60° rotation of MoS ₂ (1-x)Se _{2x} ($x = 0.3, 0.45, 0.62$) monolayers. The input wavelength was chosen where the SHG response is maximum. Scattered blue and red dots are experimental data for SHG which were parallel and perpendicular to the input polarization state of the fundamental beam, respectively. Solid traces are corresponding fitting curves.	78
Figure 5-7: SHG spectra (dotted traces) of monolayer alloys and corresponding room-temperature PL spectra (solid traces). Spectral positions of the A- and B-excitons are indicated. For comparison, SHG of PLD-assisted grown MoSe ₂ is plotted together.	82
Figure 5-8: (a) χ_{xxx2} dispersions of monolayer alloys with different Se compositions and (b)	

static χ^2 values as function of Se composition. The solid line is a theoretical prediction. ... 83

Figure 6-1: (a) OM image of a typical hetero-bilayer consisting of MoS_2 (top layer) and $\text{MoS}_{2(0.7)}\text{Se}_{2(0.3)}$ (bottom layer). (b) AFM image obtained from the red square in Fig.6-1(a) with the overlaid height profile. (c) Raman and (d) photoluminescence spectra acquired from this hetero-bilayer (black) and its constituent layers: MoS_2 (blue) and $\text{MoS}_{2(0.7)}\text{Se}_{2(0.3)}$ (red).89

Figure 6-2: (a) Energy-level diagram for SHG in monolayer TMDC. The dashed lines represent virtual states and the solid lines represent real states in momentum space; *A*- and *B*- exciton levels (red). (b) CMOS image of the hetero-bilayer. The arrows schematically represent the SHG fields of MoS_2 (blue), $\text{MoS}_{2(0.7)}\text{Se}_{2(0.3)}$ (red), and the hetero-bilayer (black), respectively. (c) SHG spectra (solid symbols) superimposed with the PL (solid traces) obtained from monolayer MoS_2 (bottom panel), monolayer $\text{MoS}_{2(0.7)}\text{Se}_{2(0.3)}$ (middle panel), and the hetero-bilayer (top panel). The dashed lines indicate the exciton resonances of the constituents. 91

Figure 6-3. (a) Wavelength-dependent SHG from the homo-bilayer overlaid with the PL spectrum, clearly showing the *A*- and *B*- exciton resonances. (b) Comparison of the SHG intensities between the homo-bilayer (black: $\text{MoS}_2/\text{MoS}_2$) and the hetero-bilayer (red: $\text{MoS}_{2(0.7)}\text{Se}_{2(0.3)}/\text{MoS}_2$). (c) Ratio between the SHG intensities of the two samples, displaying the improved performance of the heterobilayer. (d) Spin-orbit splitting as a function of Se doping concentration x in our previous publication.[150](e) Schematic illustration of three possible SHG enhancements in the hetero-bilayer via *AA*-, *BB*-, and *AB*-couplings. 93

Figure 6-4 Wavelength dependent SHG for monolayer (black trace)and homobilayer (red trace) MoS_2 95

Figure 6-5. (a) OM image of the hetero-trilayer comprised of three layers with different Se concentrations. (b) Schematic illustration of the trilayer showing stacking order. AFM images measured at areas marked by (c) the red square and (d) the blue square in (a), respectively. (e) Raman spectra of the hetero-trilayer and its constituent layers. (f) Room-temperature PL spectra of the hetero-trilayer and its constituent layers..... 96

Figure 6-6 (a) Wavelength-dependent SHG measured from the hetero-trilayer (purple) overlaid with the PL spectra from individual layers; monolayers $\text{MoS}_{2(1-x)}\text{Se}_{2x}$; $x=0$ (blue), 0.3 (red), 0.45 (black), and the hetero-trilayer (dark yellow). The spectral locations for the

resonance are indicated by the dashed lines of the corresponding color. (b) Comparison of the SHG efficiency of the two hetero-trilayers prepared with different stacking schemes; 1) $x = 0.45$ (black) and 2) $x = 0.62$ (red) in the third layer, whereas the bottom bilayers are identical in chemical composition, i.e., the hetero-bilayer ($\text{MoS}_{2(0.7)}\text{Se}_{2(0.3)}/\text{MoS}_2$). See SI for the latter case of the trilayer. Here, each SHG efficiency is scaled by that of the hetero-bilayer in **Fig. 6-3(b)**. 97

Figure 6-7: Wavelength-dependent SHG measured from the hetero-trilayer (pink) overlaid with the PL spectra from individual layers; monolayers $\text{MoS}_{2x}\text{Se}_{2(x-1)}$; $x=0$ (blue), 0.3 (red), 0.62 (black), and the hetero-trilayer (green). 99

List of Table

Table 1: Summary of A-exciton binding energy of monolayer TMDCs extracted from different experimental techniques.....	25
Table 2: Full width and half maximum of A- and B-exciton calculated from PL for different Se composition.....	80

Acknowledgements

First of all, I would like to express my deep gratitude to my supervisor, Professor Yong Soo Kim for the continuous support of my Ph.D. study and related research, for his helpful direction, encouragement, and patience. His guidance helped me in all the time of research and writing of this thesis.

I would like to express my gratitude to Professor Mae Se Jong and Mr. Yumin Shim for their tremendous assistance for optical characterization from the beginning to present.

My sincere thanks also go to Professor Joon Ik Jang, who provided me an opportunity to join his team at Binghamton University, and gave access to the laboratory and research facilities. Besides, I would like to appreciate the endless help from Dr. Daniel Clark, Dr. Felix Ouama. Without their valuable support, it would not be possible to finish this thesis.

I would like to thank all office clerks and Professors at the University of Ulsan, who have helped me and lectured me during my Ph.D. period.

I would also like to extend my thanks to my all lab members, Mrs. Nhu Thuy Ho, Mr. Anh Duc Nguyen, Mr. Jong Yun Won, Mr. Farman Ullah and Mr. Tahir Zeeshan. ..., it was so great sharing laboratory with all of you during last five years. Also, I thank all my friends here for all the fun and memorable moments we have had in Korea. In particular, I especially thank to Ms. Thanh Huong for her endless help during my study.

Last but not least, I would like to give special thanks to my beloved family for their inestimable love that has supported me spiritually throughout my study and my life in general.

Ulsan, November 2017

LE CHINH TAM

Abstract

Over the last few decades, the silicon-based technology has dominated in the industrial electronics market. However, in the recent decades ago, the advent of graphene, the first true 2D material, marked a historic point for potentially new-generation of electronics. Not long after that, the successive discoveries of different 2D materials including an insulator (hexagonal Boron Nitride), semiconductors (transition metal dichalcogenides TMDCs), metallic (graphene) provide a great chance to achieve extremely thin and light optoelectronic devices. In order to achieve the high performance optoelectronic, yielding 2D materials with remarkable quality is highly desirable. The essence of this work lies on growth technique that produces high quality 2D materials applicable to new-generation of 2D optoelectronic devices.

In this dissertation, monolayer TMDCs were chosen as subjects to study. In chapter 1, I will briefly introduce layer-dependent physical and structural properties monolayer TMDCs as well as the current synthesis approaches for growing monolayer TMDCs. I initially grew large-scale, highly optical quality monolayer TMDC using chemical vapor deposition method. Towards practical applications, the continuous monolayers MoS₂ were synthesized and its photoresponsibility was also characterized in order to fabricate competitive metal-semiconductor-metal photodetector in chapter 2.

An additional part of this dissertation will discuss the nonlinear optical characteristic of monolayer TMDCs towards design a broad and strong second harmonic susceptibility $\chi^{(2)}$ materials. Nonlinear properties theory will be mainly discussed in term of second harmonic generation. In chapter 3, nonlinear characteristics of transferred MoS₂ on the transparent substrate were studied in comparison with as-grown MoS₂ onto SiO₂/Si substrate, which could be applied to Fabry-Perót cavity in the laser technology. In chapter 4, another typical member of monolayer TMDC, MoSe₂, was also investigated using both intensity dependent SHG and wavelength dependent SHG techniques. The results suggested its potential use of high-powered second-order NLO devices. In chapter 5, the resonant second harmonic generation characteristics were analyzed in ternary monolayer alloy MoS_{2(1-x)}Se_{2x}, showing a feasibility to apply them into tunable second-order NLO devices. Finally, stacked heterostructures needed to be investigated to solve the quest of high NLO material. The final chapter will present our preliminary but rather interesting results on artificially stacked

monolayers TMDCs for next-generation of 2D optoelectronic devices.

Chapter 1: Introduction of monolayer TMDCs

1.1 History of development:

There are almost 60 compounds of TMDC existing naturally. Majority of them are in the layered structure. From synthesis aspects, the first known synthetic TMDC approaches appeared during the 1950s and since then they were found to be developed rapidly in 1960s.[1] At the beginning stage, the researches on these materials are more concentrated on the catalysis and energy storage application. One of the first studies on catalytic properties of TMDC was published in 1986, nearly two past decades ago.[2] However, these layered materials have not been paid more attention to until the discovery of Graphene, a single layer of carbon by sp^2 bonding, by Novosolov and Geim in 2004 and mechanical exfoliation technique which allows cleaving a single layer from their bulk. This finding sparked a surge for a flood of fundamental studies on the growth mechanism of monolayer MoS_2 . Since then, the exciting physical properties have been continuously revealed in monolayer transition metal dichalcogenides (TMDCs), thus triggering numerous following studies on their novel layer-dependent properties. Nowadays, Group VI TMDCs are rising two-dimensional materials, which have a chemical formula of MX_2 (where M can be Mo or W, X can be S or Se). This group was chosen as subject matters in my dissertation.

1.2 Structural properties:

Structurally, monolayer MX_2 are three-atom-thick (theoretical thickness less than 1 nm), comprising one layer of transition metal sandwiched between two layers of chalcogenides atoms in prismatic configuration as shown in the Fig. 1-1.[3] A strong covalently bonded atoms exist within an intra-layer, whereas the layers weakly interacted to its adjacent layers through Van Der Waal forces, making them easily to be peeled off mechanically. In general, there are three different polymorphs and polytypes of TMDC. The widely observed polytypes are 1T, 2H and 3R, which have one, two, three layer per unit cell in tetragonal (T), hexagonal (H), rhombohedral (R) primitive cell.[4] The difference in atomic spatial arrangement and symmetry of these phases leads to various electronic properties, for instances; the 1T phase is rarely found in nature and exhibiting metastable

metal, whereas 2H and 3R are commonly observed in MoS₂ crystal and possessing the semiconducting properties.[4] The local phase conversion from semiconducting (2H) to metallic (1T) in case of MoS₂ under a specific condition is feasible as demonstrated by Chhowalla et al. .[5] From catalysis and energy storage aspects, the chemically induced phase change is frequently used to convert 1T MoS₂ using a solution containing Li⁺, H⁺. [5, 6] Besides, some rare structures of monolayer, such as 1T' and 1H, also exists. The former is the phase having hexagonal symmetry with one layer per unit cell, while the latter phase is the structurally distorted phase of 1T.[4, 5]

In the bulk form crystal 2H-MoS₂ (D_{6h} symmetry) has the inversion symmetry. Being a monolayer form, 2H-TMDCs belong to lower symmetry point group (D_{3h}) point group. This symmetry point group includes a horizontal σ_h reflection plane, a threefold C₃ rotation axes, S₃ mirror rotation axis, three twofold C₂ rotation axes situated at monolayer plane and a mirror plane containing twofold rotation axes.[7] More importantly, the inversion symmetry is absent in this point group, therefore leading to a non-zero electric dipole. This spontaneous dipole, which lies parallel to mirror plane, will oscillate under a strong field produced by a laser.

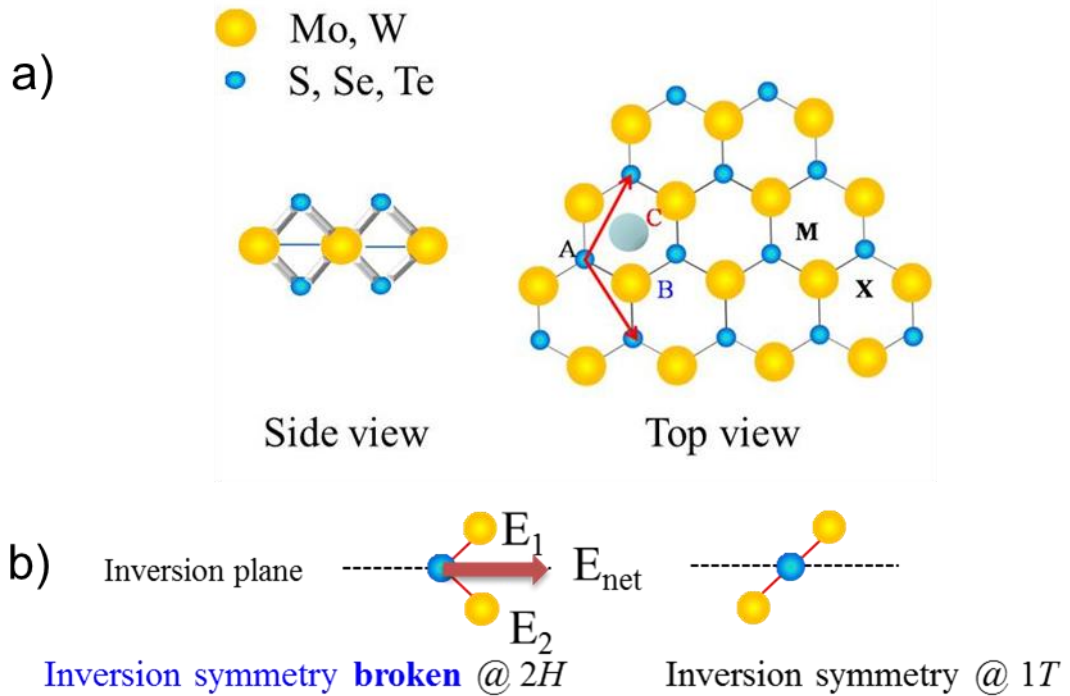


Figure 1-1: a) Atomic structure of monolayer MX₂ from side view and top view: hexagonal lattice composed of Mo/W atoms (yellow balls) and S/Se/Te (blue balls) b) schematic

illustration of difference in atomic arrangement for two commonly observed phases 1T and 2H

1.3 Synthesis approaches of monolayer TMDCs:

Analogous to graphene, monolayer TMDCs can be synthesized by various approaches. The approaches are basically classified into two primary categories. The first one is called top-down approach, typically mechanical exfoliation in which the monolayer was produced by mechanically cleaved using Scotch tape started from bulk crystal produced by CVT technique.[8] On the demand of study, there also have been a lot of layer-by-layer thinning approaches. Typically, Castellanos-Gomez *et al.* evaporated layer by employing sufficiently high energy laser.[9] In more scalable approaches, Lu *et al.* can controllably reduce the thickness of few-layer MoS₂ layer-by layer down to monolayer using thermal annealing.[10] Similarly, Liu *et al.* shows possibility of peeling off MoS₂ layers using Ar⁺ plasma until the monolayer is achieved.[11] Although the superior quality of as-produced specimens is well-appropriate to fundamental studies, the lateral size limitation is a primary drawback of the “top-down” specimens when applicable to industry. Consequently, the occurrence of bottom-up approaches is highly desirable for industrial device fabrication. For optical characterization, we adopted the bottom-up approaches to yield such a large and high-quality onto the transparent and opaque substrates.

1.3.1 Chemical vapor deposition (CVD) growth:

Chemical vapor deposition (CVD) has been known as a facile, reliable method for mass production. This approach is able to produce relatively high-quality monolayers on the large scale wafer.[12-14] As described in the Fig. 1-2, a typical experiment involves employing the chalcogenide (Se, S) and transition metal oxides (MoO₃, WO₃) powders as the source materials based on the following reaction:



Normally, inert gases like Argon and/or Nitrogen were employed as the carrier gas, conveying the vapor phase of S to the reaction zone. The reaction commonly takes place at the nearly atmospheric pressure. The typical experiment can be described as follows: we used two-zone hot wall furnace to synthesize large-size MoS₂ onto SiO₂/Si substrate. High-purity

MoO₃ (99%, Sigma Aldrich) and sulfur powder (99.5%, Alfa Aesar) were separately laid in two different graphite crucibles and the substrates were faced down and placed on the upper side of MoO₃ powder. All of them are placed in the quartz tube, which was initially pumped to a base pressure ~80 mTorr. The oxidation removal process was done by continuously flushed high-purity N₂ gas. To yield the monolayer MoS₂, the reaction chamber temperature was initially raised to 400°C with a heating rate of 25°C/min for 5mins. During this step, the pressure was maintained at 300 Tor and carrier gas flow rate was kept at 10 sccm. Then, the reaction temperature was increased to ~830 °C with a heating rate of ~25 °C/min and held for 5 min before cooling down naturally to room temperature.

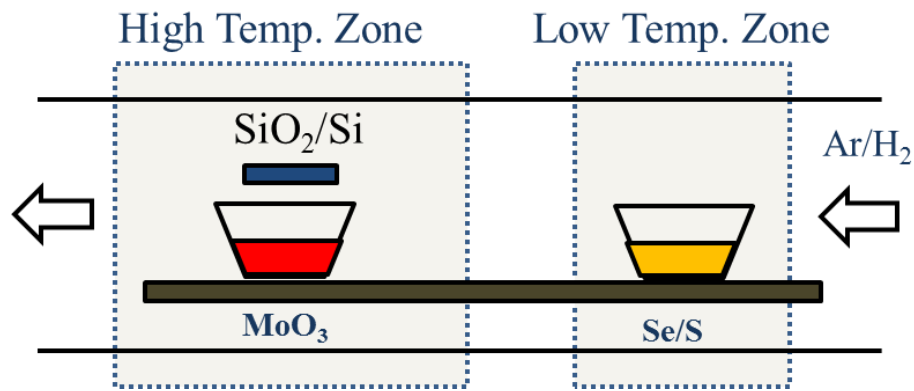


Figure 1-2: Schematic illustration of chemical vapor deposition approaches using two hot-wall furnaces

It is found that if the reaction occurs at the low pressure, the films will consist of many MoS₂ particles and in some regions, the remaining MoO₃ still exists.

The produced film MoS₂ is composed of many single, triangular-shaped MoS₂ grains (flakes) at the edge of the film as shown in the figure. Meanwhile, at the center of sample, these grains merge together into a continuous region with many grains boundaries as indicated in Fig. 1-3.

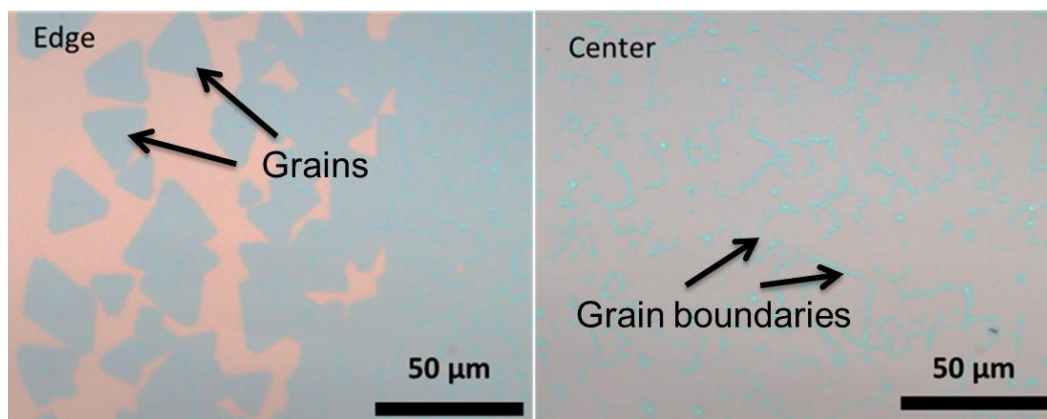


Figure 1-3 OM images taken at the edge (left) and at the center (right) of a typical CVD-grown sample

Due to the lower reactivity of Se element, the Se branch of MX_2 is apparently difficult to be synthesized on large scale as compared to S branch. Therefore, H_2 gas is sometimes introduced during the reaction in order to chemically reduce the high-melting transition oxide (WO_3) to its less oxidation state.

1.3.2 Pulsed laser deposition (PLD) assisted method:

This method is generally different from the chemical vapor deposition in the way that the oxide layer was firstly deposited onto the substrate by physical vapor deposition methods, for instances, thermal evaporation or sputtering, pulsed laser deposition. Then, the oxide layer was sulfurized and/or selenized in a quartz tube at the elevated temperature in order to form monolayer MX_2 . The first oxide layer deposition is a very important stage, which determines the thickness and quality of final specimens. By controlling the laser power at the beginning stage, I and my colleagues could produce the remarkable quality of MX_2 as compared to commercially available specimens. More details can be found in the experimental method section of chapter 4.

1.4 Optical characterization of 2-D semiconductor:

1.4.1 Neutral exciton:

The photo-excitation of an electron from the occupied valence band to unoccupied conduction band leaves an empty electron state at valence band. This empty electron state

exhibits a positively charged particle, the so-called “hole”. In the system where the Coulomb interaction is relatively strong, the photo-excited electron tightly couple with a hole to form two-particle system, the so called “exciton”.

Exciton in monolayer TMDCs possesses intriguing properties as compared to bulk semiconductor. Because of the covantly bonding in intralayers, the exciton in bulk TMDCs closely behaves like ‘Mott-Wannier” exciton with large radii. To quantitatively analyse, the exciton binding energy inTMDCs can be approximately modelled by hydrogen like model as given by:

$$E_s \propto \frac{R_y \mu_0}{m_0 \epsilon_{eff}^2}$$

Where R_y is the Rydberg constant of 13.6 eV and ϵ_{eff} is a typical effective dielectric constant of the system, μ_0 the reduced mass, m_0 is the free electron mass. Based on this hydrogenic model, there are several facts that result in the experimentally large excitonic binding energy (~400 – 900 meV) in monolayer TMDCs.[15-19] as opposed to their bulk counterparts. These facts includes i) the smaller electron and hole distances, ii) the relatively large effective masses at K point of electron, m_e , and hole, m_h iii) the weakened electronic screening effect generally occurs in 2D materials as a result of reduced dimensionality (small ϵ_{eff} , that is, the surrounding area is often air/vacuum), which is dramatically enhances Coulomb interaction in monolayers.

Table 1: Summary of A-exciton binding energy of monolayer TMDCs extracted from different experimental techniques

Exfoliated Sample	Experimental technique	Binding Energy (eV)	Reference
MoS ₂	PLE	0.44	<i>Hill et al., 2015</i>
MoSe ₂	PL	0.5	<i>Zhang et al., 2015</i>
WS ₂	Reflectance	0.83	<i>Hanbicki et al., 2015</i>
WSe ₂	Reflectance	0.37	<i>He et al., 2014</i>

Unlike gapless graphene, monolayer TMDCs with a direct optical band gap (ranging from $\sim 1.3 - 1.85$ eV) exhibit strong photoluminescence in the visible to near IR range spectrum. This is consequence of dramatic change of VBM from Γ to K point in the first Brillouin zone as they are thinned down from bulk to monolayer. Such direct gap materials are interesting in term of device application because of their light emission efficiency. There is a numerous effort to produce the prototypes based on monolayer TMDC, such as sensor,[20] photodetector[21] and energy harvesting devices[22, 23]

In electronic band structure monolayer TMDC, both valence band maximum and conduction band minimum are spin-polarized. Since the valences band (VB) is essentially composed of wave function from d-orbital of a heavy transition metal as seen in the Fig. 1-4(a), therefore the spin and orbit angular momentum strongly couple to each other (200 - 400 meV). Such a strong spin-orbit coupling along with broken inversion symmetry leads to the splitting of VB edge into two distinct energy states in momentum k -space.[24] This coupling results in two valence sub-bands; which give rise two “bright” and direct excitons: A and B arising from the transition from energies states that have the same spin states as schematically depicted in Fig 1-4(c). In contrast to the strong spin-orbit splitting at VB, the spin splitting in CB is energetically small (\sim tens of meV).[25] It is surprising that the spin-state order of CB depends upon on the transition metal atom (Mo and W). This CB spin splitting leads to an energy separation between dark exciton” which is a spin-allowed transition or optically active transition and “bright excitons” spin-forbidden transition, optically inactive.

Another interesting property occurs in the monolayer TMDC is the inequivalent responses of excitons at K points in momentum space with respect to the clockwise/counterclockwise circularly polarized lights. This phenomenon results from the inversion symmetry breaking and the restoration of time reversal symmetry at K point. As a result, it gives rise to a new degree of freedom other than spin and charge density, the so-called “valley degree of freedom”. [26] This imbuing property renders TMDCs to be potential candidates for the next generation electronic devices, so-called valleytronics.

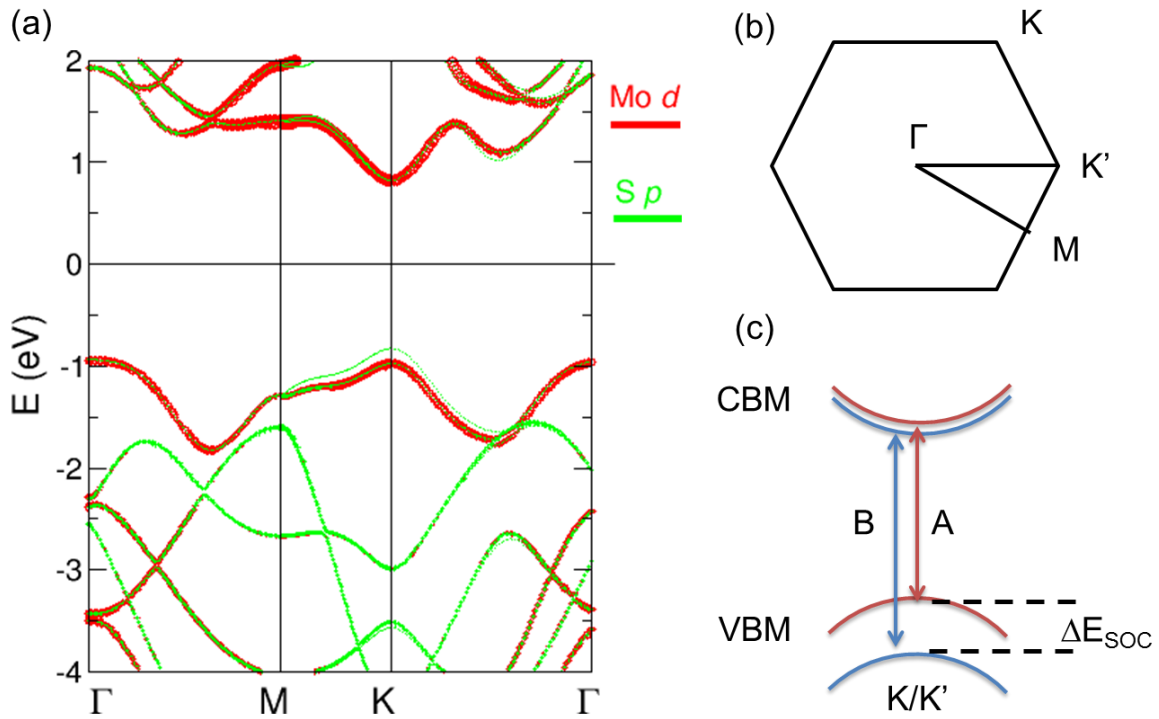


Figure 1-4 Electronic band structure of typical monolayer TMDC (MoS_2) b) The first Brillouin zone of monolayer MoS_2 where different k points are denoted as M, K, K' c) Schematic picture of finer band structure at K/K' points showing two direct transition at valence band maxima (VBM) and conduction band minima (CBM). Red and blue lines represent the spin-up and spin down states. Red and blue arrows indicate two bright A and B excitons.

1.4.2 Charged excitons (trions) and biexciton:

In addition to neutral exciton, other quasiparticles can be formed in intermediate or high-density exciton regime. The excitons no longer behave as the bound electron-holes but more like Coulomb-correlated gas. Due to a large number of structural defects such as point defects, line defects in the lattice of TMDC material, the density of free carrier charges considerably increases. When the inelastic scattering between the exciton and free carriers occurs, an exciton can bind an additional charge to form three-body systems, the so-called trions state. Likewise, the inelastic scattering between excitons can form a two-exciton state, the so-called biexciton.

1.4.3 Basic structural analysis of monolayer TMDCs

This section describes fundamental analysis to distinguish monolayer area from few-layers and bulk. Various substrates such as fused silica, SiO₂/Si, sapphire, and etc... can be used to synthesize monolayer TMDCs. Among these substrates, the SiO₂/Si with thin layer of SiO₂ is widely employed because it can enhance the optical contrast, which helps to qualitatively identify thickness of monolayer TMDCs. Moreover, the SiO₂/Si substrate is easy to further fabricate microelectronic devices.[27]. Beside optical contrast, Raman spectrum is commonly used to determine the monolayer area. Particularly, the energy separation between two phonon modes, A_{1g} and E_{2g}^1 , at high energy can be exploited to examine the thickness of mechanically exfoliated MoS₂ as its thick is less than 5 layers.[28] Besides, the uniquely strong photoluminescence feature of monolayer as its indirect band gap is converted to direct band gap can be an indicator for its thickness. In addition to qualitative analysis, the thickness of monolayer can be precisely probed by atomic force microscope operating at tapping mode.

There are many techniques to assess the exciton binding energy in monolayer TMDCs. Those include cryogenic and room temperature photoluminescence, reflectance and absorption spectroscopy and nonlinear measurement techniques for instance, two photon absorption spectroscopy. The next section will discuss on the nonlinear theory mainly concentrated on second harmonic generation.

1.5 Nonlinear optical theory: second harmonic generation (SHG)

In past decades, how light interacts with a solid matter has become a central puzzle for the research community. Nonlinear optics is research field where the electron polarization of material interacts nonlinearly with electromagnetic fields (light), which is completely different from linear optics counterpart. Whether or not the interaction between light and matters is nonlinear or linear is determined by the excitation strength. The large excitation strength up to 2.5 kW/cm² is required to trigger the nonlinear phenomenon. This power value cannot be achieved by an ordinary laser source. This is only available in a pulsed laser.

Therefore, the physical phenomena govern inside nonlinear media would not have been understood if a pulsed laser had not been invented by Theodore Maiman in 1960. The

first experimental observation of an NLO was about SHG, which was carried out by Franken et al. in 1961. In their experiment, they observed the emitted UV light with a wavelength of $\lambda = 347.15$ nm when they illuminate a fundamental laser beam with a wavelength of $\lambda = 694.3$ nm into the quartz crystal. This incident marked the historic point the field of NLO.

Recall that Maxwell's equations when light travels along the medium:

$$\begin{aligned}
 \nabla \cdot \vec{D} &= \rho \\
 \nabla \times \vec{E} &= -\frac{\partial \vec{B}}{\partial t} \\
 \nabla \cdot \vec{B} &= 0 \\
 \nabla \times \vec{H} &= \vec{J} + \frac{\partial \vec{D}}{\partial t}
 \end{aligned} \tag{1.1}$$

Where \vec{D} is the electric displacement, ρ is the free charge density, \vec{E} is the external electric field, \vec{B} is the magnetic field and \vec{H} is the magnetic auxiliary vector, \vec{J} is the free current density. In the case of $\rho = 0$ and there is no free current $\vec{J} = 0$, Eq (1) can be explicitly solved. Assuming that the media is not magnetic, $\vec{B} = \mu_0 \vec{H}$ where μ_0 is permeability of free space. Meanwhile, \vec{D} and \vec{E} are connected through this relation $\vec{D} = \epsilon_0 \vec{E} + \vec{P}$, where ϵ_0 is the permittivity of free space.

The optical wave equation can now be derived as follows: Taking the curl of Faraday's Law and interchanging the space and time derivatives for the time-varying \vec{B} using

$$\begin{aligned}
 \nabla \times \vec{B} &= \mu_0 \frac{\partial \vec{D}}{\partial t} \\
 \nabla^2 \vec{E} - \nabla(\nabla \cdot \vec{E}) + \mu_0 \frac{\partial^2 \vec{D}}{\partial t^2} &= 0
 \end{aligned} \tag{1.2}$$

Replace \vec{D} by this relation $\vec{D} = \epsilon_0 \vec{E} + \vec{P}$ into Eq(1.2):

$$\nabla^2 \vec{E} - \nabla(\nabla \cdot \vec{E}) + \frac{1}{c^2} \frac{\partial^2 \vec{E}}{\partial t^2} = -\frac{1}{\epsilon_0 c^2} \frac{\partial^2 \vec{P}}{\partial t^2}, \tag{1.3}$$

Where $c = \frac{1}{\sqrt{\epsilon_0 \mu_0}}$ is the speed of light. Using the vector identity $\nabla \times \nabla \times \vec{E} = \nabla(\nabla \cdot \vec{E}) - \nabla^2 \vec{E}$

and assume that $\nabla(\nabla \cdot \vec{E})$ is extremely small when slowly varying amplitude approximation

holds, then the optical wave equation

$$\nabla^2 \vec{E} - \frac{n^2}{c^2} \frac{\partial^2 \vec{E}}{\partial t^2} = \frac{1}{\epsilon_0 c^2} \frac{\partial^2 \vec{P}}{\partial t^2} \quad (1.4)$$

From Eq. (1.4) we can see that the external electric field \vec{E} induces a polarization \vec{P} in the medium, which in turn governs electric field \vec{E} . This motion equation is the central point of light-matter interaction in any media. The polarization \vec{P} is defined as the dipole moment per unit volume. Its strength relates to amplitude of external field \vec{E} . In the linear regime, this polarization can be expressed:

$$\vec{P}(t) = \epsilon_0 \chi^{(1)} \vec{E}(t) \quad (1.5)$$

Where $\chi^{(1)}$ is the linear susceptibility. For the nonlinear regime, the induced polarization in Eq(1.5) can be expanded using power series:

$$\vec{P}(t) \propto \chi^{(1)} \vec{E} e^{-i\omega t} + \chi^{(2)} \vec{E}^2 e^{-i2\omega t} + \chi^{(3)} \vec{E}^3 e^{-i3\omega t} + \dots + \chi^{(n)} \vec{E}^n e^{-in\omega t} \quad (1.6)$$

Where $\chi^{(2)}$, $\chi^{(3)}$ and $\chi^{(n)}$ are the second-order, third-order and n^{th} order susceptibility. These quantities are tensors with rank of $R(n+1)$ acting on each of the components of the external electric field.

1.5.1 Sum and difference frequency generation

Assume that the electric field is comprised of two different frequency components expressed by:

$$\vec{E}(t) = E_1 e^{(-i\omega_1 t)} + E_2 e^{(-i\omega_2 t)} + c.c., \quad (1.7)$$

The SFG can occur when light of two different frequencies ω_1 and ω_2 simultaneously incident a nonlinear medium where they are converted to a third frequency, ω_3 , which is the sum of two input beams.

$$\omega_3 = \omega_1 + \omega_2$$

There is another possibility that the output light of frequency from the medium is the difference of two input frequencies.

$$\omega_3 = |\omega_1 - \omega_2|$$

Note that SFG and DFG are second-order $\chi^{(2)}$ processes. For application demanding, SFG can be exploited to generate tunable radiation in the UV range while DFG has been used to generate mid-IR beam.

1.5.2 Second harmonic generation:

Second harmonic generation (SHG) is defined as a parametric process happening in the non-centrosymmetric media which doubles the frequency of incident light. From the definition, the SHG is required an electric field of the incident upon the medium whose $\chi^{(2)}$ is nonzero. In the other words, the medium must be noncentrosymmetric.

Suppose that the fundamental electric field of the incident light with an optical frequency of is represented by

$$\vec{E}(t) = E_1 e^{(-i\omega_1 t)} + c.c, \quad (1.8)$$

where c.c. is the complex conjugate.

The second-order polarization can be expressed by:

$$\vec{P}^{(2)}(t) = 2\varepsilon_0 \chi^{(2)} E E^* + (\varepsilon_0 \chi^{(2)} e^{-i2\omega t} + c.c.). \quad (1.9)$$

Equation 1.9 indicates that the second-order polarization composed of two terms: one is the optical rectification without frequency and second term with frequency 2ω . The second term can give rise to produce of light with second harmonic frequency. The static component is the first term can be experimentally measure using the

Since the SHG is parametric, the energy is conserved during this process. Therefore, the resulting SHG beam is highly directional. The SHG is basically a special case of sum frequency generation (SFG), where the two input waves have the same frequency. The output wave has a wavelength of 2ω . From a quantum point of view, the two incoming photons with the frequency of ω were simultaneously absorbed by media. The electron is firstly excited to intermediate states, which are the virtual states, by absorbing energy from the photons. The electron will not stay at this virtual state for a long time, and then it relaxes to ground state and release photon energy with double frequency.

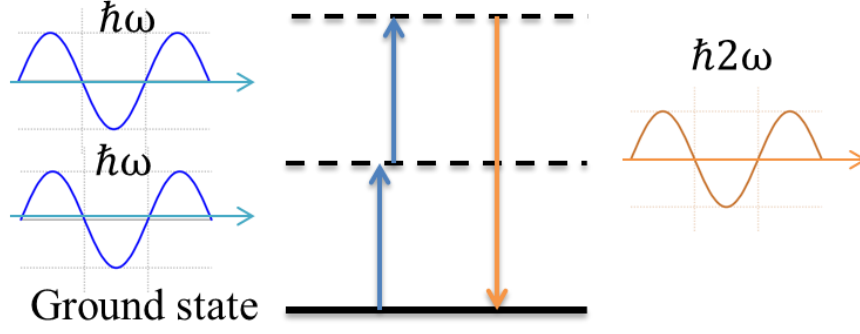


Figure 1.4 Schematics of second harmonic generation process in nonlinear medium

1.5.3 Phase- matching:

For nonparametric processes like second harmonic generation or sum frequency generation, the phase matching condition has to be satisfied in order to obtain incident energy at the most efficiently

$$\Delta k = k(2\omega) - 2k(\omega) = 0$$

Where Δk is momentum mismatch term, $k(2\omega)$ and $k(\omega)$ are wave numbers of second harmonic beam and fundamental beam. In dispersive media like bulk material, phase matching is hard to reach when out of unity length owing to the rather strong wavelength-dependence of refractive index, so called the chromatic dispersion.

The expression for the SHG intensity $I(2\omega, l)$ with l being the interaction length is given by:

$$I(2\omega, l) = \frac{\omega^2 |\chi^{(2)}|^2 l^2}{2n_{2\omega} n_{\omega}^2 c^3 \epsilon_0} \text{sinc}^2\left(\frac{\Delta k l}{2}\right) I^2(\omega)$$

Where n_{ω} and $n_{2\omega}$ are the refractive indices at ω and 2ω respectively and c is the speed of light in a vacuum and $I(\omega)$ is pump intensity. From this equation, if the process is not phase-matching the SHG intensity fluctuates as $\text{sinc}^2(\Delta k l / 2)$. In other words, the SHG field is out of phase with the incident field for $l > l_c = \frac{\pi}{\Delta k}$. In this case, the SHG intensity is always weaker than $I(2\omega, l)$ and limits the use of NLO material. In contrast, if phase matching condition is achieved, the corresponding SHG intensity is maximized. Typically, SHG intensity increases quadratically with l

1.5.4 Multiphoton absorption (MPA):

MPA is physical phenomena where the medium absorbs simultaneously N photons. In contrast to SFG or DFG, this process is non-parametric that causes electronic excitation of a medium. The number of photons N is determined by relation $N\hbar\omega \geq E_g$ with energy bandgap E_g for semiconductor. Since MPA depends on the N -th power of $I(\omega)$, MPA is subsequently much weaker the linear absorption. This process has been widely taken advantage in multiphoton spectroscopy and microscopy because of the enhanced spatial resolution. In spite of its importance in the optical limiting application, the efficiency of NLO devices can be hampered by nonlinear loss and optical damage caused by MPA.

Chapter 2: Photosensitivity Study of Metal-Semiconductor-Metal Photodetector Based on Chemical Vapor Deposited Monolayer MoS₂

2.1 Introduction

2.1.1 Overview

Motivated by the breakthrough of graphene and its novel features[29], many groups of two dimensional (2D) nanomaterials, typically, transition metal dichalcogenides MX₂ (M = Mo, W; X = S, Se) have been explored as next-generation alternatives for recent years. Among them, molybdenum disulfide (MoS₂) is currently the well-studied 2D semiconductor material due to remarkable layer dependent properties. In contrast to gapless graphene, monolayer MoS₂ exhibits ~1.2 eV indirect to ~1.83 eV direct band gap transition, which arises from quantum confinement effect when its thickness is reduced to monolayer[30]. More interestingly, recent studies have reported that monolayer and few-layer MoS₂ shows intriguing optical properties, as exemplified by valley-selective circular dichroism[31, 32], and layer dependence of nonlinear optical properties[33]. Recently, Yin *et al.* have demonstrated the first mechanical exfoliated monolayer MoS₂ based phototransistor that exhibits responsivity ~7.4 mA/W better than that of the graphene based device, ~1 mA/W[34]. Such findings facilitate monolayer and few-layer MoS₂ to be a promising candidate for lightweight, flexible optoelectronic devices such as phototransistor[34], photodetectors (PDs)[35], solar cell[36].

2.1.2 Motivation

Structurally, bulk MoS₂ is constituted of strongly bonded S-Mo-S layers, whereas two adjacent layers are weakly linked by Van der Waals force in the trigonal prismatic arrangement. Therefore, mechanical exfoliation approach has been commonly used to obtain unmatched, high-quality monolayer and few layer MoS₂ subjected to fundamental research. Nevertheless, the limitation in grain size is the main challenge for mass production. To take advantage of peculiar optical and electrical properties and further boost development of optoelectronic applications, synthesizing large area, highly crystalline monolayer MoS₂ is

highly necessary. As a result, various approaches, such as thermal decomposition of ammonium tetrathiomolybdate[37], sulfurization of the pre-deposited molybdenum film[38], catalyst-assisted vapor-solid growth[39] have been employed to synthesize large area monolayer and few-layer MoS₂ for application purpose. In this trend, Tsai *et al.* have very recently grown trilayered MoS₂ by thermal decomposition of ammonium tetrathiomolybdate approach and then fabricated metal-semiconductor-metal photodetectors based on such film.[40] The device shows high photoresponsivity up to 1.04 A/W and fast response time/recovery time ~40/50 μs. However, this approach has a drawback that is involved in two complicated post-annealing processes after dip-coating the film. Currently, chemical vapor deposition (CVD) process, which uses molybdenum trioxide (MoO₃) and sulfur (S) as reactants, has been one of the most facile and highly reproducible routines to grow large-area monolayer MoS₂. [41, 42] However, the number of studies on monolayer MoS₂ based electronic devices, where the MoS₂ film is synthesized by the CVD approach, so far have been limited.

In this chapter, we fabricated a planar metal-semiconductor-metal photodetectors based on monolayer MoS₂. The MoS₂ films were grown via CVD method, showing excellent structural and optical properties. The device exhibited good photoresponsivity ~7.7 mA/W for the wavelength of 470 nm, which is relatively comparative to the mechanically exfoliated monolayer MoS₂ PDs. The rise /fall time of devices was about 1/0.7 s. Finally, we proposed that the existence of grain boundary in monolayer MoS₂ might act as scattering sites reducing the photo-generated current, which in turn degrades the electrical performance of PDs.

2.2 Experimental details

MoS₂ films were grown on 2×2 cm² 300 nm thick SiO₂/Si via chemical vapor deposition method. The detailed growth mechanism has been reported in our previous work. In brief, sulfur (S) powder was put into a graphite crucible and placed upstream inside 2 inches diameter quartz chamber. Molybdenum trioxide (MoO₃) powder (99.999%, Materion) was put into another crucible laid on downstream. The SiO₂/Si substrate was faced upside down and mounted on the top of MoO₃ source. The CVD system was rapidly heated up to 400°C for 30 min while sulfur was kept at 100°C in the rate of 100 sccm N₂. The chamber was rapidly heated up 900°C in the rate of 25°C/min, keeping for complete reaction within 5

min. The system was cooled in the rate of 15°C/min to room temperature. The N₂ gas was strictly controlled by the mass flow meter.

Surface morphological properties of the as-grown thin film were examined by atomic force microscope (AFM) (Veeco, Dimension 3100) via tapping mode. Thickness of the films was determined by line profiles extracted from AFM measurement. Raman scattering and photoluminescence (PL) spectra were measured at room temperature by using an Ar⁺ laser with a wavelength of 514.5 nm (Melles Griot, 35-LAP-431-220) as an excitation light source. The focused laser spot size was ~10 μm² for PL and Raman spectra. Scattered light from the sample was analyzed by a single grating spectrometer with a focal length of 50 cm (Princeton Instruments, SP-2500i) and detected with a liquid-nitrogen-cooled silicon CCD detector (Princeton Instruments, Spec-10). All PL and Raman spectra were normalized by Si Raman peak at 520cm⁻¹.

The interdigital fingerlike (50 μm wide spacing) devices were fabricated by evaporating Au electrodes (100nm) directly on top of the MoS₂ layer by using a shadow mask. The electrical measurement was characterized by using Keithley 2620 series. Photoresponse was performed by varying wavelength via modulating light source (Ivium modulight, Ivium Tech.). For all monochromatic lights, the optical power intensity was maintained a constant of 0.3 mW/cm². The bottom gate bias voltage was varied from -20 V to 30 V. The photocurrent was calculated by the reduction of the dark current at a certain bias voltage ($I_{\text{light}} - I_{\text{dark}}$).

2.3 Result and discussion

2.3.1 Structural characterization of MoS₂ film

Prior to electrical characterization, we carried out a number of measurements to ensure that the as-grown thin films are high quality monolayer MoS₂. Firstly, the layer number was qualitatively determined under an optical microscope. The optical contrast enables the thin layer to be discernible under the microscope due to optical interference between the thin layered film and the underlying oxide layer of the substrate. The optical images of monolayer MoS₂ deposited on 300 nm thick SiO₂/Si substrate are depicted in Fig.

2-1(a)-(b). Isolated, triangular-shaped grains of MoS₂ are observed at the edge of MoS₂ thin film. The grain size is as large as 120 μm and distributed in the wide range from 50 to 120 μm. Twin faceted and multi-faceted grains are also found as shown in Fig. 2-1(a). At the center, flakes merge into large grains with few micrometers wide grain boundaries, thus forming a continuous film as seen in Fig. 2-1(b). This observation agrees well with the recently reported studies.[32, 39, 41, 42] The thickness of MoS₂ film was further confirmed by AFM as shown in Fig. 2-1(c). The measured value is ~0.65 nm as depicted in Fig. 2-1(d), consistent with theoretical thickness of monolayer MoS₂ of ~0.62 nm. To gain more insights into structural properties of monolayer MoS₂, Raman scattering was used to analyze phonon-photon interaction and will be discussed in the next section.

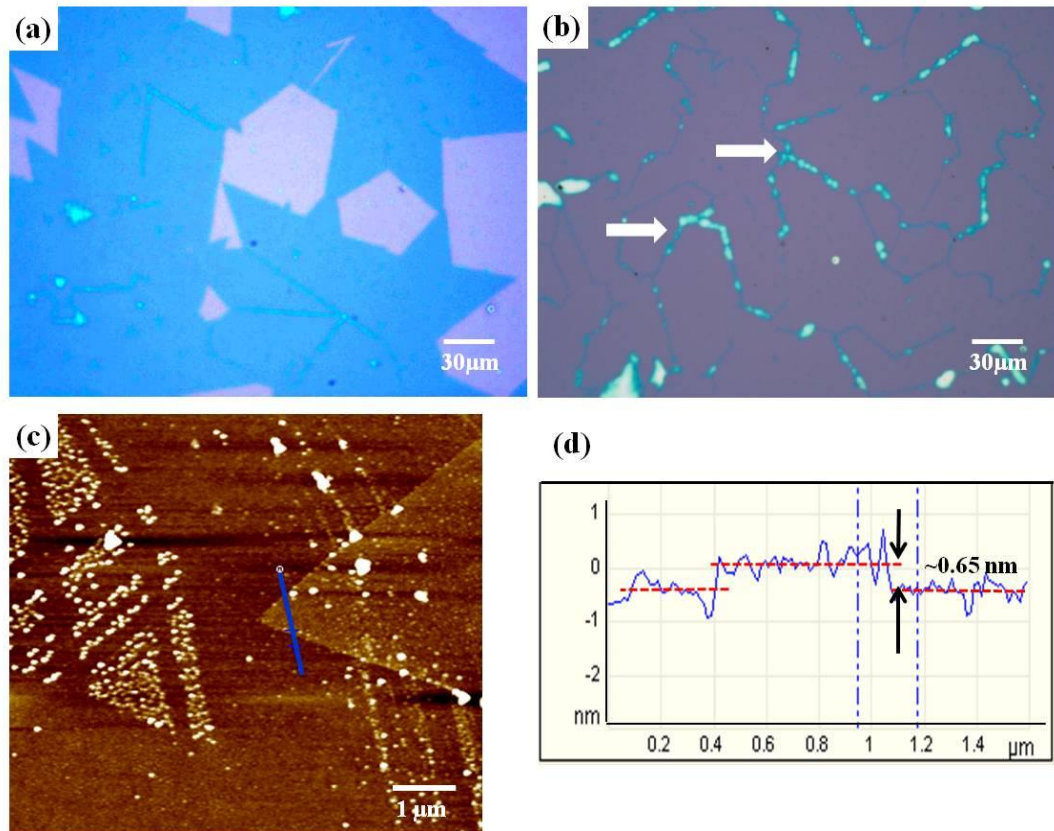


Figure 2-1 (a) Optical images of as-grown MoS₂ on 300 nm SiO₂/Si substrate at the edge and (b) center of the wafer with the existence of grain boundaries (white arrows). (c) Surface morphology of monolayer MoS₂ at the edge of wafer and (d) the height profile extracted from AFM image

It is well known that Raman scattering is nondestructive, indirect method to identify

the layer number of two-dimensional material. Thus, we carried out macro-scale Raman measurement to characterize the number of layer and optical quality of MoS₂ films as shown in Fig. 2-2(a). We observed two predominant peaks at ~383.6 cm⁻¹ and 404.2 cm⁻¹ corresponding to in-plane (E_{2g}^1) and out-of-plane (A_{1g}) vibrational modes, respectively. The peak separation (Δk) value between these two peaks is ~20.6 cm⁻¹. According to the layer number dependence of peak difference reported in previous studies[28, 43, 44], the acquired peak separation indicates that the as-grown sample is likely to be in the monolayer regime. Besides, bilayer is seen to be formed only in certain small area. The possible reasons for the difference in the thickness could be due to random nucleation seeds distribution and the extra seed growth on the first layer. It is known that full width at half maximum (FWHM) of E_{2g}^1 is a criterion to evaluate crystallinity of MoS₂ thin film. In case of our sample, FWHM of E_{2g}^1 was of ~6.4 cm⁻¹, close to the reported value of 4.2 cm⁻¹ in recent studies[44]. Accordingly, the as-grown MoS₂ thin film is highly crystalline monolayer MoS₂. Fig. 2-2(b) shows a photoluminescence (PL) spectrum of the representative MoS₂ film. The characteristic peak is observed at a wavelength of ~670 nm, which is assigned to exciton. This peak is associated with valence band maximum to conductance band minimum transition at the K point in the first Brillouin zone. Moreover, PL intensity exhibits ~600 times stronger than that of Si peak. The intensity of observed peak was normalized by Si Raman peak at 20 cm⁻¹. The occurrence of strong luminescence and PL peak position are clear evidences for high-quality monolayer MoS₂ film.

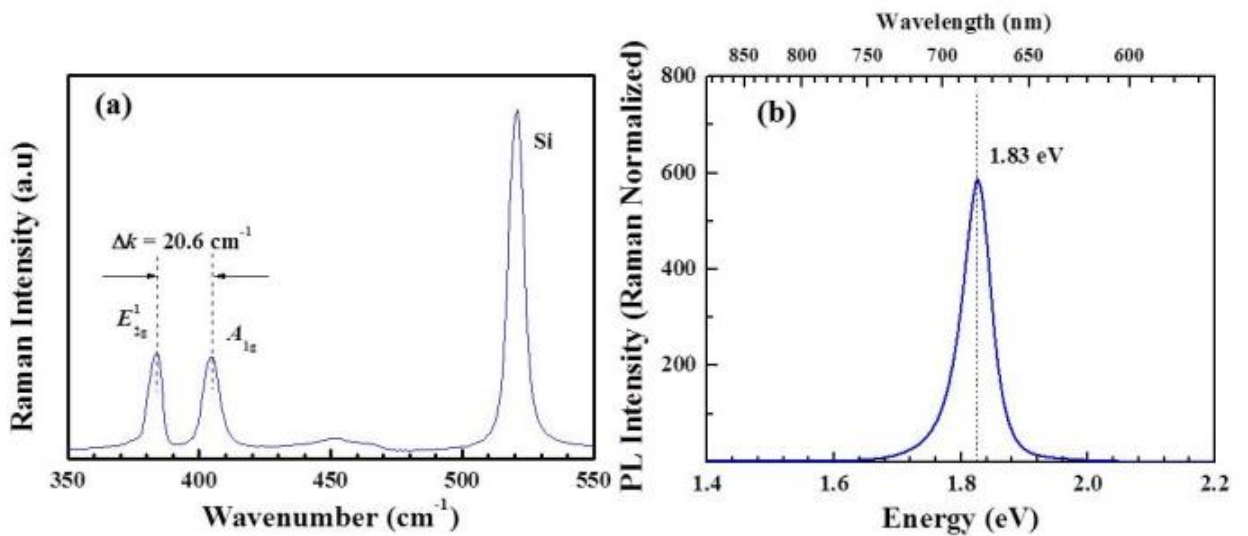


Figure 2-2: Raman scattering (a) and PL spectrum (b) measured at the center of MoS₂ film.

2.3.2 Electrical characterization

The inter-digital MSM PDs devices were fabricated at the center of the MoS₂ films, where the continuous film was formed along with the randomly oriented grain boundaries as shown in Fig. 2-3(a-b). The MSM PD is equivalent to two Schottky's diode connected back to back. One diode is forward biased and the other one is reverse biased. Electrical properties of monolayer MoS₂ based PDs were analyzed by investigating the current-voltage characteristic at various wavelengths in visible spectrum as shown in Fig. 2-3(c). Current-voltage curves show a typical Schottky contact behavior, which is expected to form when bringing high work function Au ~5.1 eV in contact with semiconductor MoS₂. Additionally, *I-V* curves indicate that photocurrent at the wavelength much shorter than 670 nm, direct bandgap of monolayer MoS₂, increases markedly. Meanwhile, those of longer wavelengths closer to 670 nm are apparently unchanged under illumination condition. This manner could possibly be explained by two reasons as proposed by Yin *et.al.*[34] The number of photo-generated carriers in MoS₂ is significantly dependent on the energy of incident photon and the number of incident photon. In other words, the wavelength of incident light and the optical power strongly influence the photocurrent. In order to excite the electrons in monolayer MoS₂ from valence band to conduction band, the incident photon is required to possess energy that is greater than the band gap energy of monolayer MoS₂, which is equivalent to the wavelength ~670 nm. Additionally, the transition probability of photo-generated electron is also an important criterion to evaluate the magnitude of photocurrent. The electrons will be supplied with more energy from higher energy photon, that is, shorter wavelength, which allows these electrons to surmount not only the defect trapping sites inside MoS₂ but also Schottky barrier at Au/MoS₂ interface as well. Therefore, the higher photon energy supplied to electron, the larger photocurrent will be generated in PDs as found in current-voltage curves.

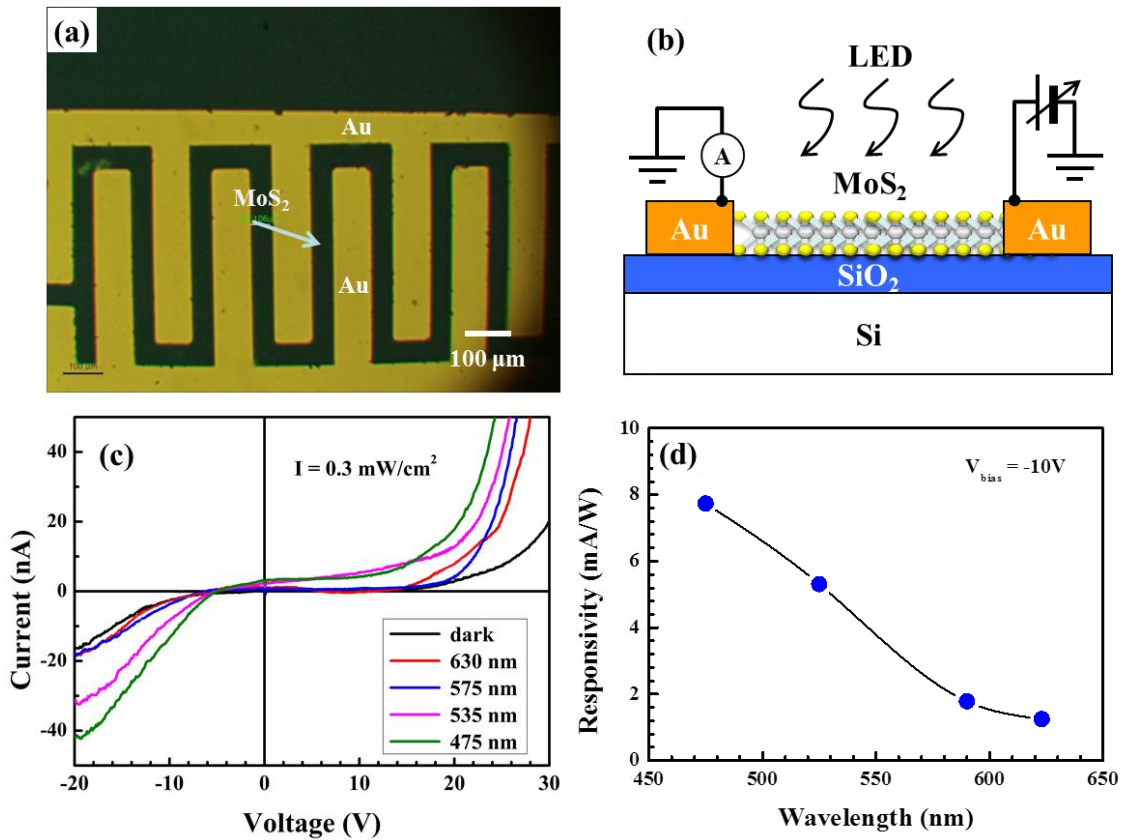


Figure 2-3: (a) An optical image of MSM photodetector device. (b) Schematic illustration of device structure shown in (a). (c) I-V characteristic curves at various illuminated wavelengths. (d) The wavelength-dependence responsivity under -10 V bias.

Besides, the photocurrent of our device is relatively low, which might be due to an existence of randomly oriented grain boundaries between electrodes. The electrode spacing of our device was 50 μm similar to the range of MoS₂ grain size, and thus the effect of grain boundaries on electrical transport should be taken into account. Recent studies employing transmission electron microscope (TEM)[41, 42] has shown that CVD-grown monolayer MoS₂ is polycrystalline. Electrical transport between two or more single crystals could probably be influenced by scattering effect due to defect sites and dislocations at grain boundary, which is proven by experimental observation[45] in case of graphene. Depending on structure of the boundary, sheet conductance decreases around 30% as opposed to pristine monolayer MoS₂[42].

The responsivity can be extracted by the relationship; $R = I_{ph}/P = I_{ph}/(I_{opt} \times A)$, where I_{ph} is photocurrent under certain applied voltage, P is input light power, I_{opt} is incident

light power intensity and A is active area of device as plotted in Fig. 2-3(d). The device exhibited the highest photoresponsivity of ~ 7.7 mA/W for monochromatic light with wavelength of 475 nm under -10 V bias. We also investigated the optical power dependence of photocurrent of monolayer MoS₂ PDs at fixed wavelength of ~ 470 nm. The photocurrent was measured while the device was biased from -10V to 20V. Fig. 2-4(a) depicts that the photocurrent increase gradually as increasing the illuminating optical power. To study the incident optical power dependence, the photocurrent was plotted according to different input optical power at -5V and -10V, respectively as depicted in Fig. 2-4(b). The photocurrent under fixed applied voltage exhibits linear relation with incident optical power. This relation is well expressed by the equation[46]: $I_{ph} = (qnv_d)W \cdot D = A \cdot P_{opt}$ where, q is electronic charge, n carrier concentration, v_d is carrier drift velocity, W is channel width, D is absorption depth, A is fitting parameter, and P_{opt} is incident optical power. Such linear relation indicates that the photo-generated carrier is the only factor that contributes to the magnitude of photocurrent under illumination condition in our device.

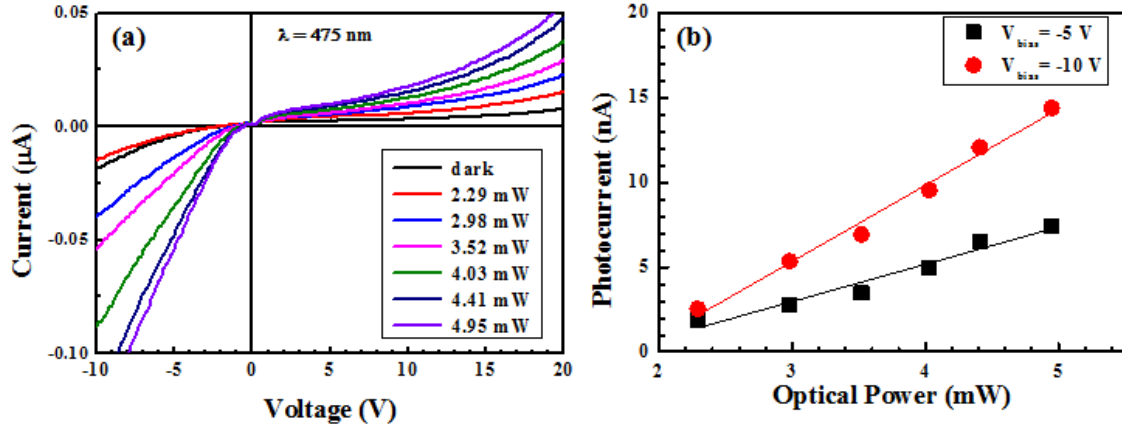


Figure 2-4 (a) I-V curve at various optical powers at 475 nm. (b) Photocurrent dependence of input optical power at constant bias voltage, -5 V and -10 V.

The photoresponse measurement was performed by employing monochromatic light with wavelength of 475 nm. Fig. 2-5(a) shows the switching characteristic of monolayer MoS₂ PDs at modulated frequency of 0.1 Hz. The current increases to high value (ON state) ~ 0.3 nA and then decreases to low value 0.15 nA (OFF state) when switching on and off the input light alternatively. Moreover, the photocurrent increases with increasing applied voltage under constant optical power density as shown in Fig. 2-5(b). The photocurrent changes from

~0.05 nA to 0.5 nA as the applied bias voltage increase from -2.0 V to -3.0 V. Such behavior suggests that a fraction of photo-generated carriers was not supplied with enough energy from the electric field to avoid recombination when biased voltage is low. The rise time is defined as the period time when current increases from 10% to 90% of photocurrent. Similarly, the fall time is the period times when current drops from 90% to 10% of photocurrent. In case of our device, the rise and fall time were 1.0 s and 0.7 s, respectively, as shown in Fig. 2-5(c). The fall time has two exponential including the fast and slow component, possibly caused by trapping effect. Under the illumination condition, the fraction of photo-generated carriers are collected by electrode under the electric field created by biased voltage while the other photo-generated carriers are trapped by the point defects or charged impurities existing on the surface of monolayer MoS₂. This trapping process gives rise to the increase in recombination lifetime of charge carriers and prolongs traveling time to counter electrode. Since the trapping process occurs slowly, thus the device has long time response. This similar trend is also observed in the previous reports[47, 48].

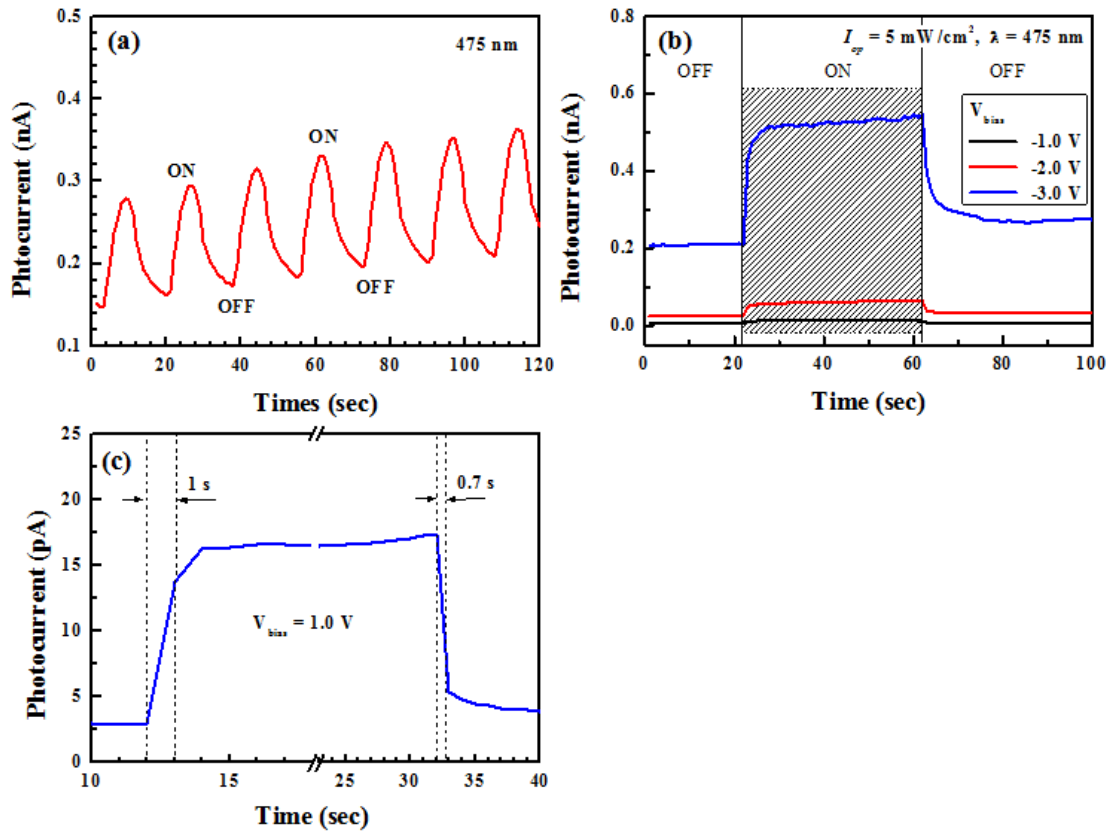


Figure 2-5: (a) Photoresponse curve of the device. (b) Photoresponse measured at various

applied bias voltage -1 V, -2 V and -3 V. (c) The response time is defined as the time when current increase from 10% to 90% of the photocurrent and the recovery time is defined as the period time when current decrease from 90% to 10% of the photocurrent as shown.

2.4 Chapter summary

In summary, MoS₂ thin film was synthesized by direct sulfurization method. Optical images, AFM image, Raman and PL characterization showed that the MoS₂ film is quality monolayer form. The *I-V* and photoresponse measurement showed monolayer MoS₂ based photodetector to have good photoresponsivity of ~7.7 mA/W for wavelength of 470 nm with the rise and fall time of ~1.0 s and 0.7 s, respectively. The degradation of photocurrent caused by the grain boundaries requires further in-depth study to fully understand the electrical transport mechanism.

Chapter 3: Near bandgap second-order nonlinear optical characteristics of MoS₂ monolayer transferred on transparent substrates

3.1 Introduction:

3.1.1 Overview:

Two-dimensional (2D) transition metal dichalcogenides (TMDCs) offer a new window into infinitesimally thin materials where the fabrication process can be precisely tuned on an atomic scale. These 2D materials, especially in the form of a monolayer, have shown outstanding electrical, structural, and optical properties as they have been used to demonstrate high on/off ratio transistors, integrated circuits with the logic operation, as well as chemical and gas sensors.[49, 50] By exploiting the fact that the conduction/valence band of these materials can possess two minima at equal energies, but different positions in momentum space, they can also be utilized for a new type of electronic switching known as valleytronics.[51, 52]

The mechanical strength and flexibility of 2D TMDCs, along with the ability to stack them and create atomically thin heterojunctions, shows strong potential for use in flexible electronics and field effect transistors.[53, 54] 2D heterostructures which can be prepared for printable electronics have exhibited unprecedentedly large and tunable electrical resistance making them ideal for memristive and memcapacitive switches,[55] however ultrathin TMDC monolayer devices that require flexibility, stretchability, and/or transparency are most promising.[56] Their ability to withstand enormous amounts of strain makes them wonderful candidates for piezotronic devices where their electronic properties can be tuned via stress/strain.[57]

3.1.2 Motivation:

As a bottom-up approach, the chemical vapor deposition (CVD) process allows for the fabrication of large-area, high-quality (electronic/structural) TMDC monolayers.[58] In some cases, the CVD process yields monolayers whose electronic properties rival that of the best mechanically exfoliated monolayers.[59] As a TMDC whose bandgap becomes direct

with *inversion symmetry breaking* in the monolayer limit, MoS₂ has been getting ample attention for its strong second-order nonlinear optical (NLO) properties.[60-64] Being limited by the atomically thin NLO interaction length, however, monolayered MoS₂ is considered impractical for efficient wavelength conversion. Unfortunately, simply increasing the number of layers cancels out coherent NLO responses from successive layers because of typical Bernal stacking.¹⁴ Recently, a breakthrough was made by the capability of spiral multilayer stacking where second harmonic generation (SHG) was shown to be enhanced by almost two orders of magnitude for three-dimensional MoS₂ spirals ($N \sim 15$).[65] However, the pyramidal stacking structure renders the area of the multilayer to be a few μm^2 , still seriously limiting its practical use.

We note that TMDC monolayers are typically grown on “opaque” substrates such as SiO₂/Si for the compatibility issue with the existing electronics. However, the 2D TMDC must be available on “transparent” substrates, because efficient wavelength conversion requires coherent, accumulative overlap between fundamental and NLO radiation throughout an NLO crystal in the “transmission” mode. As a preliminary step, therefore, we have realized CVD-grown MoS₂ monolayers transferred on transparent substrates. The transparency of the monolayer samples allowed us to probe wavelength-dependent SHG near exciton resonance using both reflection and transmission geometry. Our SHG measurements clearly indicate that the additional transfer process of MoS₂ monolayers does not deteriorate the intrinsic NLO properties of MoS₂. We believe that our results are important in future endeavors to enhance the NLO efficiency of the 2D TMDC systems in general, especially under confinement such as an optical ring resonator or a Fabry-Pérot cavity.[66-68]

3.2 Results and discussion

Large-size monolayered MoS₂ flakes and films were first grown onto 300-nm-thick SiO₂/Si substrates via atmospheric pressure CVD in a hot wall furnace. The synthesis can be described as follows: a graphite crucible containing high-purity sulfur powder (99.5%, Alfa) was placed inside a 2-inch-diameter quartz tube and maintained at 300°C. Meanwhile, another graphite crucible containing high-purity MoO₃ powder (99%, Aldrich) was placed downstream and separately heated up to 830°C with a heating rate of 25°C/min. The

substrates were flipped upside down and mounted above the MoO₃ crucible by a quartz holder. During the growth, the tube was constantly fed by a 10 sccm high-purity N₂ carrier gas and the optimal chamber pressure was found to be ~ 500 Torr.

The frequently used polymethyl methacrylate (PMMA) method was employed to transfer a CVD-grown MoS₂ monolayer onto a commercially available fused silica substrate. The as-grown MoS₂ onto SiO₂/Si substrate was initially coated with PMMA via spin coating at two steps: 500 rpm for 10 s and 3000 rpm for 60 s. After spin coating, the sample was softly baked at 120°C for 10 min. The sample was dipped into 2 M KOH solution at ~ 100°C until the polymer-supported film detached from the substrate and floated on the surface of the KOH solution. The floating film was pulled out of the solution and cleaned thoroughly with DI water. The film on the fused silica was baked at 120°C to expel any air/water vapor trapped between the film and substrate. Finally, the PMMA was removed with acetone for 30 min to expose the raw MoS₂ surface. For MoS₂ on the polyethylene terephthalate (PET) substrate, we used dilute hydrogen fluoride (HF) acid to slowly etch out the SiO₂ layer of the as-grown MoS₂. Firstly, the as-grown sample was mechanically clamped with a fresh PET substrate on the upper side by a polyester clip. Then both were immersed in a 1% HF solution for 5 min. The SiO₂ layer was instantly attacked by the HF acid leaving the MoS₂ monolayer on the PET substrate. The transferred MoS₂ was taken out of solution and rinsed with DI water, then baked at 100°C for 10 min to enhance adhesion between MoS₂ and the new substrate.

As-grown and transferred MoS₂ flakes or films were initially inspected using an optical microscope (Nikon system). The morphology was also checked through field emission scanning electron microscopy (JEOL JSM-7500F, accelerating voltage of 5.0 KV, operated in SEI mode). Macro-Raman spectra were taken using 514.5 nm radiation from an Ar⁺ laser (Melles Griot, 35-LAP-431-220) as an excitation light source at room temperature. The laser-spot size and power on the sample were ~ 100 μm in diameter and less than 10 mW, respectively. A single-grating spectrometer with a focal length of 50 cm (Princeton Instruments, SP-2500i) and a liquid-nitrogen-cooled silicon charge-couple device (CCD) detector (Princeton Instruments, Spec-10) was used to analyze scattered light from the sample. The acquired Raman shift was calibrated with the Neon calibration lamp (Newport,

6032). Room-temperature photoluminescence (PL) spectra were taken using 532-nm radiation from a Shanghai Dream Green Laser Module (average power > 50 mW) with a beam diameter of $\sim 70 \mu\text{m}$ near the edge of the MoS_2 sheet. The PL signal was collected with a combination of lenses and focused onto a fiber optic bundle coupled to a selective-grating Horiba iHR320 spectrometer equipped with a CCD camera.

First, we utilized the optical microscope (OM) and scanning electron microscope (SEM) to visualize the surface morphology of MoS_2 on the transparent substrates. Figures 3-1(a) and (b) show the OM images of MoS_2 on fused silica and on the PET substrate, respectively. Both images were taken at the edge of the film where individual flakes can be clearly observed. The inset in Fig. 3-1(a) is a prototype SEM image of transferred MoS_2 flakes on the fused silica. The single crystals of MoS_2 (darker area) retain their size ($\sim 50 \mu\text{m}$) and triangular shape with sharp edges after transfer when compared to the as-grown MoS_2 on SiO_2/Si shown in Fig. 3-1(c). The small black dots sporadically scattered over the OM images are the nucleation seeds, arising from the CVD growth technique whereas larger dark spots are bulk MoS_2 . As for the CVD-grown MoS_2 on SiO_2/Si , the thickness of the layer was determined by an atomic force microscope (AFM, MFP-3D) and the height profile is shown in Fig. 3-1(d) along with an averaged scan trace (solid red line). The dotted red lines indicate the starting and end line of the scan area over which the cross section profiles were averaged. The AFM measurement was performed in the tapping mode with a cantilever of $k \sim 1.8 \text{ N/m}$ and a scan frequency of 0.5 Hz. The measured layer thickness was found to be $\sim 0.9 \text{ nm}$. Although this value is slightly thicker than the theoretical value for the monolayer ($\sim 0.6 \text{ nm}$), we expect that this discrepancy is commonly observed in CVD-grown MoS_2 monolayers as well as graphenes on SiO_2/Si substrates; this is possibly caused by the existence of adsorbents under the film.[69] Note here that thickness determination by AFM is not particularly informative for the transferred samples because the measured height profile can be directly affected by a gap between the monolayer and the substrate.

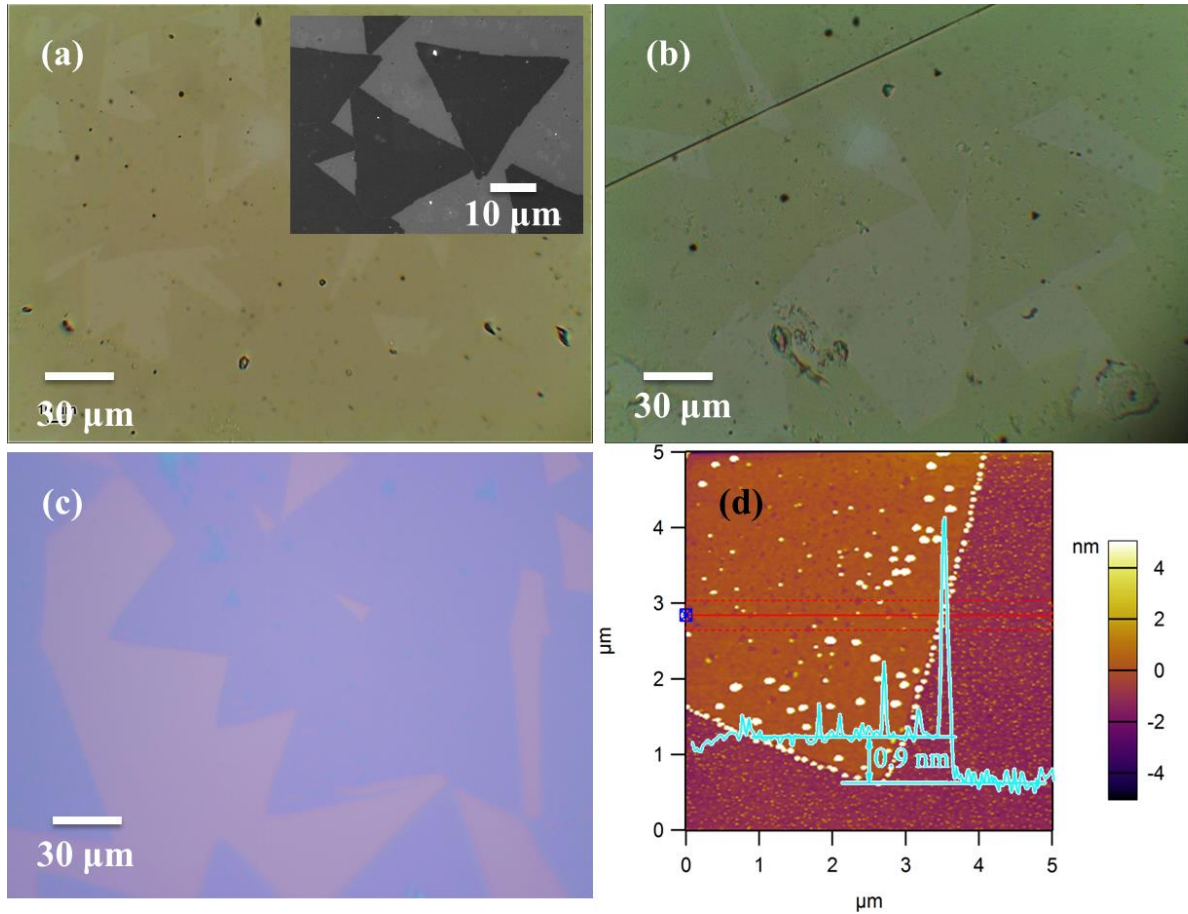


Figure 3-1: OM images of transferred MoS₂ on (a) fused silica, (b) flexible PET substrate and (c) as-grown MoS₂. Inset: SEM image of MoS₂ on fused silica. (d) AFM image (scan range; 5 × 5 μm²) and its thickness profile at the edge of the as-grown MoS₂ flake. For clarity, the height profile is plotted across the boundary between the MoS₂ flake and substrate.

Therefore, we further performed macro-Raman and PL measurements on the MoS₂ samples in order to confirm the layer number and the consistency of intrinsic properties of the film before and after the transfer process. For comparison, Raman spectra from MoS₂ on SiO₂/Si, fused silica, and PET are presented in Fig. 3-2(a). The peak located at ~ 385 cm⁻¹, is attributed to in-plane vibrational mode E_{2g}^1 where the oscillation of top and bottom sulfur layers is confined to the basal plane and opposes the motion of the Mo atoms. The other peak near ~ 407 cm⁻¹ is assigned to the out-of-plane vibrational mode A_{1g} which involves the two sulfur layers oscillating out of phase and in the direction perpendicular to the basal plane while the Mo atoms remain stationary. The peak difference $\Delta\omega$ between these Raman peaks

is widely used to identify the number of layers. Raman spectra show $\Delta\omega$ values are $\sim 21.4 \text{ cm}^{-1}$ for MoS₂ on both the fused silica and PET substrates, which are similar to that of MoS₂ on the SiO₂/Si substrate $\sim 21.2 \text{ cm}^{-1}$. According to the correlation between $\Delta\omega$ and layer number in previous studies for CVD-grown MoS₂,^[70] the thickness of transferred MoS₂ films on the transparent substrates lies between the monolayer and bilayer range. Since Raman data was measured towards the edge of the sheet where the MoS₂ film consists of many grain boundaries, these experimental values of $\Delta\omega$ can be understood considering the beam size of $\sim 100 \text{ }\mu\text{m}$ which can cover two adjacent flakes with some overlap forming a bilayer near the grain boundary.

The PL spectra of MoS₂ on SiO₂/Si as well as fused silica and PET are plotted for comparison in Fig. 3-2(b). Since the PET substrate exhibited a PL signal of its own, we performed a spectral subtraction to isolate the PL of MoS₂ (see Supplemental Materials for details). The peak position of the A-exciton in the MoS₂ film on SiO₂/Si is centered at $\sim 675 \text{ nm}$ (1.84 eV). The estimated bandgap agrees well with the direct bandgap of monolayer MoS₂ on SiO₂/Si found in previous studies.^[71] However, for the MoS₂ on fused silica and PET, the A-exciton peak position is blue-shifted to $\sim 663 \text{ nm}$ (1.87 eV). Such a significant blue-shift for transferred MoS₂ monolayers is well known and consistent with Ref [72].

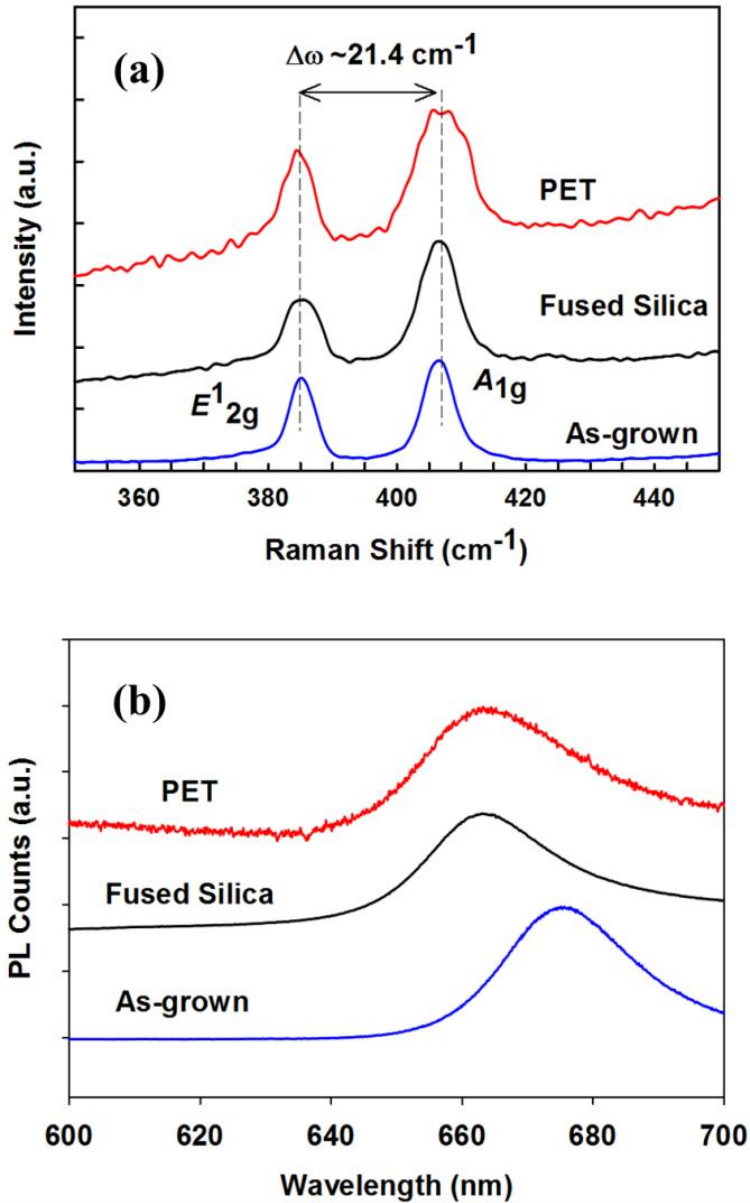


Figure 3-2: (a) Raman and (b) PL spectra of as-grown MoS₂ on SiO₂/Si and both transferred samples (fused silica and PET substrates).

Details on the experimental setup of NLO experiments can be found in Supplemental Materials. A broadband SHG measurement was conducted in order to provide the $\chi^{(2)}$ dispersion of the material. The transmitted (T) and reflected (R) SHG signals of the monolayers on transparent substrates were simultaneously monitored. The excitation beam spanned a spectral range of $\lambda = 1064 - 1600$ nm. Therefore, the detected SHG range

encompasses both the A - and B -exciton states. As an initial calibration, we measured the T and R SHG signals from a bulk z -cut quartz crystal. As predicted, the SHG ratio $T/R \sim 25$ was confirmed over the experimental λ range as shown in Fig. 3-3. After quartz calibration, we measured the T and R SHG from monolayered MoS_2 as a function of λ and the corresponding SHG spectra were shown in Fig. 3-3. A spot near the edge of the MoS_2 films was excited since this region was most likely monolayer and did not contain any overlapping grains. Spectral Maker fringes are not expected to manifest themselves in the broadband SHG data of MoS_2 since the monolayer thickness is much smaller than the excitation wavelength. Therefore, strong SHG dispersion should be interpreted in terms of two-photon resonance as shown in Fig. 3-4.

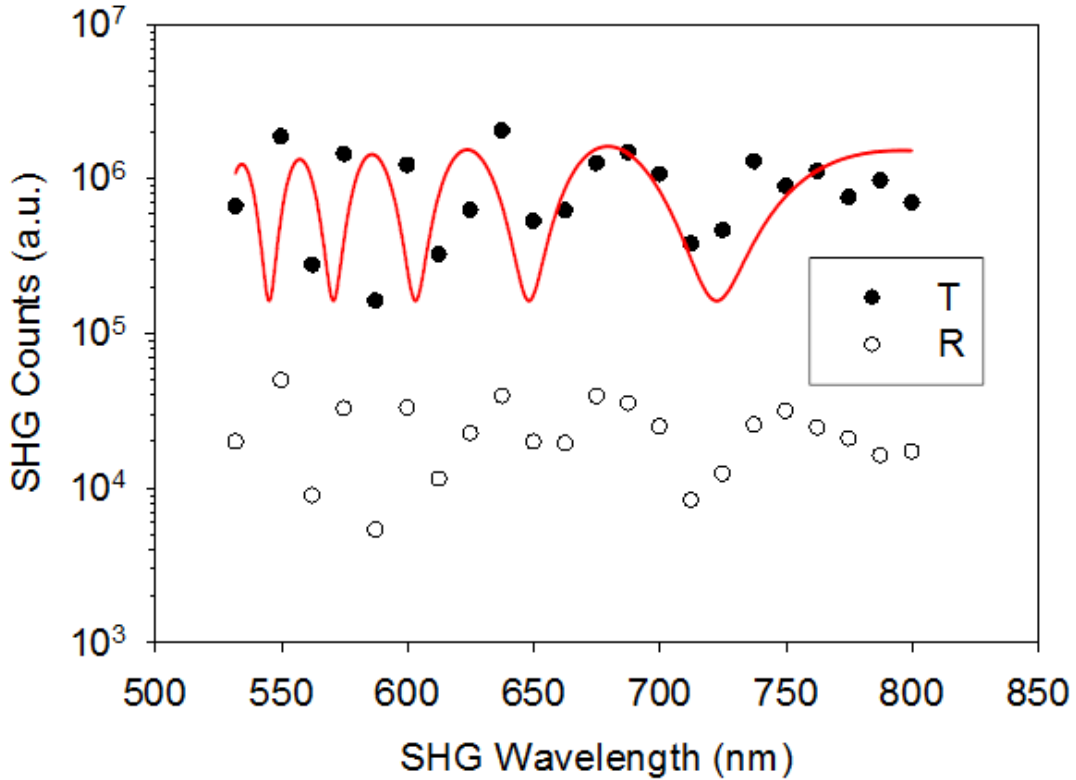


Figure 3-3: Broadband SHG responses of single-crystal quartz in transmission (dots) and reflection (circles) modes. The red plot overlaid on the transmission data is a bulk SHG fit that takes into account the spectral Maker fringe effect.

First, we examined the λ -dependent SHG measured by T and R . If treated as a thin polarized sheet embedded between two dielectric media, the T/R ratio is expected to be

independent of the MoS₂ dielectric function. Instead, the ratio only depends on the refractive indices of the two surrounding media via $(n_2/n_1)^3$, where $n_2 \sim 1.5$ is the refractive index of the substrates (both fused silica and PET) and $n_1 \sim 1$ is the refractive index of air within our λ range.[29, 73] Therefore, a constant ratio of $T/R \sim 3.4$ is predicted. At $\lambda/2 = 800$ nm, the measured T/R ratio was 3.0 for MoS₂ on fused silica and 2.7 for MoS₂ on PET which agree reasonably with the theoretical prediction. However, when λ was tuned such that the corresponding SHG overlaps with the *A*- and *B*-exciton lines, the T/R ratio drops as indicated by the red traces in Fig. 3-3. While the effect is partially extrinsic as indicated by the difference in the variation range of the T/R ratio for the two samples, it seems to arise at two-photon resonance of SHG at exciton levels where T is reduced by excitonic absorption or R is enhanced by resonant reflection.[74] A precision measurement is required to resolve the issue using a *directly grown* MoS₂ on the transparent substrates to eliminate any extrinsic effect arising from the transfer process. More importantly, we believe that “transparent MoS₂” can be exploited to further enhance the SHG process since both the forward and backward SHG signals can accumulate via constructive interference through multiple passes within a confined cavity or a stacked structure.

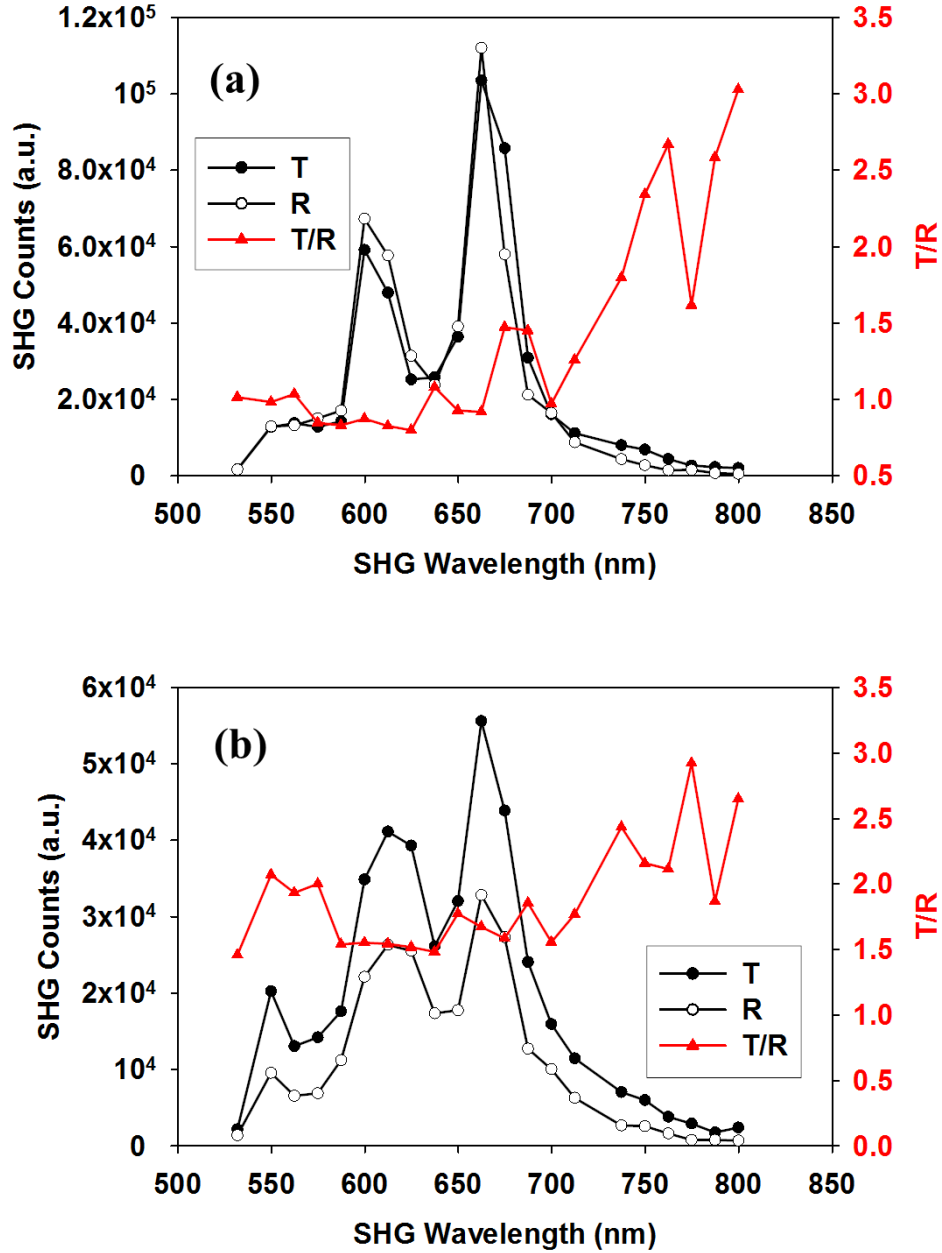


Figure 3-4: Broadband SHG response of (a) MoS₂ on fused silica and (b) MoS₂ on PET with two collection geometries. The red trace is a ratio of transmitted to reflected SHG.

The *z*-cut quartz (~ 0.65 mm thick) was also used as a reference material for calculating $\chi^{(2)}$ from the measured MoS₂ SHG signal. As previously mentioned, the monolayer was modeled as a polarized sheet embedded between two dielectrics[75, 76] and the quartz was modeled as bulk. Under these assumptions, Eq. (1) can be used to calculate the *absolute* $\chi^{(2)}$ dispersion of monolayered MoS₂

$$\chi_{\text{MoS}_2}^{(2)} = \frac{\chi_q^{(2)} [n_q(\omega) + 1]^3}{16\pi\Delta h\Delta k_q n_q(\omega) n_q^{1/2}(2\omega)} \left(\frac{\lambda}{\lambda_q} \right) \left(\frac{I_{\text{MoS}_2}(2\omega)}{I_q(2\omega)} F_q \right)^{1/2} \quad (1.10)$$

where $\chi_q^{(2)} = 0.6$ pm/V,[77] $n_q(\omega)$ and $n_q(2\omega)$ represent the linear refractive indices of quartz at frequency ω and 2ω respectively, $\Delta h \sim 0.9$ nm is the thickness of the monolayer, Δk_q is the phase mismatch in quartz calculated from the refractive indices, and $I_{\text{MoS}_2}(2\omega)$ is the SHG intensity from the monolayer. λ_q is the wavelength within the probed spectral range where the SHG intensity from quartz (I_q) is a maximum, and λ represents the experimentally tuned wavelengths. Thus, at wavelength λ_q , a constructive spectral Maker fringe occurs in bulk quartz and $\sin^2(\Delta k_q L_q/2) = 1$ within the phase-matching factor.[78] No wave vector mismatch effects are taken into account for the monolayer since $\Delta h \ll \lambda$. F_q in Eq. (1.10) represents the Fresnel coefficient of quartz which needs to be taken into account when comparing reflection/transmission geometry. For example, the ratio of transmitted SHG intensity to reflected SHG intensity for reference quartz should be 25.

Figure 3-5 shows the $\chi^{(2)}$ dispersion obtained from the measured SHG intensities of the MoS₂ sheet on fused silica and on the PET substrate using Eq. (1). The solid red lines in both plots represent the PL spectra from Fig. 3-2(b) taken under continuous wave excitation. At $\lambda = 1600$ nm, where the dielectric function is purely real, $\chi^{(2)}$ of the MoS₂ monolayer sheet on fused silica was measured to be 6.3 pm/V and $\chi^{(2)}$ of MoS₂ on PET is 7.0 pm/V. With proper corrections to previous work, we found that $\chi^{(2)}$ of MoS₂ transferred on transparent substrates is on par with $\chi^{(2)}$ of as-grown samples on SiO₂/Si substrates confirmed both in reflection and transmission geometry. It is interesting that both MoS₂ on fused silica and PET samples exhibit two-photon resonant enhancement in $\chi^{(2)}$ near the spectral positions of the *A*- and *B*-excitons. Compared to the long-wavelength limit, $\chi^{(2)}$ of the MoS₂ sheet on fused silica can be enhanced by $\sim 7.2 \times$ and $\sim 4.0 \times$ for MoS₂ on PET near the spectral position of the *A*-exciton. The *B*-exciton resonantly enhances the static $\chi^{(2)}$ value by $\sim 5.0 \times$ for MoS₂ on fused silica $\sim 3.3 \times$ for MoS₂ on PET.

A slightly weaker resonance effect at the *B*-exciton line is indeed theoretically predicted – see Fig. 3(a) of Ref.[64] which properly takes into account the excitonic effect. This theory also predicts that the resonance effect is about 3 times stronger at the *C*-exciton line (~ 2.9 eV). We note that the measured $\chi^{(2)}$ values of ~ 40 pm/V at the *A* exciton

resonance from our transferred samples are therefore consistent with Ref. [61], reporting $\chi^{(2)} \sim 100$ pm/V at the C-exciton resonance of an “exfoliated” MoS₂ monolayer. This implies that the NLO quality of our synthetic samples is also on par with that of an exfoliated MoS₂.

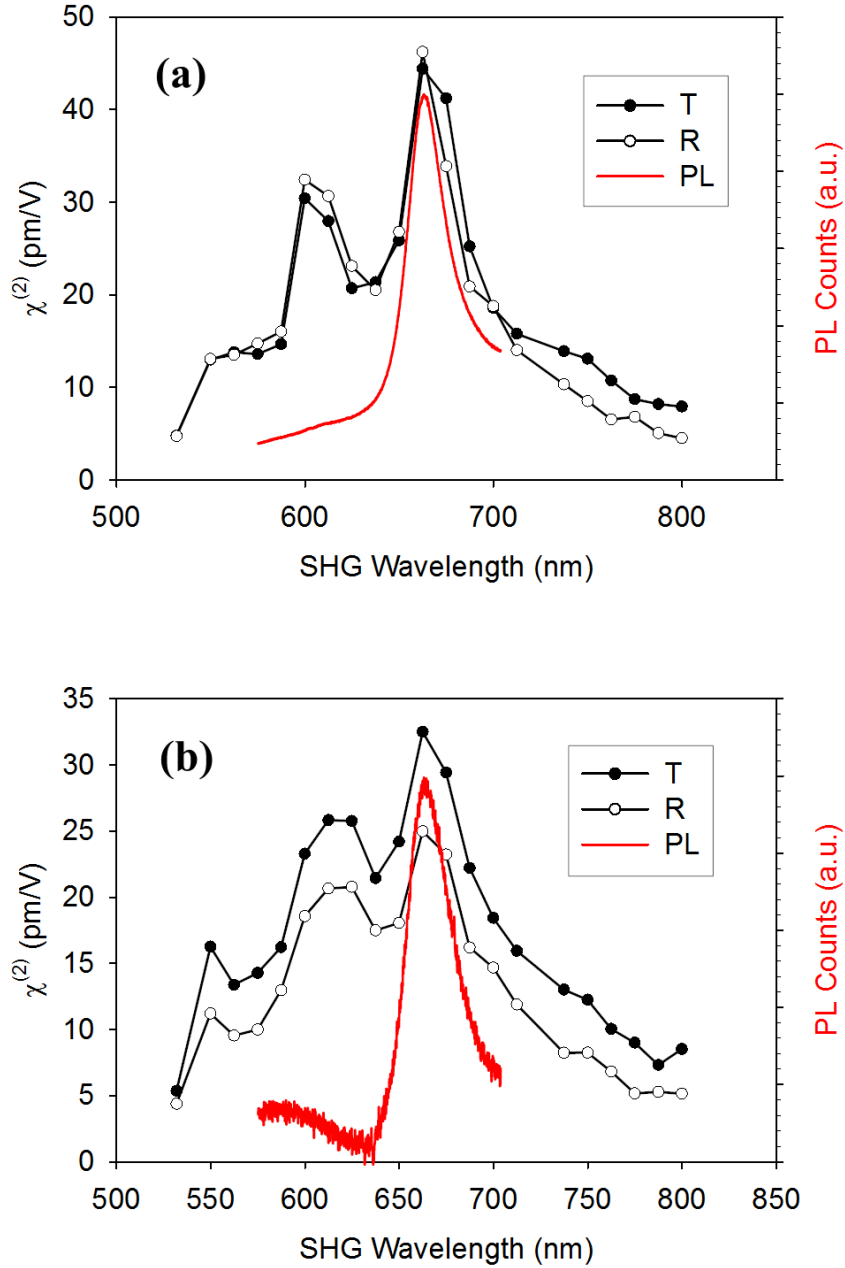


Figure 3-5: $\chi^{(2)}$ dispersions calculated based on transmission and reflection geometries from (a) MoS₂ monolayer sheet on a fused silica substrate and (b) MoS₂ monolayer sheet on a PET substrate. The red traces are the corresponding PL spectra from Fig. 3-2(b), confirming two-

photon exciton resonance of SHG.

3.3 Chapter summary

We have provided a comprehensive second-order NLO characterization of CVD-grown MoS₂ monolayers transferred onto transparent substrates. A measurable blue-shift of the exciton levels were confirmed by both PL and SHG measurements. MoS₂ exhibits two-photon resonant enhancement of $\chi^{(2)}$ near the *A*- and *B*- exciton states and the corresponding absolute $\chi^{(2)}$ values are comparable with that of a typical CVD-grown monolayer. We have also shown that the SHG intensities from “transparent” MoS₂ monolayers are comparable both in the forward and backward directions, which is consistent with a nonlinear sheet model. Our future work is to design and fabricate stacked structures by either transfer or direct growth on transparent substrates that can be confined within a cavity and resonant with excitonic states in order to realize the maximum SHG efficiency attainable.

Chapter 4: Nonlinear optical characteristic of monolayered MoSe₂

4.1 Introduction

4.1.1 Overview

High demand on miniaturizing optoelectronic devices has encouraged researchers to discover new active materials that can potentially overcome the scaling limitation of current Si-based technology. In recent years, atomically thin transition metal dichalcogenides (TMDCs), MX₂ (M = Mo, W; X = S, Se), have emerged as promising alternatives due to their appealing dimensionality-dependent electrical, mechanical and optical properties.[79] Structurally, TMDCs consist of a network of weakly bonded X-M-X layers via van der Waals coupling, where one array of hexagonal lattice of transition metal atoms is sandwiched between two arrays of hexagonal lattice of chalcogen atoms. For example, MX₂ can crystallize with the centrosymmetric D_{6h} space group for 2H stacking.[80] When they are thinned down to the monolayer regime, the electronic band structures of TMDCs experience a fascinating evolution from indirect bandgaps to direct bandgaps.[28] This electronic modification is also accompanied with inversion symmetry breaking and strong two-dimensional (2D) confinement under reduced dielectric screening, leading to intense light emission,[81] room-temperature excitonic effects,[82, 83] as well as strong second harmonic generation (SHG).[84-89] These unique properties makes monolayers more attractive to numerous applications such as photodetectors, [13, 90] valleytronics where the device switching mechanism is based on two non-equivalent K/K' points in the Brillouin zone [91, 92] as well as nonlinear optics.[93]

Many different tactics have been used to thin down TMDCs into monolayers. Some of the most common methods include mechanical and electrochemical exfoliation,[94] sulfurization/selenization of pre-deposited oxide or metal films,[52] and chemical vapor deposition (CVD).[13, 95, 96] Mechanical exfoliation is a well-known approach for producing superior quality monolayers; however this process generally produces small-area crystals which is a major limitation for practical applications. In contrary the CVD process yields large-area, continuous monolayer TMDCs for mass production. Although there has

been much progress on growth of monolayer TMDCs in recent years,[97] the growth of large-area, high-quality monolayer MoSe₂ is limited due to the lower chemical reactivity of selenium as compared to sulfur.[98] The controlled growth of high-quality Se-containing TMDCs is essential for the development of atomically thin TMDC-based NLO devices working at infrared.

4.1.2 Motivation

As noncentrosymmetric materials with direct bandgaps, TMDC monolayers are theoretically predicted to exhibit strong second-order nonlinear susceptibility $\chi^{(2)}$ in comparison with their bulk counterparts.[64, 99, 100] Experimentally, MoS₂ and WS₂ monolayers have been proven to possess large $\chi^{(2)}$ values.[84, 88, 89] In contrast to well-studied MoS₂ and WS₂, however, there are only a few available reports on the NLO properties of MoSe₂. [101] For example, using circularly polarized radiation, Dong *et al.* has experimentally investigated the SHG responses for mechanically exfoliated mono- and few-layered MoSe₂ within a limited fundamental wavelength $\lambda = 1500 - 1700$ nm.[86] More recently, Wang *et al.* studied exciton states in monolayer MoSe₂ using two-photon spectroscopy across Rydberg excitonic levels. However, none of these studies report on the key NLO parameter of MoSe₂. Experimental confirmation of the absolute nonlinearity of MoSe₂ is particularly important, because the existing theories[99, 100] predict larger optical nonlinearity, compared with that of the sulfide analog.

In order to contribute to the comprehensive picture of the NLO properties on TMDC group of materials, we investigated the NLO characteristics of MoSe₂ in its monolayer form. Our high-quality MoSe₂ crystal was obtained by selenizing the pulsed laser deposited (PLD) MoO₃ film on a SiO₂/Si substrate. For the first time, to the best of our knowledge, we provide an estimation of the absolute $\chi^{(2)}$ value using the “polarized sheet” model.[89] Our unique broadband capability enabled us to study steeply varying SHG dispersion across the two major exciton levels involved in direct optical transition, when the fundamental wavelength was tuned over a wide spectral range of $\lambda = 1200 - 1800$ nm. Additionally, a high laser induced damage threshold (LIDT) was also determined for MoSe₂ in comparison with a MoS₂ monolayer at the fundamental Nd:YAG radiation ($\lambda = 1064$ nm and $\tau = 30$ ps), demonstrating their persistence against high-power laser flux.

4.2 Experimental methods

Raman and photoluminescence (PL) spectra were measured at room temperature using an argon Ar⁺ laser (Melles Griot, 35-LAP-431-220) with 514.5-nm excitation light and a spot size of approximately ~ 10 μm on the sample. The scattered Raman and luminescence signals from the sample were dispersed by a single-grating spectrometer (Princeton Instruments, SP-2500i) with a 50-cm focal length, and then detected with a cooled liquid-nitrogen CCD detector (Princeton Instruments, Spec-10). The recorded wavelength and Raman shift of the scattered light was calibrated by a standard Neon calibration lamp (Newport, 6032).

The NLO measurement was conducted using a picosecond EKSPLA Nd:YAG laser (30 ps temporal pulse width) with a 50 Hz repetition rate. The main output of the laser ($\lambda = 1064$ nm) synchronously pumped an EKSPLA PG 403 optical parametric oscillator. The sample was mounted onto a homemade rotatable sample holder attached to three translation stages yielding precise control in the x , y , and z directions. The fundamental beam from the laser was focused to a spot size of ~ 50 μm in diameter using a $10\times$ microscope objective lens. The reflected SHG beam was then guided to collection optics via a beam splitter and focused onto a fiber bundle. The bundle was coupled to a selective grating Horiba iHR320 spectrometer equipped with CCD camera. The experimental irradiance was ~ 0.9 GW/cm^2 , which is well below the optical damage thresholds for the monolayer. A halogen lamp coupled to a fiber cable was inserted in our setup so that the MoSe₂ flake could be located with a CMOS camera (Thorlabs) in a reflection microscope scheme.

When measuring the polarization-dependent SHG, a half-wave plate was used to select the polarization state of the fundamental beam tuned to 1280 nm while a detection analyzer in front of the detector was adjusted to be either parallel or perpendicular to the polarization state of the input beam. The isolated monolayer MoSe₂ flake was then rotated through 360° in 10° steps for both configurations of parallel and orthogonal polarization measurements.

4.3 Result and discussion

The monolayered MoSe₂ flakes were prepared by two-step growth mechanism, as

schematically shown in Fig. 4-1 (a) and (b). The first step involves the synthesis of Molybdenum trioxide (MoO_3) thin film 300 nm thick SiO_2/Si substrate by pulse laser deposition (PLD) technique (Fig. 4-1a). Highly pure MoO_3 target of approximately 2cm in diameter was placed in rotating target holder. The substrate was fixed 25cm above the target. The pressure of the vacuum chamber was reduced to 5×10^{-7} torr. Before deposition, the MoO_3 target was exposed to the laser beam for 5 minutes to clean the contaminants aggregated on the surface of the target. For MoO_3 deposition, the laser power and repetition frequency (number of laser shots per second) were set to be 200 mJ/cm^2 and 3 Hz respectively, and the total deposition time was 60s. The deposition was carried out in ultra-high vacuum (5×10^{-7} torr) without any carrier gas. A krypton fluoride (KrF) excimer laser ($\lambda=248 \text{ nm}$, CompexPro 102F) with 20 ns pulse width was used for target ablation. In the second step, PLD deposited MoO_3 film was converted to MoSe_2 by selenization in chemical vapor deposition (CVD) system as illustrated in Fig. 4-1b. The selenization process was as follows: Approximately 300 mg of high pure selenium powder (Sigma Aldrich, 99.99%) in graphite crucible was placed in the furnace tube. The MoO_3 sample was placed approximately 15cm away from the selenium powder. The tube pressure was initially pumped down to the base value of 80 mtorr. The tube was repeatedly flashed with pure N_2 gas at room temperature to clean the reaction chamber (quartz tube). The chamber pressure was raised to 330 torr with 100 sccm flow rate of carrier gas (N_2) and 10 sccm of H_2 . At this point, the flow rate of N_2 was reduced to 10 sccm and H_2 to 1 sccm. The reaction chamber temperature was raised to 400°C with temperature increasing rate of $25^\circ\text{C}/\text{min}$. These conditions were maintained for 15 min. The chamber pressure and temperature were then raised to 550 torr and 850°C respectively and were maintained for 25 min. After selenization time, the furnace was naturally cool down and samples were taken out below 350°C .

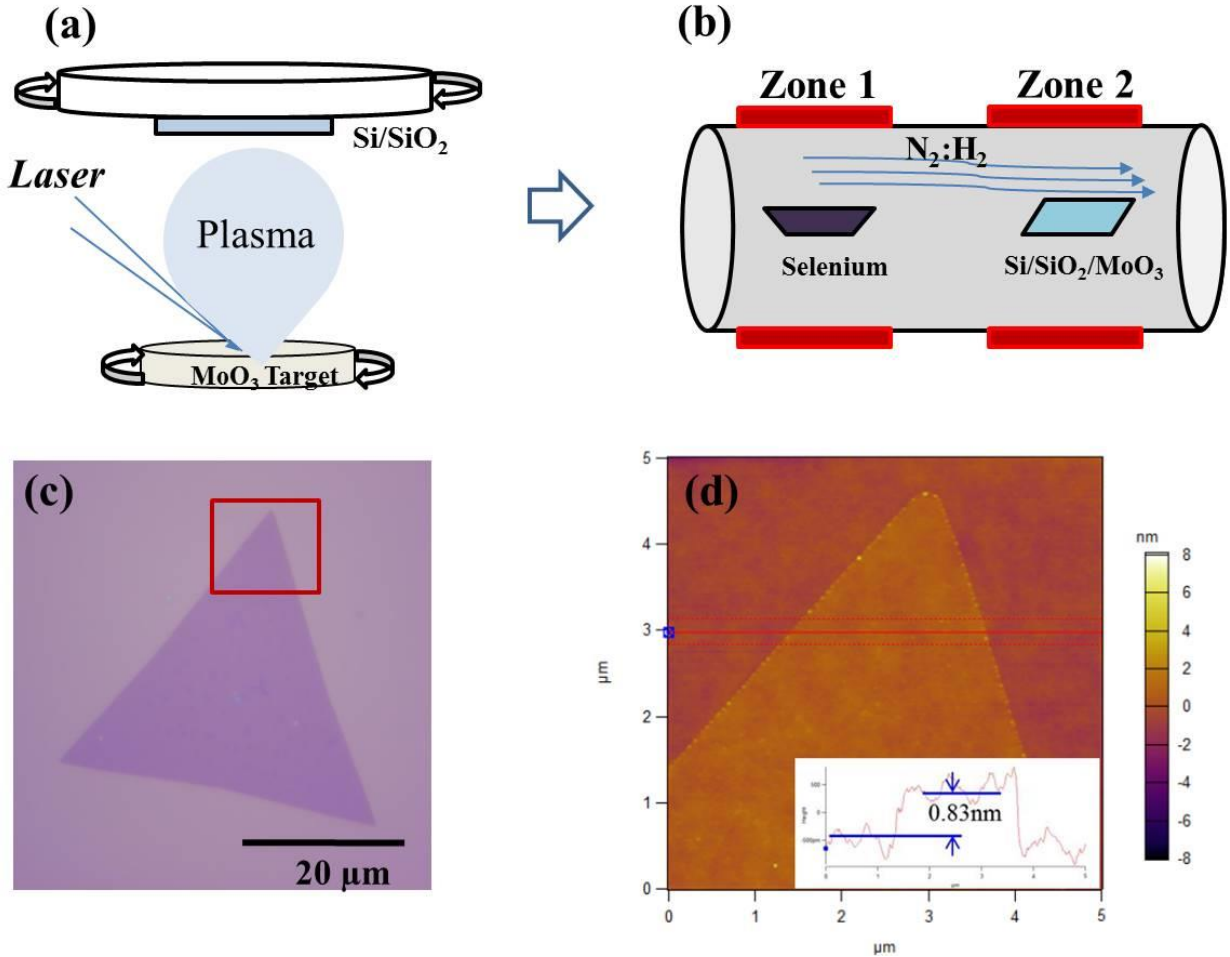


Figure 4-1: (a) Schematic drawing of two-step PLD growth mechanism PLD and (b) the furnace system for selenization of MoO₃ film. (c) OM and (d) AFM image of monolayer MoSe₂ flake from the marked region (red outlined square) in (c) and thickness profile (inset) on the SiO₂/Si substrate.

The thickness-dependent color contrast between the thin MoSe₂ flakes and the underlying 300 nm SiO₂ layer can be used for the identification of monolayer flakes. For optical characterization, an isolated, large-size (~40 μm) ML MoSe₂ flake was initially identified using an optical microscope (OM, Nikon). The OM image of the isolated triangular MoSe₂ flake is depicted in Fig. 4-1(c). The height measurement of the flake was performed by atomic force microscopy (AFM, MFP-3D). The AFM result (tapping mode with cantilever of $k \sim 1.8$ N/m, 0.5 Hz scan speed) shows that the MoSe₂ flake is a high-quality monolayer with no discernible contamination. Moreover, the thickness of the flake was found to be ~0.83 nm, which confirms that the flake is indeed monolayer [inset **Fig. 4-1(d)**].

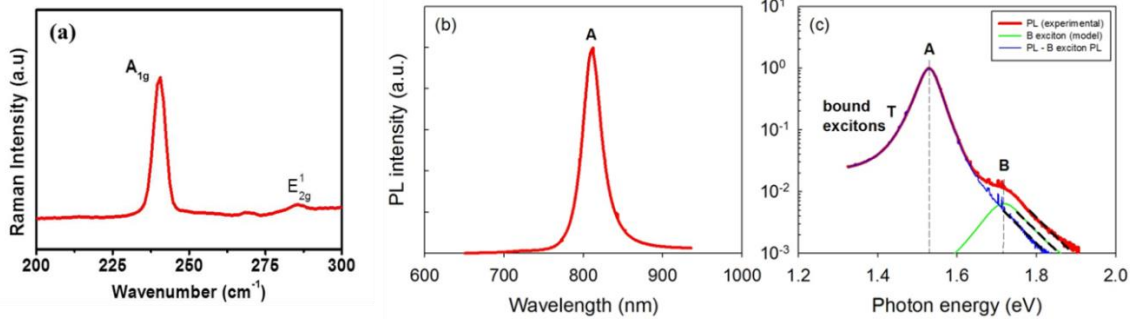


Figure 4-2: (a) Normalized Raman spectrum and (b) photoluminescence spectrum of the monolayer MoSe₂ flake. (c) Semi-log plot of the PL (red), showing A- and B-exciton levels along with lower-energy tail arising from bound excitons. The B-exciton PL (green) is modeled with a Lorentzian shape. The blue trace is the PL without the B-exciton contribution.

Raman spectroscopy has been used as an indirect method to estimate the number of layers (thickness) of two-dimensional layered materials.[43, 96] The intensities and shift in energies of the in-plane (E^1_{2g}) and out-of-plane (A_{1g}) vibrational modes strongly depend on the number of layers. The Raman spectrum of our MoSe₂ flake shows two characteristic vibrational modes, which are the A_{1g} and the E^1_{2g} peaks at 240.6 cm⁻¹ and 285.5 cm⁻¹ respectively, as shown in Fig. 4-2(a). The A_{1g} peak intensity is much higher than E^1_{2g} peak intensity, consistent with previous Raman studies on CVD-grown MoSe₂. [13, 95, 96] The wavenumber separation ($\Delta\omega$) between the two peaks is 44.9 cm⁻¹ corresponding to monolayer MoSe₂. Moreover, the full width half maximum (FWHM) of the A_{1g} peak can be correlated to the crystallinity of the film. The FWHM value A_{1g} peak of our MoSe₂ flake is 4.1 cm⁻¹, which is comparable with that of commercially available CVD-grown monolayer MoSe₂, indicating the high crystalline nature of the flake.

Another hallmark of good quality monolayer MoSe₂ is its PL response. The PL intensity of MoSe₂ decreases exponentially with increasing thickness due to its bandgap transformation from direct to indirect. As shown in Fig. 4-2(b), the as-grown MoSe₂ flake exhibits an excellent PL response at room temperature with a strong A-exciton peak at 1.53 eV, corresponding to the direct-gap transition at the K/K' point of the Brillion zone.[102] In order to examine the detailed feature of the optical transition, we plot the PL spectrum vs. photon energy ($\hbar\omega$) on a semi-logarithmic (semi-log) scale in Fig. 4-2(c), where the B-

exciton transition can be clearly observed as a high-energy shoulder. We modeled the B -exciton PL (green trace) line using a Lorentzian shape, , to accurately determined the B -exciton energy (E_B) with Γ being an empirical dephasing rate ~ 56 meV that determines the inhomogeneous broadening of the peak. As indicated by the parallel dashed lines, the fit parameters were carefully determined under a constraint ensuring the same slopes of the high-energy onset for the experimental PL (red), the modeled B -exciton PL (green), and the A -exciton PL (blue) that was obtained by subtracting the latter from the former. The spin-orbit interaction energy was calculated to be $E_{SO} = 190$ meV using a fit value $E_B = 1.72$ eV, which is approximately consistent with the reported value of 0.2 eV.[103] Interestingly, we found that the intensity ratio between the B -exciton PL and the A -exciton PL is about 0.06. This value is roughly 10 times larger than the equilibrium ratio of $\exp[-E_{SO}/k_B T] \sim 0.006$ at room temperature, which was calculated assuming the two-component exciton gas having the same radiative decay rate. The discrepancy therefore implies that A excitons have additional relaxation pathways to form bound excitons and negatively charged trions (T) via being bound to ambient defects and electrons. Our interpretation is in fact supported by the observation of broad low-energy tailing that extends to near infrared in Fig. 4-2(c).

For NLO study, an experimental setup was arranged to probe the SHG response from the flake as shown in Fig. 4-3(a) (detailed in experimental methods). Conventionally, the polarization-dependent SHG is a universal measurement to probe the crystal symmetry and orientation of NLO materials. In the bulk form, MoSe₂ belongs to D_{6h} symmetry point, which has spatial inversion symmetry, thus resulting in $\chi^{(2)} = 0$ and no allowable SHG. Meanwhile, the MoSe₂ monolayer possesses the D_{3h} symmetry without inversion center. Due to its three-fold rotational symmetry, there is only one independent component in the second-order susceptibility tensor $\chi_{MoSe_2}^{(2)} = \chi_{xxx}^{(2)} = -\chi_{xyy}^{(2)} = -\chi_{yyx}^{(2)} = -\chi_{yxy}^{(2)}$. As a result, the parallel and perpendicular components of resultant SHG intensity are expected to reflect $\cos^2[3(\theta + \theta_0)]$ and $\sin^2[3(\theta + \theta_0)]$ dependence, where θ is the angle between the mirror axis of the crystal and the electric field of the linearly polarized fundamental laser beam and θ_0 is the initial angular offset. Indeed, six-fold symmetric responses were measured when we rotated the MoSe₂ flake for normal incidence, in analogy with SHG responses for monolayer MoS₂[84, 85, 87, 89] and consistent with the previous report on monolayer MoSe₂[86] Fig. 4-3(b) exhibits the corresponding SHG intensity as a function of θ for parallel and

perpendicular components of the SHG field. This polarization-dependent SHG along with the Raman and PL spectra provide strong evidence for excellent optical and crystalline quality of our as-grown MoSe₂ monolayer.

In order to obtain the $\chi^{(2)}$ dispersion of the MoSe₂ monolayer, we performed a broadband SHG measurement using a reflection geometry. The MoSe₂ monolayer was illuminated (~50 μm diameter) using tunable picosecond laser pulses ($\tau = 30$ ps) from an optical parametric oscillator. The fundamental wavelength λ was tuned from $\lambda = 1200 - 1800$ nm in step of $\Delta\lambda = 25$ nm. This spectral wavelength range was chosen to encompass the optical band edge and monitor any potential resonance effects. A bulk z-cut quartz crystal (thickness ~0.65 mm) was used as a reference material. In our previous studies, we proposed an equation for calculating the bulk second-order susceptibility $\chi^{(2)}$ for monolayered MoS₂ on either transparent or opaque substrate, which can be generalized for TMDCs as long as the thickness of materials is much shorter than the wavelength. Therefore, the Eq(1) is still valid and can be used for calculating absolute $\chi^{(2)}$ dispersion for monolayered MoSe₂ :

$$\chi_{MoSe_2}^{(2)} = \frac{\chi_q^{(2)} [n_q(\omega) + 1]^3}{16\pi\Delta h \Delta k_q n_q(\omega) n_q^{1/2}(2\omega)} \left(\frac{\lambda}{\lambda_q} \right) \left(\frac{I_{MoSe_2}(2\omega)}{I_q(2\omega)} F_q \right)^{1/2} \quad (1)$$

where $\Delta h \sim 0.83$ nm is the thickness of the monolayer, $\chi_q^{(2)} = 0.6$ pm/V is second-order susceptibility of quartz[16], $n_q(\omega)$ and $n_q(2\omega)$ denote the linear refractive indices of quartz at frequency ω and 2ω respectively. Δk_q is the phase mismatch in quartz calculated from the refractive indices, and $I_{MoSe_2}(2\omega)$ is the SHG intensity from the monolayer. λ_q is the wavelength where the SHG intensity from quartz (I_q) reaches maximum value. At such a wavelength, spectral Maker fringe occurs constructively in bulk quartz and $\sin^2(\Delta k_q L_q/2) = 1$ within the phase-matching factor. λ denotes the experimentally tuned wavelengths. For the case of monolayer since $\Delta h \ll \lambda$, there is no wave vector mismatch effects taken into account. Note that Fresnel coefficient of quartz F_q has to be taken into account when comparing reflection/transmission geometry.

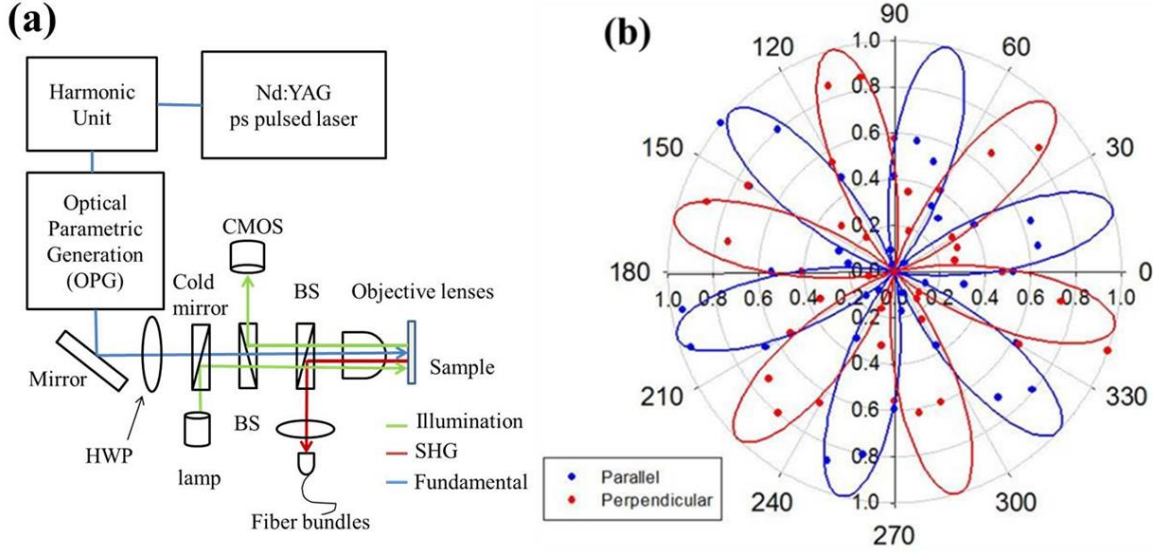


Figure 4-3: (a) Experimental setup for NLO study and (b) the azimuthal symmetry of monolayer MoSe₂ as determined by SHG polarization dependence. Parallel (blue dots) components and perpendicular (red dots) components are shown with the corresponding fitting curves (solid traces).

Figure 4-4(a) depicts the calculated $\chi^{(2)}$ dispersion from the measured SHG intensities from the MoSe₂ monolayer using Eq. (1). The solid red (dashed blue) trace is the room-temperature PL spectrum from Fig. 2(b) plotted on a linear (semi-log) scale. For comparison, the calculated $\chi^{(2)}$ dispersion for the MoS₂ monolayer from previous work is shown in Fig. 4(b)[93] with its corresponding PL spectrum (red). The $\chi^{(2)}$ dispersion of the MoSe₂ monolayer shows the following characteristics:

(i) For the short wavelengths (photon energies above the optical band edge, i.e., the A-exciton state), the $\chi^{(2)}$ is almost unchanged with a value of ~ 10 pm/V, although slight enhancement in $\chi^{(2)}$ is observed over a broad range of 640 nm – 700 nm. This effect can be attributed to two-photon resonance at *excited* exciton states. Wang et al. have also observed enhanced SHG at excited exciton levels such as X_A^{2p} ($2p$ A-exciton) and X_B^{2p} ($2p$ B-exciton) at low temperature ($T = 4$ K).[101] However, in our case, there is a noticeable redshift in the excitonic states[104] since our experiment was conducted at room temperature. Even with a large $1s$ - $2p$ splitting ~ 0.18 eV, these states are predicted to be stable at room temperature because of binding energies on the order of ~ 0.32 eV = 0.5 eV – 0.18 eV, where the ground-

state binding energy is about 0.5 eV. [105]

(ii) $\chi^{(2)}$ is maximum at the *A*-exciton resonance, which is ~ 50 pm/V. This value is about 25% greater than that of the sulfur analogue, ~ 40 pm/V[89, 93] – see also Fig. 4-4(b). Interestingly, the resonance effect in our MoSe₂ is only significant at the *A*-exciton, which is $5.0\times$ greater than those at the *B*-exciton and excited exciton states in the shorter wavelength range. We note that the recent low-temperature experiment shows an opposite trend,[101] where SHG is even stronger at the excited states than at the *1s* ground-states of both *A*- and *B*-excitons. The observed SHG dispersion of our MoSe₂ is also rather different from that observed in MoS₂ monolayers where the resonance factor at the *B*-exciton is comparable to that at the *A*-exciton as shown in Fig. 4-4(b). As evident from these rather different resonance behaviors, the SHG coupling to a specific exciton state might be a subtle process that can even be possibly affected by extrinsic factors. Clearly, more experiments should be conducted to understand the overall SHG resonance across the major exciton states using MoX₂ monolayers prepared under different conditions.

(iii) Most interestingly, two significant features seem to clearly manifest themselves at and even *below* the optical band edge. While the sharp SHG response at ~ 806 nm stems from the *A*-exciton resonance, SHG is also strongly enhanced starting from ~ 825 nm to longer wavelengths. This quasiparticle state can be attributed to the trion state (*T*) based on the spectral separation of $28 - 35$ meV from the *A*-exciton energy, which is consistent with the reported trion binding energy $E_{\text{binding}} = 34$ meV[104, 106] exceeding the room temperature thermal energy $k_{\text{B}}T = 26$ meV. The existence of trions is less clear in the PL spectrum of our monolayer MoSe₂, only slightly discernible as PL tailing when plotted on a semi-log scale as shown in Fig. 4-2(c) or the dashed blue trace in Fig. 4-4(a). The low-energy tail extending to the near infrared may arise from other bound excitonic states overlapped by thermal broadening effects. Being real transition levels, this continuum of bound excitonic states causes a large $\chi^{(2)}$ value of ~ 40 pm/V far below the optical gap, when it is two-photon resonant with the fundamental photon energy. While such a behavior also seem to exist in MoS₂ as shown in Fig. 4-4(b), it is interesting that the effect is much more pronounced in MoSe₂. While this effect is desirable for NLO applications in the infrared, our results also show that the SHG technique can be utilized to efficiently probe trions and bound excitons in TMDCs.

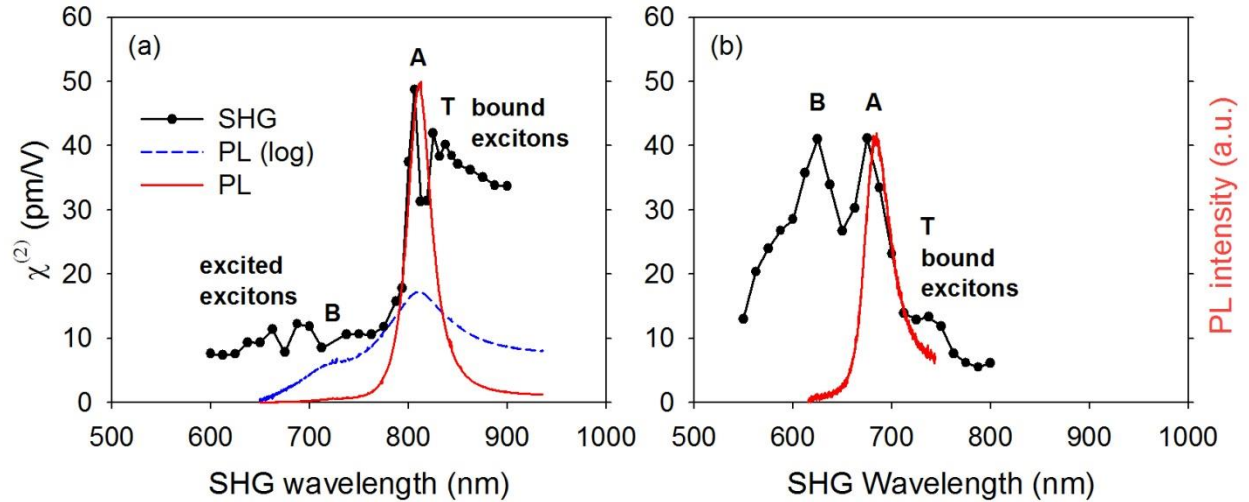


Figure 4-4 (a) Broadband $\chi(2)$ dispersion of the MoSe₂ monolayer and (b) MoS₂ monolayer with superimposed PL spectra (solid red traces). The major excitonic levels are indicated.

For high-power NLO applications, applicable materials should possess a sufficiently high optical damage threshold. Therefore, the laser-induced damage threshold (LDIT) of monolayer MoSe₂ was evaluated to consider the feasibility of utilizing this novel material as a high-power laser component such as a frequency converter or a saturable absorber. In fact, saturable absorption was recently demonstrated using MoS₂ suspensions.[107, 108]

The LIDT measurement was performed by recording the spectrally integrated SHG counts as a function of laser intensity at the fundamental Nd:YAG line (1064nm), which is a typical wavelength for picosecond NLO applications. These peak laser intensities are the time-averaged values over 2000 cycles. Since the fundamental photon energy is ~ 1.2 eV, the simultaneous absorption of two photons is necessary for the real excitation across the bandgap ($E_g \sim 1.53$ eV). While SHG is a virtual two-photon process yielding a frequency-doubled photon in the final state by leaving an NLO medium in the ground state, it is important to note that two-photon absorption (2PA) involves simultaneous absorption of two photons to promote an electron from a valence band to a conduction band, i.e., non-parametric.[109] Therefore, two-photon absorption (2PA) is expected to be the dominant mechanism for optical breakdown when significant.

The damage mechanism under picosecond-pulse excitation is attributed to electron avalanche breakdown [110-112] where electrons are initially populated into the conduction band via optical excitation. The relaxation of electrons involves a transfer of energy to

phonons until enough electrons have been generated to damage the crystal through resistive Joule heating. A crystal's bandgap strongly governs the LIDT particularly in the case of the excitation photon energy being tuned below the bandgap as in this study. Since the population of initial electrons and further excitation of these charges is a result of 2PA, the LIDT should exhibit some dispersion as well as a dependence on the excitation pulse duration. The LIDT is also dependent on the overall band structure which dictates the strength of the electron-phonon coupling and governs the energy transfer rate between conduction-band electrons and phonons.

Figure 4-5 plots the intensity-dependent SHG response for MoSe₂ (circles) and MoS₂, (dots), respectively, when the input irradiance was varied from 3 – 60 GW/cm². We found that SHG is more efficient in MoSe₂ than MoS₂ at $\lambda = 1064$ nm. In the low-intensity regime where 2PA is minimal, square-law fitting, $I_{SHG} = \alpha I^2$ can be used to explain the dependence of SHG intensity I_{SHG} on the laser intensity I as shown by the solid red solid line of Fig. 4-5. In this case, α is an overall scaling factor that includes $|\chi^{(2)}|^2$. Such dependence is no longer maintained when the peak input intensity is larger than ~ 16 GW/cm² for our MoSe₂ monolayer and the sample damage could be readily observed by imaging the flake onto the CMOS camera. The LIDT of a CVD-grown MoS₂ monolayer was also assessed and was measured to be ~ 24 GW/cm². This higher LIDT is expected since MoS₂ is a wider bandgap material and thus more resilient to optical damage. Most of all, it is noteworthy that in both cases the monolayer shows almost 10 \times stronger LIDT than benchmark NLO crystals such as AgGaSe₂ ($E_g \sim 1.8$ eV) and AgGaS₂ ($E_g \sim 2.4$ eV) under the same experimental condition.[113] In fact, these LIDT values of the TMDC monolayers are truly impressive when considering their lower bandgaps. These exceptionally high LIDTs seem to originate from good thermal conductivity[114] of TMDC monolayers together with inefficient 2PA in an atomically thin interaction length; 2PA is basically volume excitation.

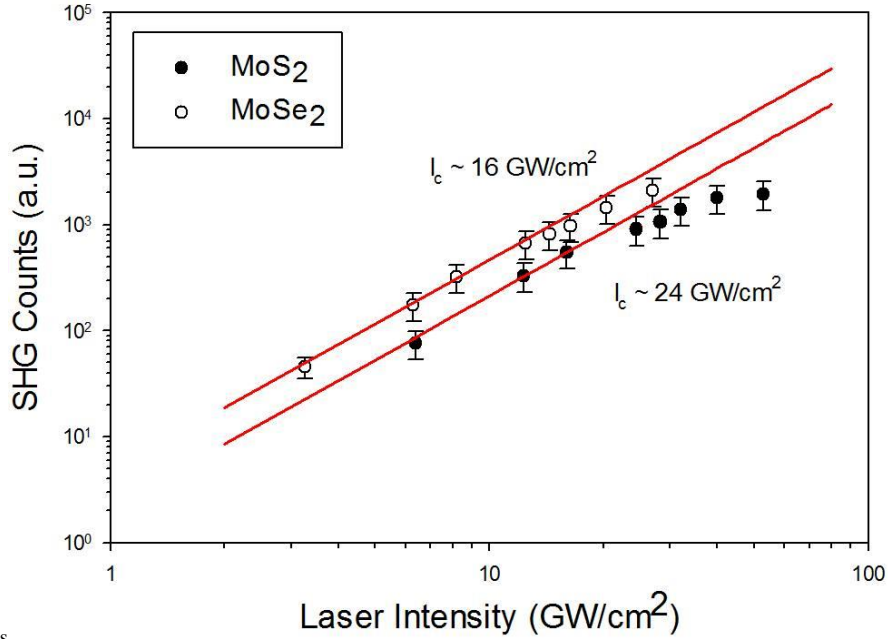


Figure 4-5: SHG power dependence of MoSe₂ monolayer (white dots) and MoS₂ monolayer (black dots) plotted on a log-log scale. The solid red lines are square-law fitting lines.

4.4 Chapter summary

We have reported the NLO characteristics of monolayer MoSe₂ both as a function of input intensity as well as wavelength over the key optical transition range. From basic optical measurements, Raman fingerprints and PL, we have confirmed that our monolayer MoSe₂ flake exhibits a high crystal quality. We have estimated the $\chi^{(2)}$ dispersion in a broad range of spectral wavelengths. Furthermore, we have also observed strong two-photon resonant enhancement in $\chi^{(2)}$ especially at the *A*-exciton state and bound exciton states in the crystal. We have also demonstrated that the SHG scan efficiently probes bound excitons and trions. Finally, the strong LIDT was measured in comparison with monolayer MoS₂, showing strong potential for high-power NLO applications. We believe that our findings will pave the way to a new era of 2D NLO devices with large $\chi^{(2)}$ over a wide spectral range from the visible to near-infrared when sufficient knowledge and control are available to stack these layered 2D materials to form especially 2D heterostructures.

Chapter 5: Impact of selenium doping on resonant second harmonic generation in monolayer MoS₂

5.1 Introduction

5.1.1 Overview

Second harmonic generation (SHG), an optical frequency doubling process, is historically a bulk process where nonlinear light-matter interaction coherently builds up with increasing interaction volume in a noncentrosymmetric crystal. In addition, SHG is a powerfully versatile and nondestructive technique that has been widely used to investigate the surface and interface of biological specimens where the inversion symmetry is inherently broken.[115, 116] The subject of SHG studies has also become important in atomically thin layered materials that provide an ideal two-dimensional (2D) world for exploring new physics. Especially, the advent of monolayer transition metal dichalcogenides (TMDCs), MX₂ (M = Mo, W; X = S, Se, Te), has drawn significant interest from various perspectives, especially optoelectronics as these semiconductors exhibit properties distinct from their bulk counterparts.[117] An indirect-to-direct bandgap[118] transition occurs for monolayer TMDCs, yielding strong luminescence in the visible or near-infrared (IR) range.[20] Moreover, inversion symmetry ceases to exist in the hexagonal TMDC lattice as a consequence of being a monolayer, rendering them to be SHG-active. Many theoretical and experimental investigations on single- and odd-layered TMDCs have reported strong second-order nonlinear susceptibility, $\chi^{(2)}$, especially at the exciton resonances for monolayer MoS₂,[119] MoSe₂,[120] WS₂,[121] and WSe₂. [122, 123] Additionally, TMDCs possess high laser-induced damage thresholds making them great candidates for high-powered nonlinear optical (NLO) devices.[120, 124]

5.1.2 Motivation

Two critical issues that must be considered for NLO applications are *i*) the magnitude of the optical nonlinearity and *ii*) the spectral range of the material for efficient SHG. Therefore, enhancing $\chi^{(2)}$ over a broad spectral range is significantly beneficial for developing realistic 2D NLO devices. To address the former issue, several studies reported

the enhancement of SHG by applying external stimuli under different mechanisms. Yu *et al.*[45] employed a back-gate electric field to induce nonzero SHG in “centrosymmetric” bilayer WSe₂ under a charge accumulation state. On the other hand, SHG could be efficiently implemented by manipulating neutral and charged excitons through a resonance effect. Very recently, Seyler *et al.*[125] demonstrated electrically enhanced SHG around the spectral position of the *A*-exciton in monolayer WSe₂ up to a factor of four at room temperature and a factor of ten at low temperatures. This work was fundamentally based on the electrostatic doping controlled exciton. In contrast, the latter issue has not been actively pursued, although the performance range of SHG could potentially be tuned by spectrally shifting exciton energies through controlled alloying. Recent progress in 2D growth allows the synthesis of completely tunable monolayer ternary alloys MoS_{2(1-x)}Se_{2x} and Mo_{1-x}W_xSe₂. [126-128] However, to the best of our knowledge, the alloying effects on TMDC crystallinity in terms of highly efficient SHG remain almost unexplored, thus prompting us to study the second-order NLO properties of TMDC alloys and gain physical insight for NLO applications.

In this chapter, we synthesized high-quality monolayer ternary alloys MoS_{2(1-x)}Se_{2x} ($0 \leq x \leq 0.62$) using the chemical vapor deposition (CVD) approach in an effort to spectrally tune resonant SHG over a wide range of wavelengths. The chemical composition of alloy samples was analyzed by X-ray photoemission spectroscopy (XPS). Since the chemical composition of a single specimen can slightly vary from flakes to flakes, the actual *x* values for monolayer flakes under investigation were estimated by the spectral position of the *A*-exciton of monolayer alloys. Furthermore, the structural and linear optical properties were respectively characterized by Raman scattering and photoluminescence (PL) spectroscopy. Due to their atomic-scale thickness, X-ray diffraction cannot efficiently probe the crystalline properties of the monolayers. Therefore, the monolayer ternary alloys were subjected to polarization-dependent SHG, confirming the underlying *D*_{3h} structure. We calculated the $\chi^{(2)}$ dispersion for monolayer alloys with varying Se composition to observe the effect of Se doping on the SHG characteristics by employing wavelength-dependent SHG scan. The main results were also compared with those obtained from a pure MoSe₂ monolayer prepared by pulsed laser deposition (PLD) assisted CVD to understand the overall behavior over a wide doping range including the two end members. We experimentally demonstrate that Se alloying not only enhances $\chi^{(2)}$ but also broadens the excitonic resonance

range significantly. Our approach provides a novel concept for engineering highly efficient 2D materials for NLO applications.

5.2 Result and discussion

Ternary alloys $\text{MoS}_{2(1-x)}\text{Se}_{2x}$ ($0 \leq x \leq 0.62$) were grown onto SiO_2 (300 nm)/Si substrates by atmospheric pressure CVD, which employed MoO_3 powder and a mixture of chalcogen powder S/Se as reactants. By varying the Se and S molar ratio, we were able to grow controlled compositions of ternary alloys.

5.2.1 The growth of monolayer $\text{MoS}_{2(1-x)}\text{Se}_{2x}$ alloys:

The growth was performed in a sealed vacuum quartz chamber under ambient pressure. ~2 mg of high-purity MoO_3 (Sigma Aldrich, 99.99%) powder in a graphite crucible was placed at the entrance of the tube in the high-temperature zone. Meanwhile, a specified amount of mixed sulfur/selenium powder (Sigma Aldrich, 99.99%) was put in another graphite crucible placed at the exit of the quartz tube and varied to yield the desired Se concentration in the grown monolayer. The SiO_2/Si substrate was securely laid face down onto a designated quartz plate. The temperature of the MoO_3 -containing zone was risen to 400°C and kept constant for 5 min, while the corresponding temperature of the mixed chalcogen powder was 130°C. Next, the high-temperature zone was heated up to the reaction temperature ~950°C, while the chalcogen-powder-contained zone was kept at a lower temperature of ~450°C. During heating, a mixture of high-purity 10 sccm Ar and 2 sccm H_2 gas were introduced to the chamber as a carrier gas.

Initially, the surface morphology of as-grown alloys was characterized using standard spectroscopic imaging tools for 2D materials i.e. an optical microscope (OM, Nikon system) and an atomic force microscope (AFM, MFP-3D). Under the optical microscope, the domains with an average size of ~50 μm were clearly seen with a homogenous color together with flakes having an equilateral triangular shape toward the edge of the substrates, Fig. 5-1(a). Merged domains and star-like domains formed at the central part of the sample are commonly observed for CVD-grown TMDCs. For our study, an isolated single domain flake was selected from each sample (See Fig. 5-2) and the corresponding AFM height profile was

measured to confirm the monolayer thickness, which is required to accurately assess $\chi^{(2)}$ of the monolayer. This single domain is also confirmed by polarization-dependent SHG study. We found that the thickness of the selected flakes is in the range of $\sim 0.8 - 1.0$ nm. For example, Fig. 5-1(b) displays a typical AFM image of a single flake of $\text{MoS}_{2(0.55)}\text{Se}_{2(0.45)}$. The overlaid height profile (blue trace) indicates that the thickness of the as-grown flake is ~ 0.83 nm which closely matches the thickness of a monolayer alloy in a previous report.[126]

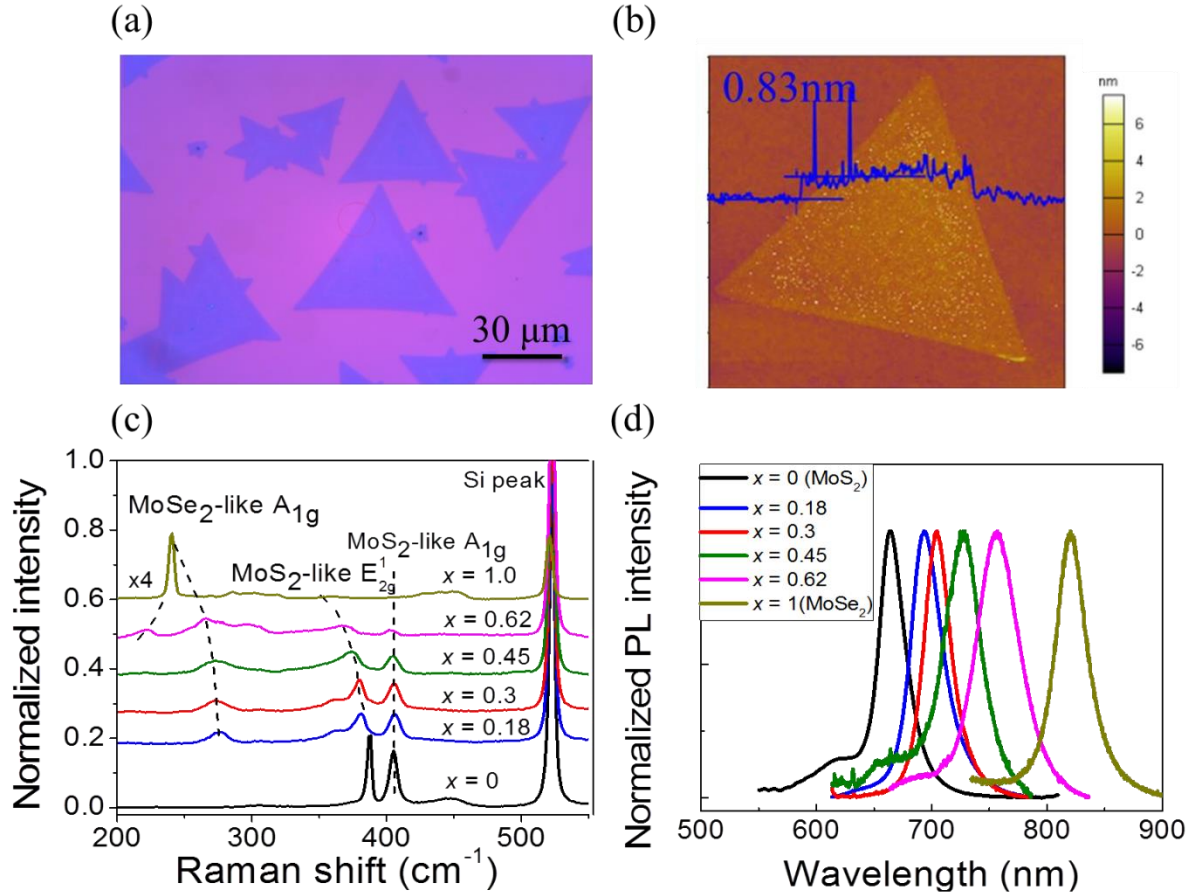


Figure 5-1: (a) Optical microscopic image (scale bar is $30 \mu\text{m}$) and (b) representative AFM image ($x = 0.45$). Normalized (c) Raman spectra and (d) PL spectra for monolayer alloys as a function of Se composition, x . For comparison, the data for PLD-assisted grown MoSe_2 is plotted together (dark yellow curve).

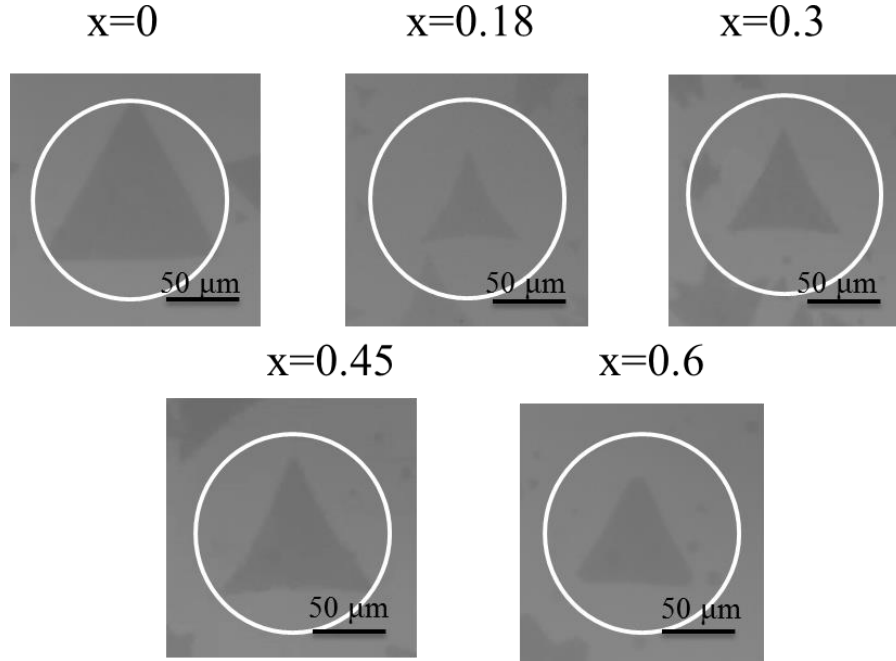


Figure 5-2: CMOS images of alloy flakes selected for the SHG study. The beam size is $\sim 100 \mu\text{m}$ in diameter as indicated by the circle.

The phonon modes of our as-grown alloy monolayers were characterized by analyzing the Raman spectra at room temperature. A continuous wave 514.5 nm Ar^+ beam (Melles Griot, 35-LAP-431-220) was utilized as the excitation source with a beam power of ~ 0.1 mW and tightly focused down to a spot size of $\sim 1 \mu\text{m}$ in diameter. Fig. 5-1(c) shows composition-dependent normalized Raman spectra of as-grown monolayer $\text{MoS}_{2(1-x)}\text{Se}_{2x}$. For comparison, the Raman spectrum from the monolayer MoSe_2 is plotted together.⁷ All Raman active modes of pure MoS_2 and pure MoSe_2 are clearly observed. There are two Raman peaks associated with Mo-S coordination: the in-plane A_{1g} mode (404.7 cm^{-1}) and the out-of-plane E_{2g}^1 mode (387.4 cm^{-1}) in the higher frequency range. Similarly, there are two noticeable peaks associated with Mo-Se coordination: one for the in-plane A_{1g} mode (240.6 cm^{-1}) and one out-of-plane E_{2g}^1 mode (285.5 cm^{-1}) in the lower frequency range. In addition, we also observed peak splitting of the MoS_2 -like E_{2g}^1 mode when x is in the range of 0.18–0.45 and splitting of the MoSe_2 -like A_{1g} mode at $x = 0.62$. This splitting stems from the difference in structural arrangement of S/Se atoms relative to Mo atoms.[129] The contrasting evolution of peak intensities was found in between MoS_2 -like and MoSe_2 -like

vibrational modes as Se composition changes. This is consistent with previous studies on monolayer $\text{MoS}_2(1-x)\text{Se}_{2x}$. [126, 127] More specifically, the MoS_2 -like A_{1g} and E_{2g}^1 modes appear strongly at lower Se compositions, but they are more suppressed and eventually vanish from the Raman spectra upon increasing Se composition. Meanwhile, the MoSe_2 -like A_{1g} and E_{2g}^1 modes are initially missing and then progressively become more pronounced.

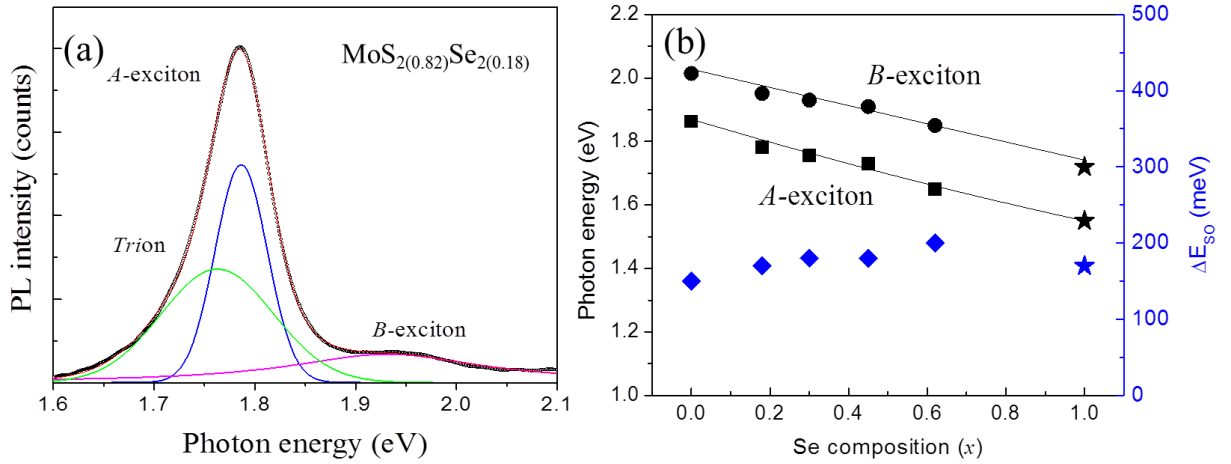


Figure 5-3 (a) PL (circles) of monolayer alloy $\text{MoS}_2(0.82)\text{Se}_2(0.18)$ with Gaussian fit curves to the A-exciton (blue traces), B-exciton (magenta trace), and trion (green trace) to produce the overall fit (brown trace). (b) A-exciton (squares) and B-exciton (circles) spectral position as a function of x . Also plotted is the energy separation (spin-orbit splitting) between the two exciton states (blue diamonds). Star dots are data from our previous publication regarding the PLD-assisted grown monolayer MoSe_2

Room-temperature PL was measured to determine the spectral positions of excitons in the as-grown monolayers. Fig. 5-1(d) shows normalized PL spectra as a function of x (see SI for the determination of x), together with the result from the MoSe_2 monolayer ($x = 1$) to discern the tunability of excitonic states. All PL spectra show a prominent peak with a higher energy shoulder, which can be assigned to A- and B-exciton band-edge transitions, respectively, where the associated energy splitting arises from the large spin-orbit splitting of the valence band maximum at the K (K') point. The Gaussian fits were carefully performed to precisely deduce the A- and B-excitonic levels as shown in Fig. 5-3(a). As Se composition increases, we observed a variation in the optical bandgap of the alloys from 1.87 eV to 1.53 eV as evidenced by red-shift in the PL spectral peak position from 660 nm (pure MoS_2) to

810 nm (pure MoSe₂). When x varies from 0 to 1, the B -exciton also red-shifts in the range of ~ 2.0 eV – 1.72 eV as shown in Fig. 5-3(b). Furthermore, spin-orbit splitting, ΔE_{SO} , calculated from the PL data is in the range of 150 meV – 200 meV and agrees well with theoretical results.[130] Additionally, the trion (negatively charged exciton) level can be also seen in the long-wavelength tail as evidenced from the fit in Fig. 5-3(a). Since our experiment was performed at room temperature, bound exciton states may be overlapped due to thermal broadening effects in the near-IR range. We also found that the PL intensity significantly reduces and the exciton peaks broaden when Se composition increases (Fig. 5-4), which is consistent with observation in the literature.[131] While such a behavior is typical in alloys and sometimes interpreted as a negative effect of alloying, our major result indicates that bandgap engineering of MoS₂ by Se substitution is indeed beneficial in terms of stronger and broader NLO response as discussed below.

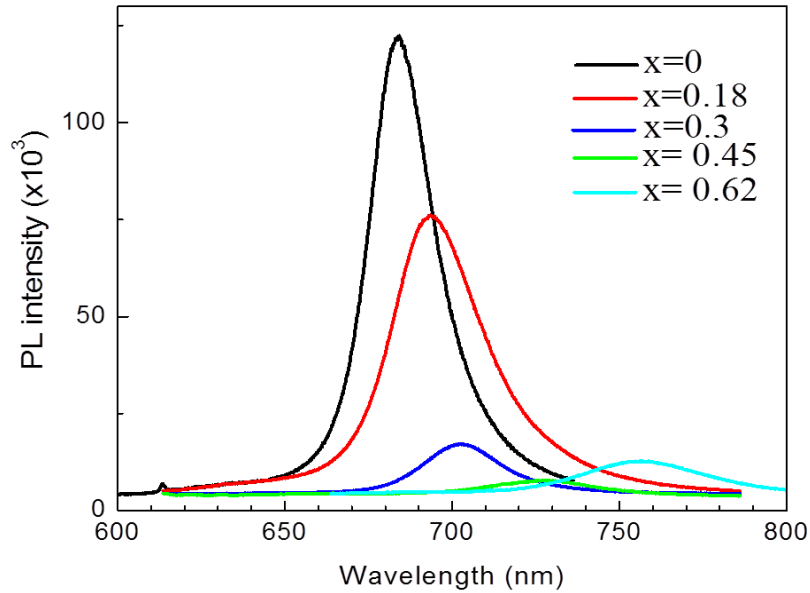


Figure 5-4 Room-temperature PL spectra of monolayer ternary alloys

In order to determine the crystal symmetry and orientation of monolayer ternary alloys, we carried out a polarization-dependent SHG measurement, which is schematically illustrated in Fig. 5-5(a). A typical monolayer flake for polarization-dependent SHG is shown in Fig. 5-5(b), which was imaged by the CMOS camera. For MoS₂ and MoSe₂, their bulk and even-layered slabs belong to the D_{6h} symmetry, which possesses inversion symmetry, signifying $\chi^{(2)} = 0$ and hence no SHG. In contrast, odd-layered TMDCs possess D_{3h}

symmetry, which lacks inversion symmetry, yielding a strong SHG signal. For monolayer alloys, phase separation, such as local MoS₂ and MoSe₂, is absent in the formation of monolayer ternary MoS_{2(1-x)}Se_{2x} due to small lattice mismatch.[132] Accordingly, the single/double Se substitution could randomly occur at different S sites in the hexagonal lattice of MoS₂, which was experimentally observed and analyzed in detail using atomic resolution annual dark field imaging.[131] This arbitrary substitution of S by Se in the primitive unit cell can result in an additional SHG field which is absent in pure MoX₂. As global symmetry is no longer precisely D_{3h} , other components, d_{15} , d_{31} , and d_{33} , emerge with Se substitution. However, our density functional theory (DFT) calculations confirmed that those components are much smaller than $d_{22} \equiv \chi_{xxx}^{(2)}/2$ at most by 4 – 6% for $x = 0.5$. Monolayer alloys thus approximately assume D_{3h} crystal symmetry. As a result, we expect that the monolayer ternary alloys should exhibit the same polarization-dependent SHG response as MoS₂ and MoSe₂, whose second-order susceptibility tensor can be expressed by one independent element, $\chi_{xxx}^{(2)} = -\chi_{xyy}^{(2)} = -\chi_{yyx}^{(2)} = -\chi_{yxy}^{(2)}$. Accordingly, the resultant SHG with polarization states being parallel and perpendicular to the fundamental beam should respectively be proportional to $\cos^2[3(\theta + \theta_0)]$ and $\sin^2[3(\theta + \theta_0)]$, where θ denotes the angle between the incident linear polarization and the mirror axis of the crystal and θ_0 denotes the initial angular offset. Fig. 5-5(c) shows the normalized polarization-dependent SHG intensity as a function of θ for parallel (blue squares) and perpendicular (red dots) configurations in monolayer MoS_{2(0.82)}Se_{2(0.18)} at the fundamental wavelength of 1360 nm. The solid red and blue traces are the fit curves to both polarization states using a least-squares method. We observed one oscillation peak in the SHG intensity when each sample was rotated through 60° in 10° steps, indicating the six-fold symmetry through one full azimuthal rotation. Likewise, all monolayer alloys with different x values display a similar six-fold pattern for polarization-dependent SHG (see details in Fig. 5-6). The sharp six-fold pattern in the polarization-dependent SHG measurement along with PL spectra suggests that the as-grown alloys possess high structural and optical quality.

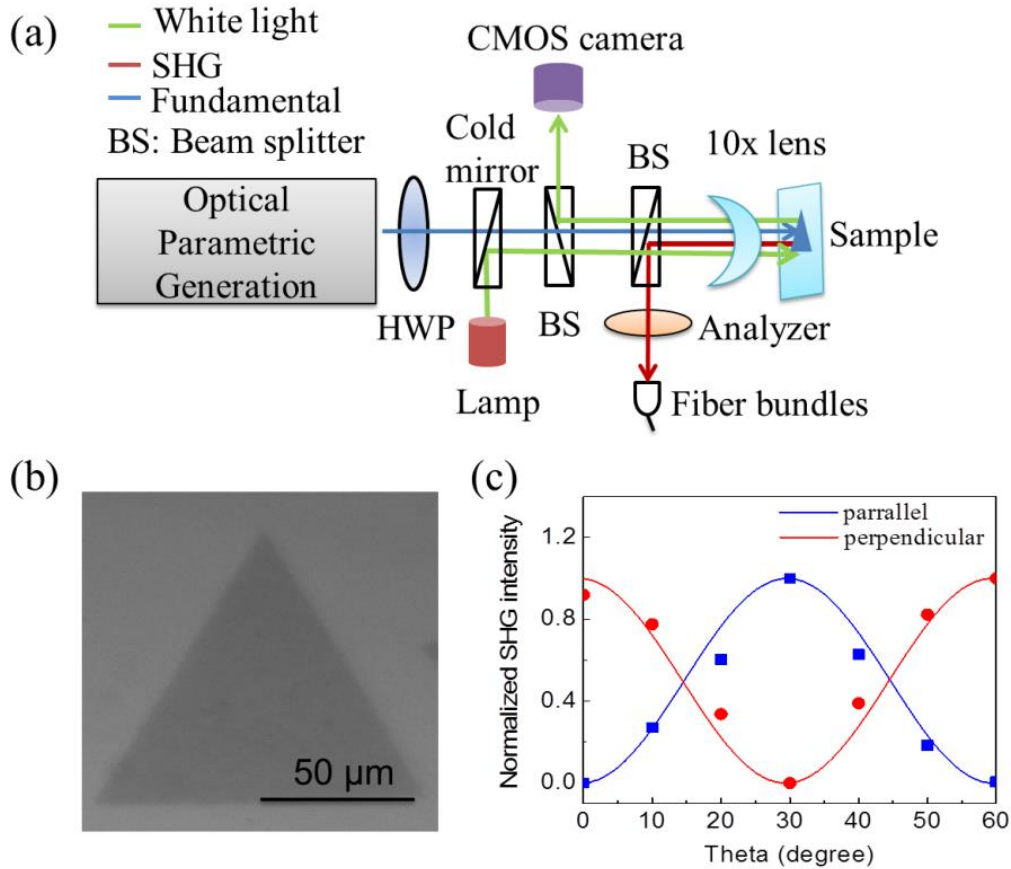


Figure 5-5: (a) SHG experimental setup, (b) CMOS images of a targeted sample, and (c) polarization-dependent SHG through 60° rotation of monolayer MoS_{2(1-x)}Se_{2x} ($x=0.18$). Scattered symbols are experimental data and solid traces are corresponding fitting curves.

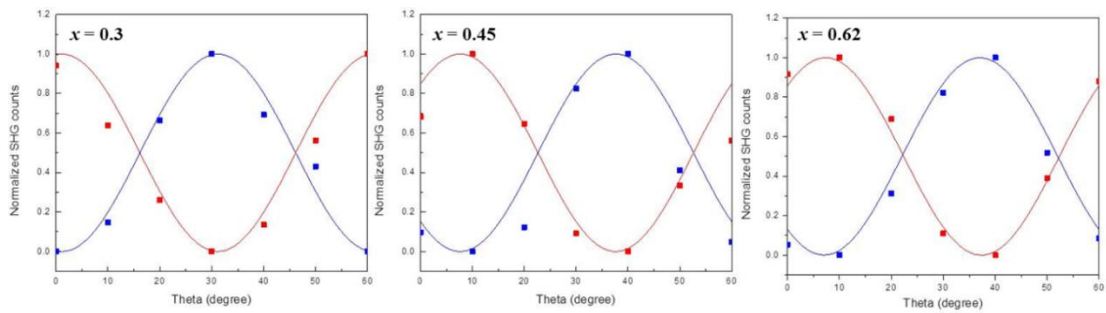


Figure 5-6: Polarization-dependent SHG through a 60° rotation of MoS_{2(1-x)}Se_{2x} ($x = 0.3, 0.45, 0.62$) monolayers. The input wavelength was chosen where the SHG response is maximum. Scattered blue and red dots are experimental data for SHG which were parallel and perpendicular to the input polarization state of the fundamental beam, respectively. Solid traces are corresponding fitting curves.

The SHG response was measured as a function of wavelength to calculate the $\chi^{(2)}$ dispersion in these monolayer alloys. A bulk *z*-cut quartz single crystal was utilized as a reference material for the calibration of the SHG efficiency. In order to probe optical transitions near the band edge and exciton resonance effects, we varied the wavelength from $\lambda = 1000 \text{ nm} - 1800 \text{ nm}$ in sufficiently fine steps of $\Delta\lambda = 20 \text{ nm}$. In an effort to account for any discrepancy in the monolayer flake sizes spanning from $\sim 50 \text{ }\mu\text{m}$ to $100 \text{ }\mu\text{m}$, the SHG intensities were properly scaled and normalized to a single monolayer domain size of $100 \text{ }\mu\text{m}$ (Fig. 5-2). Resonantly enhanced SHG at the excitonic levels can be clearly seen by overlapping the PL spectra and wavelength-dependent SHG of monolayer $\text{MoS}_2(1-x)\text{Se}_{2x}$ ($0 \leq x \leq 0.62$) as depicted in Fig. 5-3. We observed a general trend in the broadband SHG spectra for all monolayer alloys including pure MoS_2 and MoSe_2 which can be described as follows.

At shorter wavelengths ($< 600 \text{ nm}$) where the two-photon virtual energy level of the SHG process is above the excitonic transitions, SHG intensities are relatively unchanged, indicating no resonance effects; our monitoring range is below the *C*-exciton level. Meanwhile, for wavelengths near *A*- and *B*-excitonic levels, SHG intensities are strongly enhanced for all of our bandgap-engineered monolayers. This enhancement in SHG is attributed to exciton resonance effects where the tunable virtual state of the SHG process lies energetically close to the real energy level of the excitons. As previously demonstrated,[133], fine-scale SHG scan typically yields a precise information on the resonance level even for the optically inactive transition. This effect is consistently observed for binary TMDCs in previous publications.[134] When Se composition increases, the resonantly enhanced SHG peaks at the *A* and *B*-exciton states red-shift and spectrally match well to the corresponding PL peaks. Interestingly, the resonance effect is more significant near the *B*-exciton level than the *A*-exciton level for monolayer alloys, whereas the *B*-exciton resonance seems to be much suppressed for pure MoS_2 (black curve) and MoSe_2 (orange curve). As clearly shown in Fig. 5-7, this phenomenon becomes more pronounced with higher Se compositions. For low Se compositions ($x = 0.18, 0.3$), SHG near the *B*-exciton becomes stronger and even comparable to that near the *A*-exciton. As the Se concentration increases further, the SHG intensity near the *B*-exciton is more significant than that near the *A*-exciton. For example, at $x = 0.62$, the SHG intensity at the *B*-exciton is two times stronger than that close to the *A*-exciton. We

believe that this could be an extrinsic effect associated with defects and/or state broadening, which resulted from the fluctuation of surrounding electrostatic potential caused by the random distribution of Se atoms. This random substitution could lead to local electronic structure change as clearly seen in scanning tunneling microscopy/spectroscopy studies for $\text{Mo}_{1-x}\text{W}_x\text{S}_2$. [135] In fact, the state broadening is clearly seen through the increase in the full width at half maximum of the PL spectra (see Table 2). It is also demonstrated that SHG efficiency could be slightly enhanced by chemically introducing the dopants in the lattice of monolayer TMDCs, such as MoSe_2 . [136] The doping effect on SHG is expected to be most obvious at $\text{MoS}_{2(1-x)}\text{Se}_{2x}$ ($x = 0.5$), where the local density of states significantly changes. [137] This is also consistent with the widest exciton resonance at $x = 0.45$ from Table 2 and Fig. 5-7. However, our hypothesis needs more detailed theoretical calculations as well as additional measurements for a rigorous explanation.

Table 2: Full width and half maximum of *A*- and *B*-exciton calculated from PL for different Se composition.

Se composition (x)	A-exciton (meV)	B-exciton (meV)
0	52	93
0.18	71	110
0.3	68	109
0.45	70	180
0.62	74	110

More importantly, Fig. 5-3 shows that monolayer alloys exhibit much wider resonance through broadening of the *A* and *B*-exciton states without hampering the maximum SHG response. Therefore, we clearly demonstrate that state broadening by alloying is beneficial for stretching the efficient performance range of SHG. The impact of trions on SHG resonance in monolayer alloys is less clear, although it may contribute to the

broadening of the resonance near the A -exciton towards the longer wavelength range, which is most evident for the $x = 1$ case. We also note that B -exciton resonance may have two peaks as most well demonstrated by the $x = 0.18$ case. This could be due to an alloying-induced splitting of the conduction band at the minimum in which electron-hole exchange interaction further splits the four-fold degenerate B excitons into the singlet and triplet states. In fact, this effect is theoretically predicted to be stronger for the B -exciton state, especially for Se-containing Mo-based TMDCs.[138]

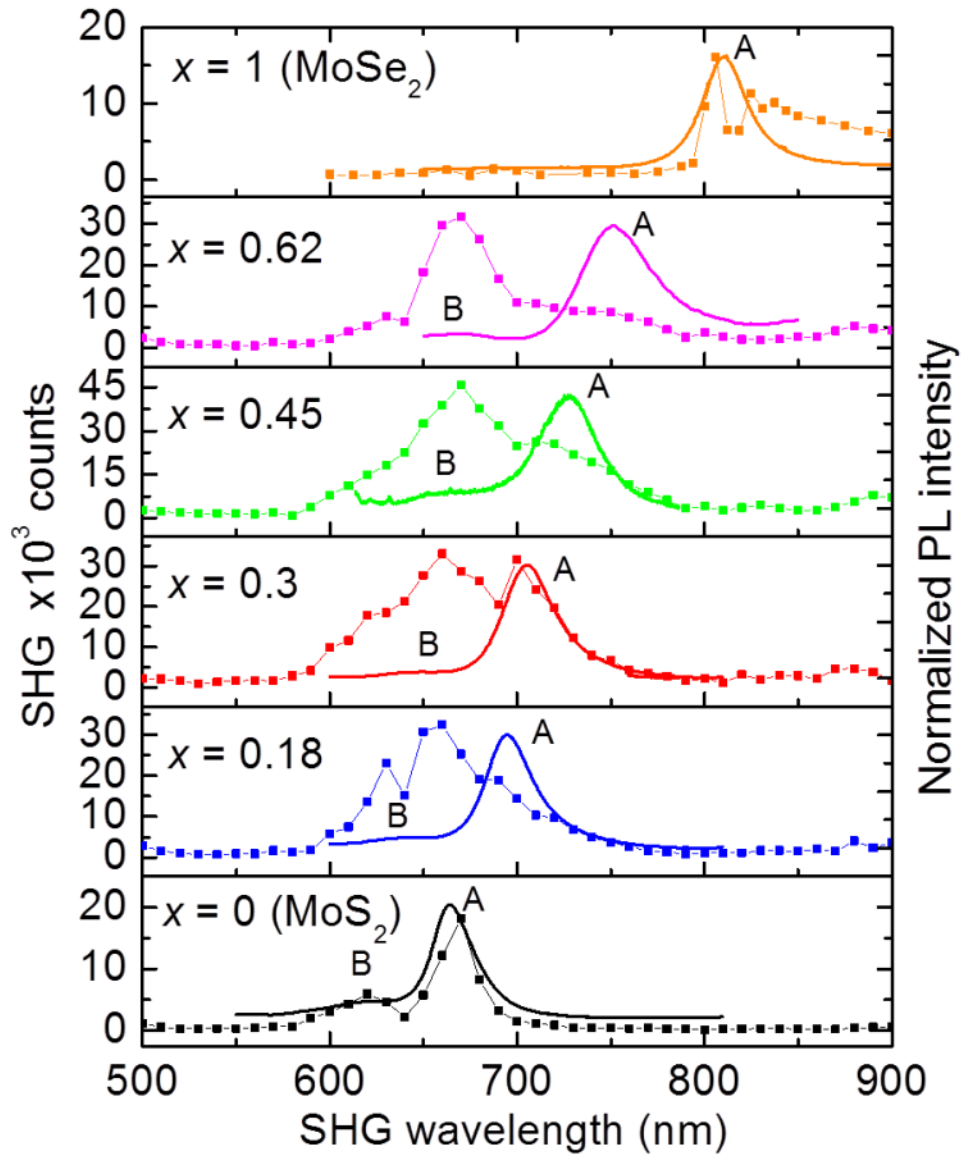


Figure 5-7: SHG spectra (dotted traces) of monolayer alloys and corresponding room-temperature PL spectra (solid traces). Spectral positions of the *A*- and *B*-excitons are indicated. For comparison, SHG of PLD-assisted grown MoSe₂ is plotted together.

In order to calculate the absolute $\chi^{(2)}$ dispersion, we used our previously reported equation [134] that effectively considers monolayer TMDCs as “polarized dipole sheets” using the experimental SHG intensities as input values. The equation can be given as follows:

$$\chi_{\text{alloy}}^{(2)} = \frac{\chi_q^{(2)} [n_q(\omega) + 1]^3}{16\pi\Delta h\Delta k_q n_q(\omega) n_q^{1/2}(2\omega)} \left(\frac{\lambda}{\lambda_q}\right) \left(\frac{I_{\text{alloy}}(2\omega)}{I_q(2\omega)} F_q\right)^{1/2} \quad (1)$$

In Eq. (1), Δh represents the measured thickness of the monolayer from AFM; we used the averaged value ~ 0.8 nm. $\chi_q^{(2)} = 0.6$ pm/V is second-order susceptibility of quartz,[139] and $n_q(\omega)$ and $n_q(2\omega)$ denote the linear refractive indices of quartz at frequency ω and 2ω , respectively. Δk_q is the wavelength-dependent phase-mismatch term in quartz calculated from the refractive indices. $I_{\text{alloy}}(2\omega)$ and $I_q(2\omega)$ are the measured SHG intensities from the monolayers and quartz, respectively. λ_q is the wavelength at which the constructive spectral Maker fringe occurs for the reference quartz, where $\sin^2(\Delta k_q L_q/2) = 1$ and the SHG intensity from quartz (I_q) is a maximum in the monitored spectral range. Since the thickness of the monolayer alloys is much smaller than the excitation wavelength ($\Delta h \ll \lambda$), phase-matching factors are not taken into account for the monolayers. F_q represents the Fresnel coefficient of quartz, which compensates for reflection/transmission losses.³⁰

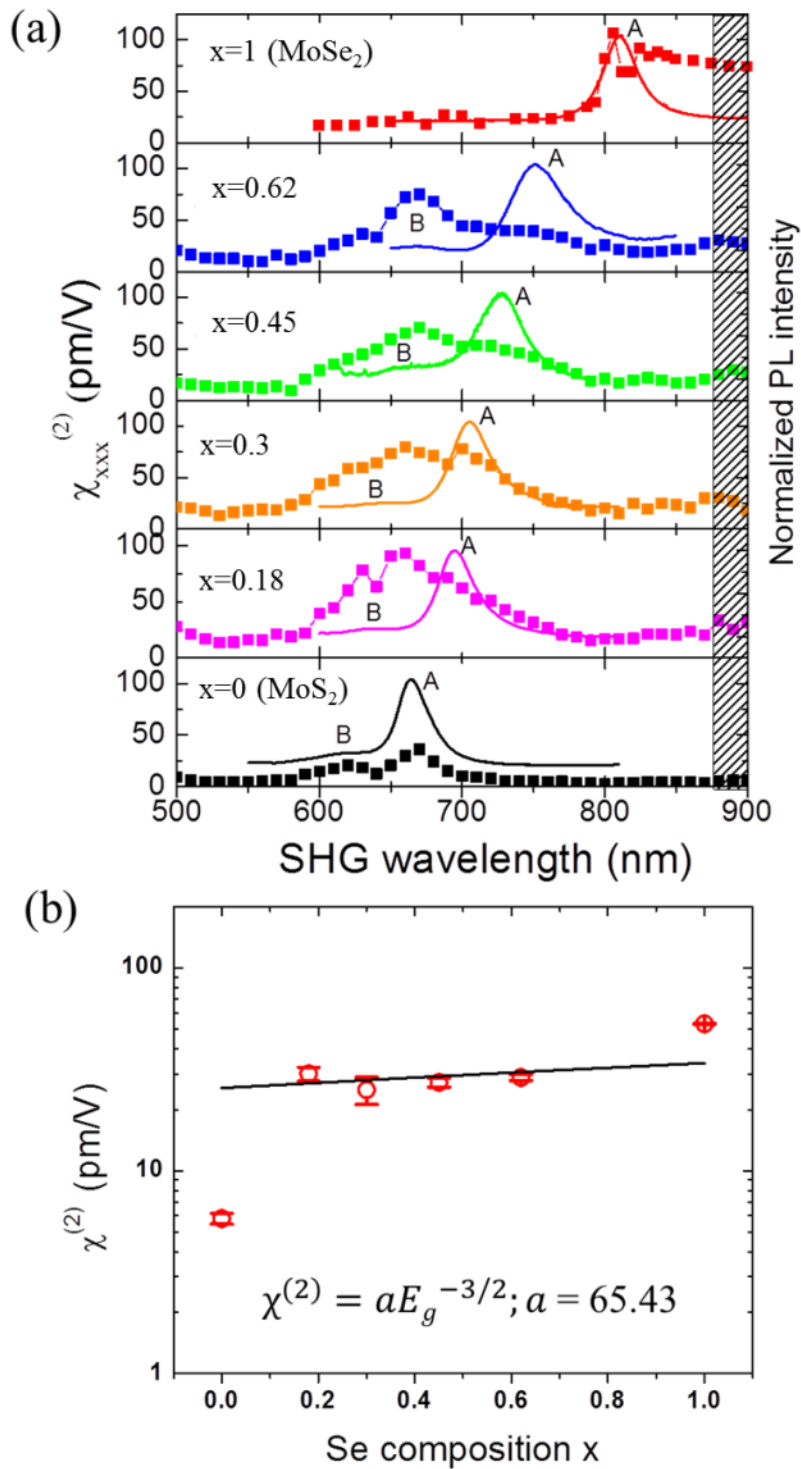


Figure 5-8: (a) $\chi_{xxx}^{(2)}$ dispersions of monolayer alloys with different Se compositions and (b) static $\chi^{(2)}$ values as function of Se composition. The solid line is a theoretical prediction.

Fig. 5-8(a) displays the calculated $\chi^{(2)}$ dispersions for monolayer alloy $\text{MoS}_{2(1-x)}\text{Se}_{2x}$ ($0 \leq x \leq 0.62$), in which we include the PLD assisted CVD-grown MoSe_2 result for comparison. A different flake size effect was taken into account as explained in SI. For all monolayer alloys, $\chi^{(2)}$ is a maximum in the SHG wavelength range of 660 – 680 nm. These $\chi^{(2)}$ peak values are between $\sim 40 - 80$ pm/V, which are consistent with the experimentally reported values for the pure MoS_2 and MoSe_2 . [119, 120] Fig. 5-8(b) shows composition-dependent $\chi^{(2)}$ values near the static range (the long-wavelength range away from excitonic transitions). These absolute values are calculated by averaging values over the SHG spectral range of $\lambda = 880 - 900$ nm [shaded area in Fig. 5-4(a)] and can be used to compare the zero-frequency $\chi^{(2)}$ response among the alloyed monolayers since they are far from resonance. The $\chi^{(2)}$ values at the static range increase with increasing Se composition which can be explained based on the decreased bandgap in monolayer alloys. This trend was indeed theoretically predicted in a previous study on monolayer TMDCs based on first principle calculations. [123] To semi-quantitatively assess the bandgap dependence on the static $\chi^{(2)}$, we plot a simple theoretical prediction, $\chi^{(2)} \sim E_g^{-3/2}$, in Fig. 5-4(b), which was firstly proposed by Jackson et al. [140] The model fits rather well with the experimental data within the investigated range. Clearly, the observed dependence confirmed that doping Se atoms into monolayer MoS_2 can enhance second-order NLO properties at the off-resonant range purely due to bandgap decrease.

For all SHG dispersions, we observed an enhancement in $\chi^{(2)}$ at exciton levels by a factor of ~ 3 compared to the static values. It is noteworthy that resonant $\chi^{(2)}$ values at the *B*-exciton for low Se compositions ($x = 0.18$ and 0.3) are two times greater than that of the *A*-exciton for pure MoS_2 (black curve). More interestingly, Fig. 5-4(a) illustrates that spectral broadening of the SHG resonance is evident in alloys, compared with that of monolayer MoS_2 or MoSe_2 . Our results therefore infer that more efficient SHG in terms of both magnitude and breadth can be obtained by Se alloying. Our results further implies that one can expect to obtain broader and even stronger resultant SHG by preparing a hetero-bilayer consisting of different Se contents, rather than merely $4\times$ stronger enhancement within a narrow range in the case of homo-bilayer MoS_2 as experimentally observed in a previous publication. [21] With recent advances in the vertical stacking technique, we believe that

higher efficiency frequency-conversion devices could be achieved by multi-layer heterostructure stacking, where the crystal orientation and the Se content of the constituent TMDC layers can be customized to controllably enhance SHG at specific wavelengths.

5.3 Chapter summary:

In conclusion, we have studied the impact of Se alloying in the benchmark TMDC monolayer of MoS₂ on SHG characteristics over a broad Se composition range up to $x = 0.62$. Raman scattering, photoluminescence and polarization-dependent SHG analysis show that our ternary alloys possess high crystalline and optical quality. Furthermore, we calculated the $\chi^{(2)}$ dispersions for the monolayer alloys using a polarized sheet model in which the monolayer thickness is much smaller than the excitation wavelength. We have clearly shown that resonant SHG of monolayer MoS₂ can be spectrally tuned by alloying. Most importantly, we demonstrated that alloying MoS₂ with Se further enhances and broadens the overall SHG efficiency. Further theoretical and experimental studies with a finer SHG scan step are required to elucidate a key correlation between alloying ratio and exciton resonance, especially at the *B*-exciton. Nonetheless, as a preliminary result, our findings imply potential to engineer monolayer alloys through oriented vertical stacking to fabricate NLO materials working over a broad spectral range with a high frequency-conversion efficiency. This combination could potentially spark generation of new and exciting ultrathin NLO devices.

Chapter 6: Preliminary results of broadband resonant second harmonic generation of artificially stacked heterostructures

6.1 Introduction:

6.1.1 Overview

Group-VI transitional metal dichalcogenides (TMDCs, MX_2 ; where $\text{M} = \text{Mo}, \text{W}$ and $\text{X} = \text{S}$ or Se) are hexagonally packed two-dimensional (2D) semiconductors with excellent optoelectronic properties. In the monolayer regime, MX_2 has a direct energy gap with broken inversion symmetry. Moreover, the band structure of monolayer MX_2 possesses doubly degenerate but inequivalent energy valleys (local band extrema) at K and K' in k -space, which is a direct consequence of broken inversion symmetry and restoration of time reversal symmetry. As a consequence, the TMDC system has hosted fascinating phenomena such as significant valley polarization,[141, 142] strong optical nonlinearity[143] with a high laser-induced damage threshold,[144] and exceptionally strong excitonic effects.[145, 146] These apparently distinct subjects of valleytronics, nonlinear optics, and excitonics are indeed closely interrelated in the monolayer TMDCs. For example, helicity-flipping “valley” selection rules for “nonlinear optical” second harmonic generation (SHG) and two-photon-induced “excitonic” luminescence were theoretically predicted and experimentally confirmed in monolayer TMDCs,[73, 147, 148], providing a better understanding of the combined effects offered by this unique material class.

6.1.2 Motivation

From the standpoint of nonlinear optics, however, a large bulk phase is generally preferred because the SHG field for instance increases with the interaction volume. Unfortunately, this is not the case in TMDCs since they stack in 2H order by alternating the orientation of each layer along the c -axis, rendering only layers with an odd number SHG-active.[61-63, 73, 149] This implies that artificial stacking of layers with the same orientation is required for maximizing SHG, in which the effect of stacking angle is clearly demonstrated for MoS_2 bilayers.[21] Controlled stacking of the same member of monolayer

MX_2 however only enhances the SHG intensity, which is strongest at the exciton resonance.[143] Recently, our group showed that engineering of valence-band splitting through alloying chalcogen anions with a controlled ratio of S/Se can significantly improve the SHG efficiency in terms of both strength and spectral breadth.[150] Our main thesis of this work is therefore towards boosting both working efficiency and range of SHG by the combination of both approaches (stacking and alloying) in artificially stacked heterostructures (HSs). Clearly, such a 2D scaffold with enhanced optical nonlinearity is highly desirable for realizing efficient second-order nonlinear optical devices.

To construct such a delicate artificial system, chemical vapor deposition (CVD) method has been conventionally used to yield large and high-quality monolayers MX_2 , [59, 151] alloys $\text{W}_x\text{Mo}_{(1-x)}\text{S}_{2(1-x)}\text{Se}_{2x}$ with a controlled x value, [57, 152] and also their vertical HSs. [153] However, the precise stacking of each layer without angle tilt in the HSs is critical for efficient SHG, which cannot be directly controlled by the CVD growth method. We used a micro-manipulator to build 2D vertical HSs by accurately aligning the orientation of different monolayers of varying chemical compositions in X. We investigated the SHG response of artificially stacked vertical HSs that include a homo-bilayer ($\text{MoS}_2/\text{MoS}_2$), a hetero-bilayer; $\text{MoS}_2/\text{MoS}_{2(1-x)}\text{Se}_{2x}$, and a hetero-trilayer; $\text{Mo}_{2x}\text{S}_{2(1-x)}\text{Se}_{2x}/\text{MoS}_2/\text{Mo}_{2x'}\text{S}_{2(1-x')}\text{Se}_{2x'}$. Morphological and optical inspections were initially carried out to examine the surface and optical quality of the HSs. The photoluminescence (PL) spectra showed a broad feature arising from both *A*- and *B*-excitonic transitions from each individual layer, indicating the excellent optical quality of the prepared samples. Wavelength-dependent SHG measurements were done using a picosecond pulsed laser ($\lambda = 1100 \text{ nm} - 1600 \text{ nm}$) to probe broadband SHG response. Intriguingly, we found that the SHG efficiency can be significantly enhanced to a desired wavelength range by controlling the Se concentration in the alloy layers within the HS system. Our findings imply the feasibility of artificial broadband nonlinear optical materials, which could be potentially important for compact optical communication in which wavelength multiplexing can be achieved by nonlinear optical wavelength conversion of the seed beam.

6.2 Result and discussion

High-quality CVD-grown monolayer flakes of MoS₂ and its alloys with an average size of ~50 μm were selected to fabricate the vertical HSs. The HSs were assembled using a PMMA (Poly-methyl methacrylate)-involved transferring process by using the micro-manipulator. Since the SHG intensity strongly depends on stacking orientation,[21, 143] the constituent layers in the HS systems were stacked in such a fashion that their corresponding armchair directions lied parallel to each other. The optical microscopic (OM) image of a typical hetero-bilayer used in our study is shown in Fig. 6-1(a). Fig. 6-1(b) shows the atomic force microscopic (AFM) topographic image of the vertical stack taken from the red square in Fig.6-1 (a). The thicknesses of monolayer and bilayer regions were found to be ~1.0 nm and 2.3 nm, respectively. The slightly larger thickness of the two-layer region can arise from absorbents on the substrate surface,^[28, 154] residue trapping during the transferring process, or even the measurement uncertainty.^[155] The HS sample was further examined by Raman and PL spectroscopy at room temperature using a cw laser ($\lambda = 473$ nm). The blue trace in Fig. 6-1(c) is the Raman spectrum from an isolated MoS₂ region, showing two dominant peaks at ~384.1 cm⁻¹ and ~402.8 cm⁻¹, which correspond to E_{2g}^1 (in-plane) and A_{2g} (out of plane) vibrational modes, respectively. The corresponding peak separation $\Delta\omega \sim 18$ cm⁻¹ further confirms that MoS₂ is indeed a monolayer, which is consistent with the AFM result. The red trace in Fig. 1(c) corresponds to the MoS₂-like E_{2g}^1 (~378.1 cm⁻¹) peak from the monolayer alloy MoS_{2(0.7)Se_{2(0.3)}} region undergoes slight red-shift with Se doping. This frequency shift is consistent with the previous result.[150] The Raman spectrum acquired from the HS region (black trace in Fig.6-1(c)) shows all active vibrational modes of individual constituting layers.

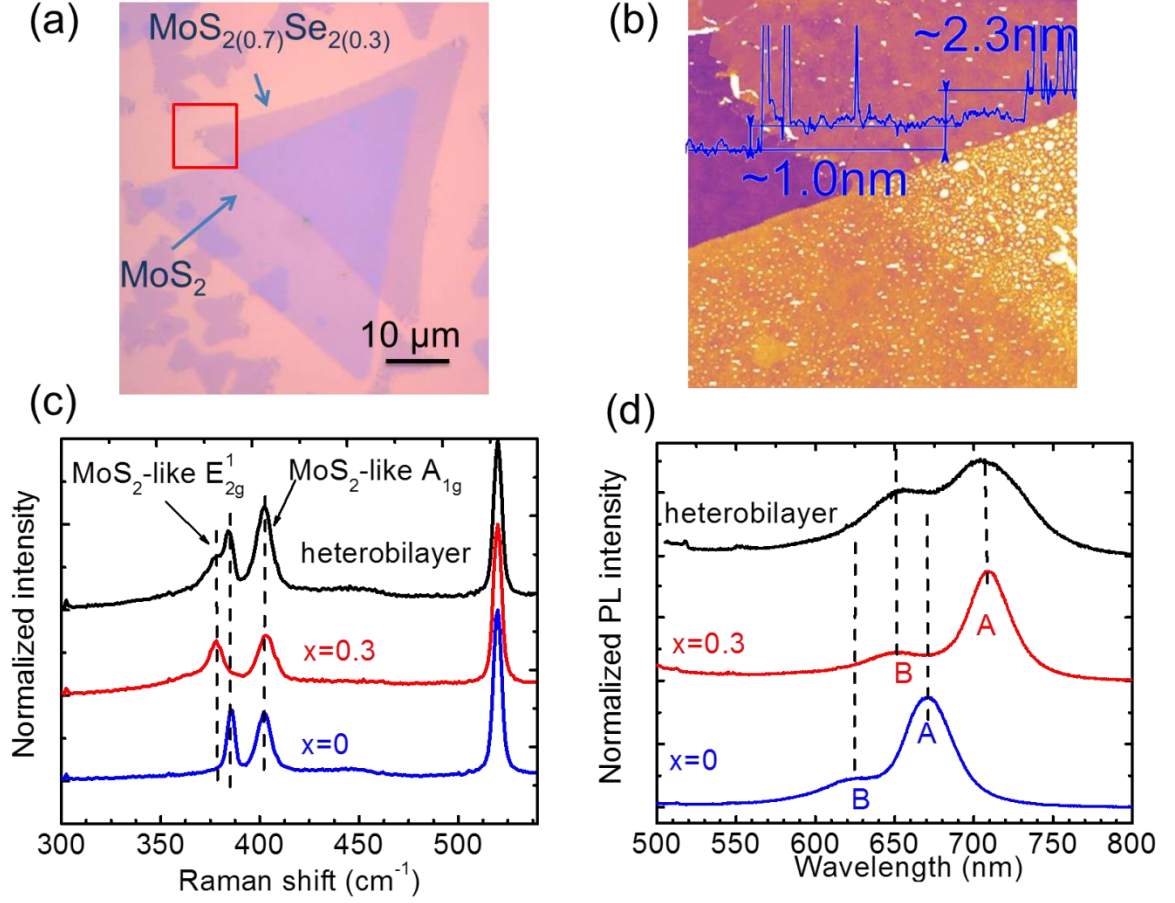


Figure 6-1: (a) OM image of a typical hetero-bilayer consisting of MoS₂ (top layer) and MoS_{2(0.7)Se_{2(0.3)} (bottom layer). (b) AFM image obtained from the red square in Fig.6-1(a) with the overlaid height profile. (c) Raman and (d) photoluminescence spectra acquired from this hetero-bilayer (black) and its constituent layers: MoS₂ (blue) and MoS_{2(0.7)Se_{2(0.3)} (red).}}

The excitonic states of our HSs were assessed with PL at room temperature. Two pronounced peaks at ~670 nm (~1.84 eV) and ~710 nm (~1.73 eV) in Fig. 6-1(d) correspond to the neutral *A*-excitonic transitions for monolayer MoS₂ and monolayer alloy, respectively. The strong PL emission reflects the direct bandgap nature of the monolayers. Additionally, *B*-excitonic transitions, which involves the second highest valence band due to the strong spin-orbit coupling, could also be observed at ~630 nm (~1.96 eV) and ~650 nm (~1.9 eV). Using the modified Vegard's law, we identified the Se composition from the spectral position of the *A*-exciton.

$$E_g(x) = xE_g(\text{MoSe}_2) + (1-x)E_g(\text{MoS}_2) - bx(1-x) \quad \text{Eq. (1)}$$

where $E_g(\text{MoS}_2) = 1.87$ eV, $E_g(\text{MoSe}_2) = 1.53$ eV, and the band-bowing parameter is given by $b = 0.05$.^[122, 127] Interestingly, we found that the PL spectrum of the HS (black trace in Fig. 6-1(d)) cannot be simply explained by any linear superposition of the PL spectra from the two constituting layers. This implies that interlayer optical transitions such as the one between the conduction band of MoS_2 and the valence band of $\text{MoS}_{2(0.7)}\text{Se}_{2(0.3)}$ may occur. Besides, we noted that the relative PL intensity of the HS is weaker than those of individual layers, indicating a good coupling between the two layers:^[156, 157] Typically, the PL is much weaker in a homo-bilayer when compared with that in a monolayer, which is also likely valid for our case of the hetero-bilayer of slightly different Se/S ratios. It is worth mentioning here that the black trace in Fig. 6-1(d) reflects the broadening the exciton resonance achieved by both intra-layer excitons and interlayer excitons. This in turn broadens the efficient SHG performance range as discussed below. Similar features were also observed from another hetero-bilayer with a different Se doping ratio ($x=0.45$), consisting of monolayer alloy $\text{MoS}_{2(0.45)}\text{Se}_{2(0.55)}$ and monolayer MoS_2 .

SHG produces a single photon at 2ω as a consequence of simultaneous absorption of two photons of a frequency at ω , as schematically illustrated in Fig.6-2(a). The process is typically virtual as it does not necessarily involve transitions to any real state. However, a resonance effect can occur provided the tunable virtual state by input-frequency tuning spectrally overlaps with the real *A*- and *B*-exciton states by two-photon resonance.^[149, 158] In our SHG measurement, the exciton resonance effect was assessed by varying the fundamental wavelength $\lambda = 1100$ nm – 1600 nm with sufficiently fine steps $\Delta\lambda = 5$ nm across the band edges of each individual layer. Fig. 6-2(b) shows the image of the hetero-bilayer seen through a CMOS camera. The orientation angle θ between the two emitted SHG fields from the constituent layers, as indicated by the red and blue arrows is nearly 0° . Therefore, the overall SHG intensity will be maximum owing to the constructive interference.

For comparison, Fig. 6-2(c) plots the wavelength-dependent SHG responses (solid symbol) of monolayer MoS_2 (blue), monolayer $\text{MoS}_{2(0.7)}\text{Se}_{2(0.3)}$ (red) and the hetero-bilayer (black), respectively. To correlate SHG enhancement with the exciton levels, the corresponding PL spectra (solid traces) were superimposed over the SHG spectra. The dramatic SHG enhancement can be clearly observed at wavelengths near the *A*- and *B*-

excitons. In particular, the SHG is greatly enhanced by 10 and 5 times for at A - and B -exciton for monolayer MoS_2 . Meanwhile, the SHG responses were intensified by 10 and 8 times for A - and B -exciton, respectively, compared with those at off resonance for monolayer alloy. Interestingly, the SHG response at B -excitonic transition from the alloy (red dots) was more intense when compared with that from pure MoS_2 (blue dots), in which the SHG response at B -excitonic transition (~ 630 nm) is significantly smaller than that at A -excitonic transition (~ 670 nm). A similar behavior was also observed from monolayer alloys with varying Se ratios in which we attributed this phenomenon to extrinsic effects related to defects and/or state broadening.[150] However, *Zhao et al.* reported that some binary monolayers such as $2H\text{-MoS}_2$ or $3R\text{-MoS}_2$ exhibit efficient SHG at the B -exciton resonance as strong as SHG at the A -exciton resonance.[159] Clearly, more investigation is required to resolve this issue. For VHS region, the resultant SHG reflected the constructive interference of both SHG signals from the constituents.

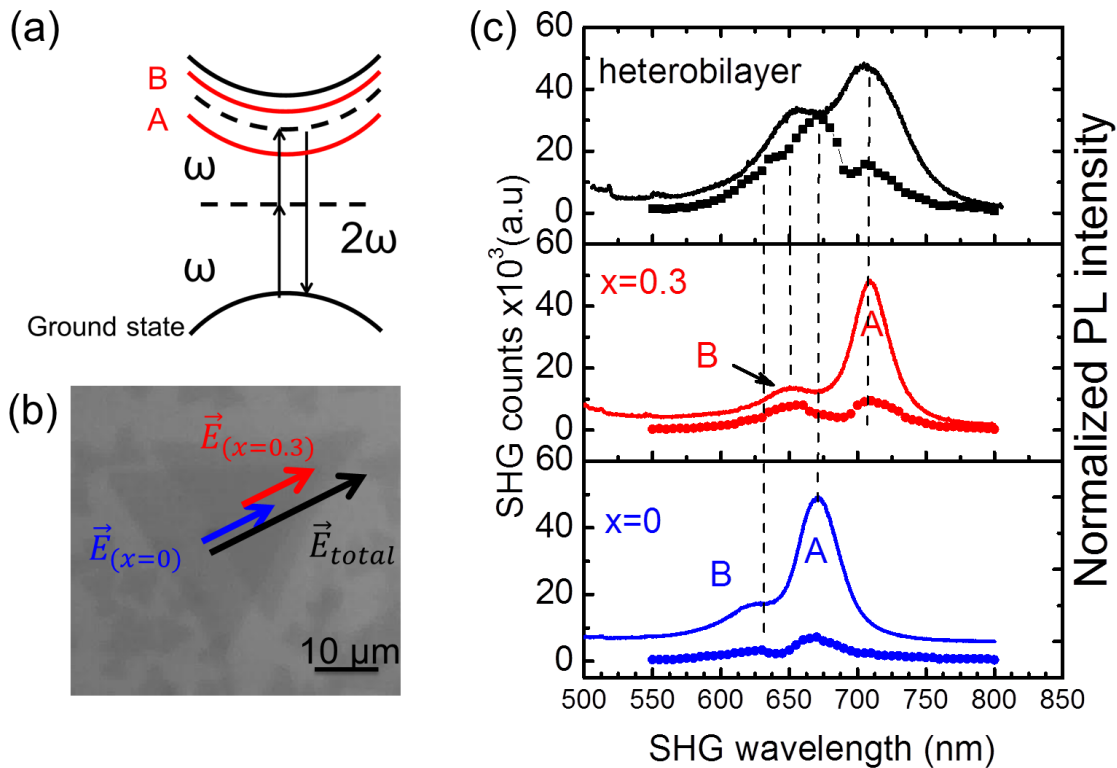


Figure 6-2: (a) Energy-level diagram for SHG in monolayer TMDC. The dashed lines represent virtual states and the solid lines represent real states in momentum space; A -

and B - exciton levels (red). (b) CMOS image of the hetero-bilayer. The arrows schematically represent the SHG fields of MoS_2 (blue), $\text{MoS}_{2(0.7)}\text{Se}_{2(0.3)}$ (red), and the hetero-bilayer (black), respectively. (c) SHG spectra (solid symbols) superimposed with the PL (solid traces) obtained from monolayer MoS_2 (bottom panel), monolayer $\text{MoS}_{2(0.7)}\text{Se}_{2(0.3)}$ (middle panel), and the hetero-bilayer (top panel). The dashed lines indicate the exciton resonances of the constituents.

We now discuss the SHG efficiency of the hetero-bilayer by directly comparing with that of the homo-bilayer ($\text{MoS}_2/\text{MoS}_2$). The dots in Fig. 6-3(a) correspond to the wavelength-dependent SHG response of the homo-bilayer. The red trace is the PL from the bilayer. In principle, SHG response is expected to vanish in an as-grown homo-bilayer due to the restoration of inversion symmetry in energetically stable AB Bernal stacking. However, in artificially stacked homo-bilayers, *Hsu et al.* showed that the SHG intensity is strongly dependent on the stacking angle between the constituent layers:[21]

$$I_S(2\omega) = I_1(2\omega) + I_2(2\omega) + 2\sqrt{I_1(2\omega)I_2(2\omega)} \cos 3\theta \quad \text{Eq. (2)}$$

where $I_S(2\omega)$, $I_1(2\omega)$, $I_2(2\omega)$ are the radiated SHG intensities from the homo-bilayer, the first monolayer, and the second bilayer, respectively, and θ is the associated stacking angle. When $\sim 0^\circ$, the SHG fields from each constituent layer coherently add up to yield four times stronger SHG than that from a monolayer. However, we observed SHG enhancement only a factor of ~ 2 at non-resonance range, while a factor of 4 is observed near A- and B-exciton of monolayer MoS_2 . The reason for a factor of 2 of SHG loss needed more additional experiments using higher repetition rate and shorter pulse duration to understand.

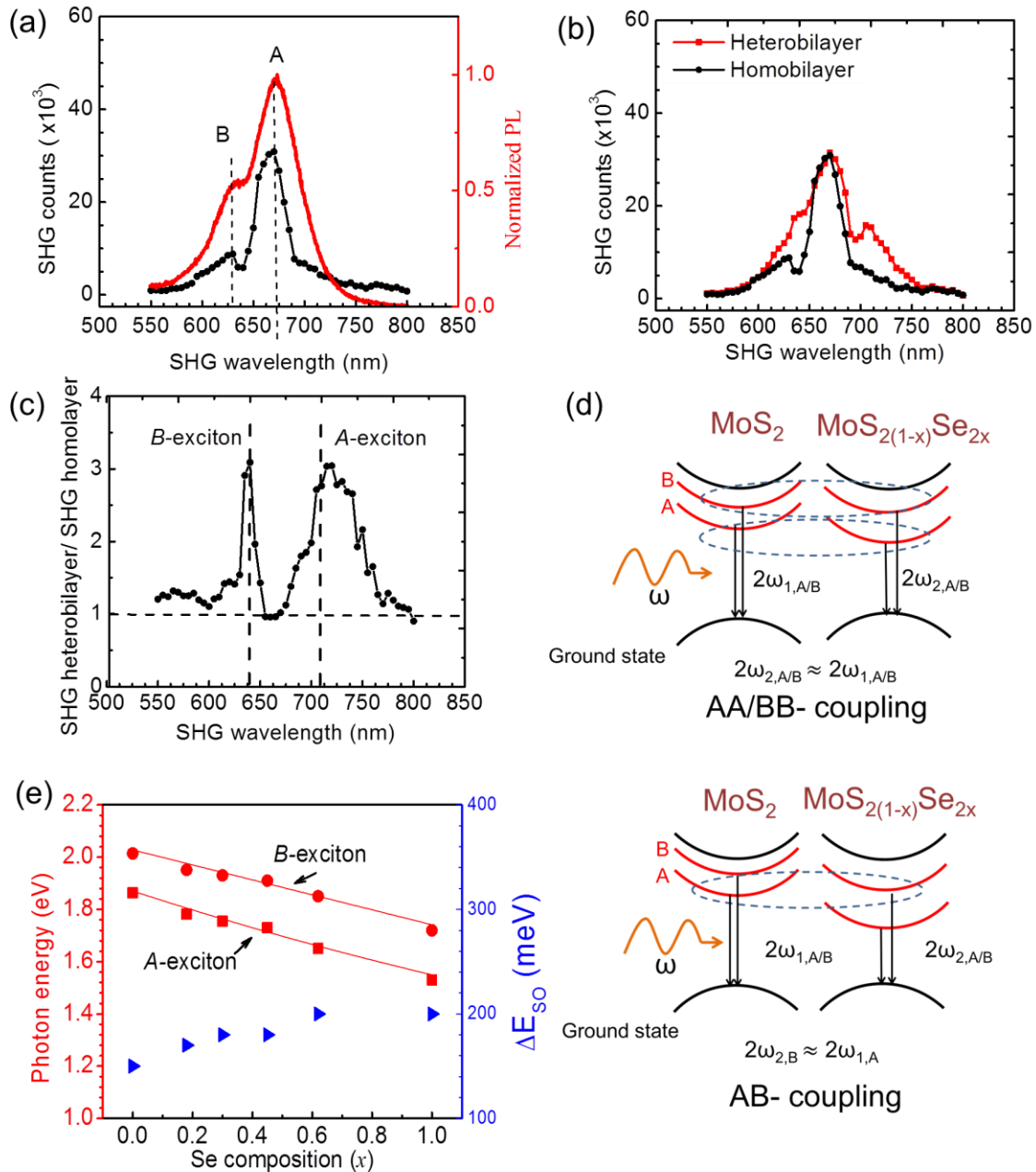


Figure 6-3. (a) Wavelength-dependent SHG from the homo-bilayer overlaid with the PL spectrum, clearly showing the A- and B- exciton resonances. (b) Comparison of the SHG intensities between the homo-bilayer (black: MoS₂/MoS₂) and the hetero-bilayer (red: MoS₂(0.7)Se₂(0.3)/MoS₂). (c) Ratio between the SHG intensities of the two samples, displaying the improved performance of the heterobilayer. (d) Spin-orbit splitting as a function of Se doping concentration x in our previous publication.[150](e) Schematic illustration of three possible SHG enhancements in the hetero-bilayer via AA-, BB-, and AB-couplings.

Interestingly, Fig. 6-3(b) shows that the hetero-bilayer (red) outperforms the homo-bilayer (black) in terms of the breath of the exciton resonance where the SHG efficiency is significantly enhanced. This effect is more clearly seen from Fig. 6-3(c), which plots the ratio between the red and the black in Fig. 6-3(b). Since the effect of Se doping on SHG in the alloy involves extension of the resonance width as well as enhancement of the *B*-exciton contribution (Fig. 6-2(c)), it is rather complicated to analyze the combined SHG effect from the hetero-bilayer ($\text{MoS}_{2(0.7)}\text{Se}_{2(0.3)}/\text{MoS}_2$), whereas the case for the homo-bilayer is straightforward (Fig. 6-4). For simplicity, however, we can roughly interpret the result in terms of a “resonance proximity effect” where the energetically close exciton states from different layers likely produce the coupling of SHG resonances. For bilayer stacking, there are three possible SHG couplings, *i.e.* *AA*-, *AB*- and *BB*-couplings, between *A*- and *B*-excitons of the top and bottom layers, which jointly and coherently contribute to the overall SHG response, as schematically illustrated in Fig. 6-3(e). In this scenario, the *BB*-coupling contributes to the SHG enhancement below 640 nm. The most striking effect was observed from the *AA*-coupling, rendering up to ~3 times more efficient SHG over a significant range of 700 nm – 750 nm. Moreover, there exists partial enhancement in the range of 640 nm – 700 nm that arises from the *AB*-coupling.

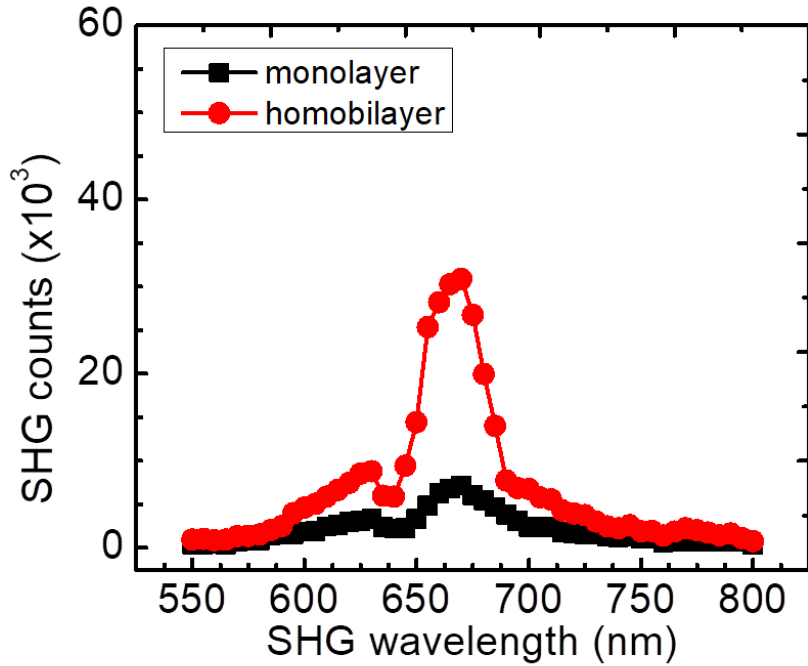


Figure 6-4 Wavelength dependent SHG for monolayer (black trace) and homobilayer (red trace) MoS₂.

This proximity effect demonstrates that Se doping in one monolayer plays a vital role to improve the overall SHG efficiency by exploiting the HS system, since the spectral structure of the resonance can be manipulated by tuning the Se concentration, x . In this sense, a detailed study on spin-orbit splitting in the valence bands as a function of x ($0 \leq x \leq 1$) would be beneficial for designing high-performance SHG devices derived from TMDCs. Generally, both A - and B -excitons redshift in energy with increasing x in MoS_{2(1-x)}Se_{2x} (Fig. 6-3(d)). We found that a more significant shift was observed (~ 1.83 eV – 1.53 eV) for the A -exciton, when compared with the B -exciton (~ 2.02 eV – 1.72 eV) as x varied from 0 to 1, which is consistent with the literatures.[57, 152] Most importantly, we experimentally showed that vertical stacking of monolayer alloys with different x is beneficial for enhancing SHG, which was also confirmed by our artificially stacked hetero-trilayer as further discussed later.

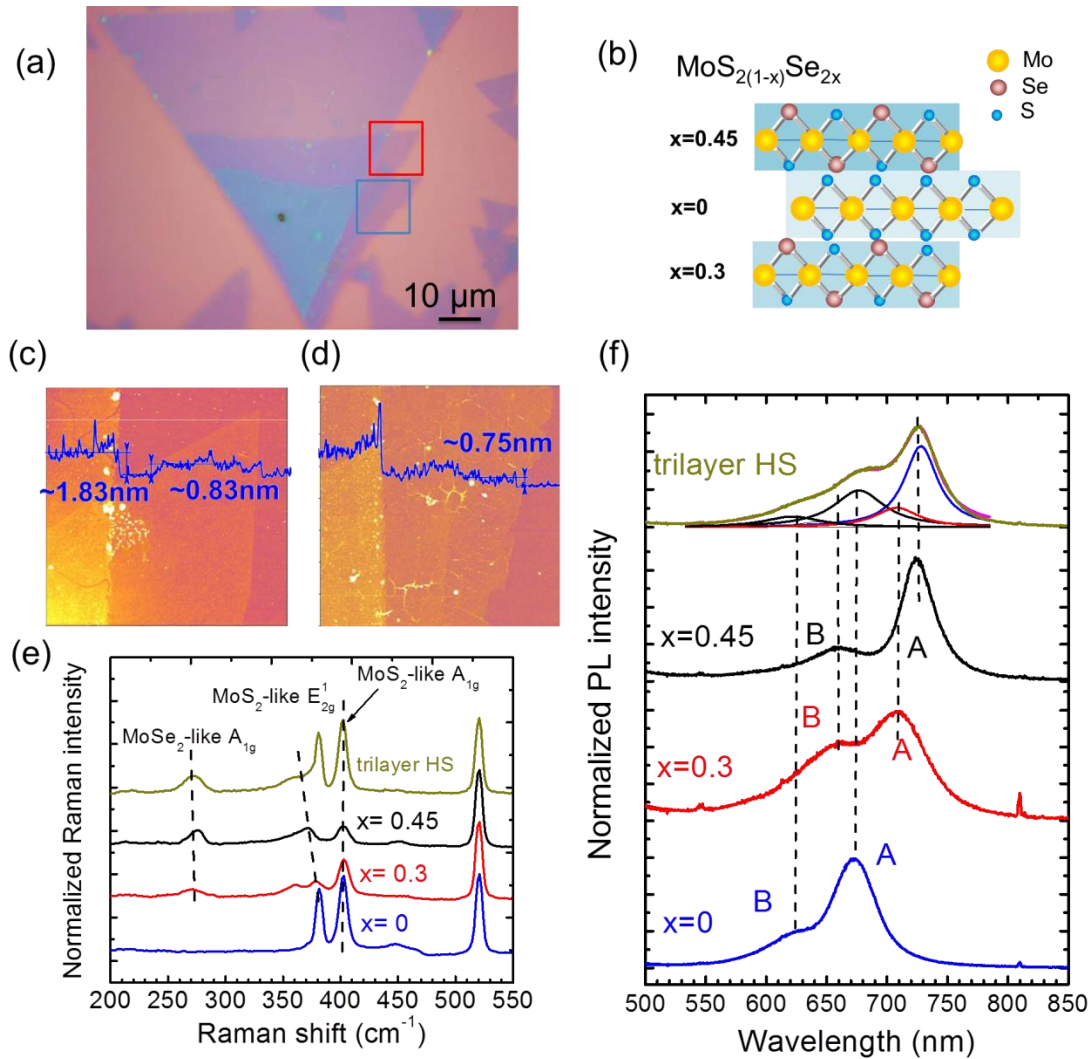


Figure 6-5. (a) OM image of the hetero-trilayer comprised of three layers with different Se concentrations. (b) Schematic illustration of the trilayer showing stacking order. AFM images measured at areas marked by (c) the red square and (d) the blue square in (a), respectively. (e) Raman spectra of the hetero-trilayer and its constituent layers. (f) Room-temperature PL spectra of the hetero-trilayer and its constituent layers.

In attempt to further enhance SHG, we designed a hetero-trilayer, comprised of three monolayers of pure MoS₂, MoS_{2(0.55)Se_{2(0.45)}}, and MoS_{2(0.7)Se_{2(0.3)}}, as depicted in Fig. 6-4(a). Here, the as-measured Se concentrations by spectroscopy were indeed initially chosen such that the exciton energies lie sufficiently close to each other to exploit the resonance proximity effect. The stacking configuration of the trilayer is displayed in Fig 6-4(b). The thicknesses

of the bottom layer and the bilayer were found to ~ 0.83 nm and ~ 1.83 nm, respectively, as shown in the AFM height profile (blue trace) in Fig 6-4(c). The thickness (~ 0.75 nm) of the top layer was measured separately as shown in the height profile of the AFM image (Fig 6-4(d)). Our AFM results confirm that all the layers in this HS are indeed monolayers. The green trace in Fig. 6-4(e) corresponds to the Raman spectrum of the hetero-trilayer. The MoS_2 -like A_{1g} characteristic peak remains almost unchanged in frequency through alloying, while the MoS_2 -like- E_{2g}^1 peak significantly downshifts in frequency. Note that these peaks become weaker in intensity with the increase of the Se concentration, x . Meanwhile, the stronger MoSe_2 -like A_{1g} peaks at $\sim 270.7 - 272.3$ cm^{-1} develop as x increases. This observation is in accordance with previous result.[152] Fig. 6-4(f) shows the PL spectra of the hetero-trilayer and its constituents measured at room temperature. By fitting the PL assuming a Lorentzian PL shape, we deconvoluted the A - and B -exciton PLs of each layers. Specifically, the noticeable peaks centered at ~ 675 nm (~ 1.84 eV), ~ 710 nm (~ 1.73 eV), and ~ 725 nm (~ 1.70 eV) can be assigned to A -excitonic transitions of pure MoS_2 , $\text{MoS}_{2(0.7)}\text{Se}_{2(0.3)}$ and $\text{MoS}_{2(0.55)}\text{Se}_{2(0.45)}$, whereas the broad peaks located at ~ 620 nm (~ 1.99 eV), ~ 645 nm (~ 1.91 eV) and ~ 655 nm (~ 1.89 eV) can be attributed to B -excitons of the corresponding layers. These peak positions match reasonably well with those in each individual layers as indicated by the dashed lines.

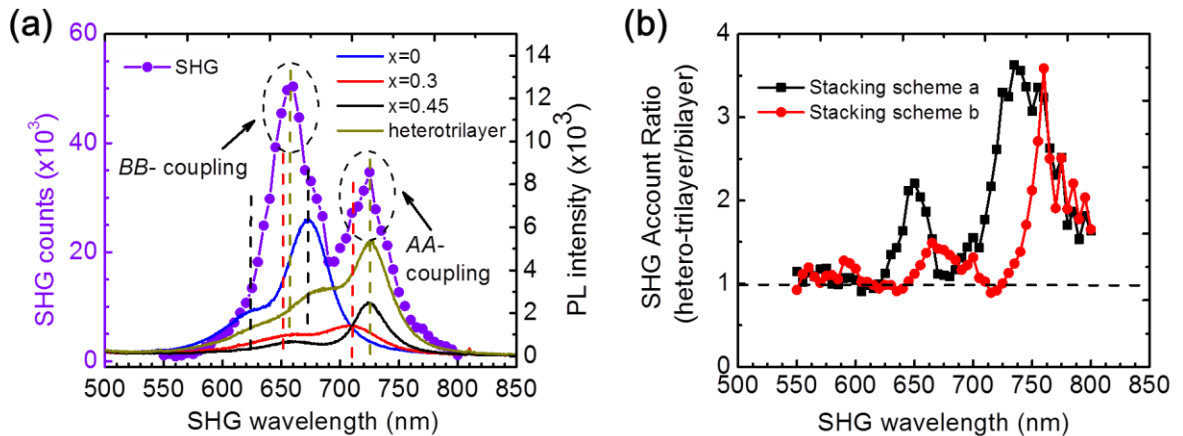


Figure 6-6 (a) Wavelength-dependent SHG measured from the hetero-trilayer (purple) overlaid with the PL spectra from individual layers; monolayers $\text{MoS}_{2(1-x)}\text{Se}_{2x}$; $x=0$ (blue), 0.3 (red), 0.45 (black), and the hetero-trilayer (dark yellow). The spectral locations for the resonance are indicated by the dashed lines of the corresponding color. (b) Comparison of the

SHG efficiency of the two hetero-trilayers prepared with different stacking schemes; 1) $x = 0.45$ (black) and 2) $x = 0.62$ (red) in the third layer, whereas the bottom bilayers are identical in chemical composition, i.e., the hetero-bilayer ($\text{MoS}_{2(0.7)}\text{Se}_{2(0.3)}/\text{MoS}_2$). See SI for the latter case of the trilayer. Here, each SHG efficiency is scaled by that of the hetero-bilayer in **Fig. 6-3(b)**.

Fig. 6-5(a) shows the broadband SHG response of the hetero-trilayer (purple), overlaid with the PL spectra from each constituent and the trilayer itself. The SHG resonances become readily distinguishable by comparing with the PL spectra of individual constituents in the HS system. Particularly, the strongest SHG response was found in wavelengths between 650 nm – 670 nm, which arises most likely from the approximate triple overlapping of *BBA*-coupling in the alloys and MoS_2 , respectively. The proximity effect in the *BB*-coupling is remarkably stronger when the two constituent alloy layers have a small difference in ΔE_{s0} . The *A*-excitonic related features of MoS_2 and $\text{MoS}_{2x}\text{Se}_{2(1-x)}$ ($x=0.3$) can be respectively seen as shoulder peaks at ~670 nm and ~710 nm, whereas that of $\text{MoS}_{2x}\text{Se}_{2(1-x)}$ ($x=0.3$) manifests itself as a pronounced peak around 725 nm. Compared to the hetero-bilayer, which has two layers with the same Se doping concentrations, the enhancement of SHG efficiency happens especially strongly near *A*- and *B*-excitons range of the additional layer, as shown in Fig. 6-5(a). However, the expected SHG enhancement factor of ~2.25 could not be seen at the non-resonance range in which the wavelength is below 600 nm. This can probably be attributed to optical degradation. This hypothesis is clearly required further experiments to confirm. Our conceptual study indicates that one can continuously improve the SHG performance in a vertical HS system by carefully stacking more layers of varying Se compositions but with the same orientation, especially via the resonance proximity effect across the constituents. A similar behavior was observed for another trilayer prepared with a different stacking configuration with the top layer having a high Se concentration ($x= 0.62$) (see Fig. 6-6).

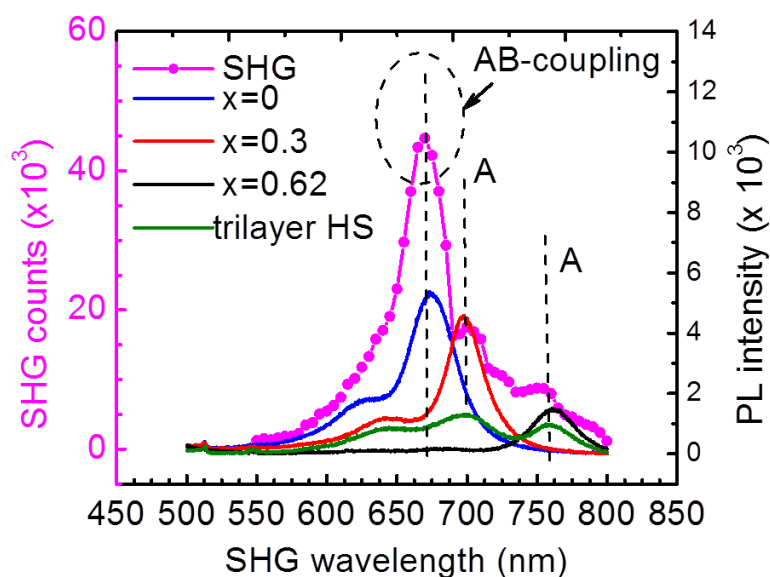


Figure 6-7: Wavelength-dependent SHG measured from the hetero-trilayer (pink) overlaid with the PL spectra from individual layers; monolayers $\text{MoS}_{2-x}\text{Se}_{2(x-1)}$; $x=0$ (blue), 0.3 (red), 0.62 (black), and the hetero-trilayer (green).

Although it also has a high SHG efficiency especially in the range of 650 nm - 670 nm due to strong *AB*-coupling between the alloy and pure monolayers, its SHG performance is less efficient at longer wavelengths. Specifically, broader SHG enhancement was clearly observed for the stacking scheme (1) than that the stacking scheme (2) at near-IR ranges (~700 nm – 750 nm), as evident in Fig. 6-5(b). The better SHG performance of the former trilayer suggests that the proximity effect can be maximally utilized for building a highly efficient wavelength converter by deliberately choosing monolayers with a series of similar Se doping concentrations. In other words, vertical stacking of multiple alloy layers with gradual increase in the Se concentration would provide a new venue for wider and stronger SHG performance.

6.3 Chapter summary:

In summary, we probed the SHG characteristics across the bandgap edges of monolayer MoS_2 and its alloys in vertical stacked HSs systems including homo-bilayer, hetero-bilayer and hetero-trilayer using pico-second pulsed laser excitation source. Intriguingly, we found that stacking of monolayer MoS_2 with its gradually increased alloys

will broaden the resonant SHG performance from visible to near IR range. Unfortunately, we could not assess the exact $\chi^{(2)}$ values for our heterobilayers and heterotrilayers. However, these results preliminarily showed the feasibility of artificial broadband materials by using vertically stacked monolayers of different TMDCs materials. This work is still ongoing. Although the scope of this study is limited to monolayer MoS₂ and its alloys, we believe that the outcomes of this study will contribute to solving the quest of artificial nonlinear optical materials for even more broad spectral range.

Conclusion:

The advanced analysis and successive scientific discoveries provides the better understanding for scientists about the chemical, physical and mechanical properties of materials. In return, material scientists with state-of-art growth techniques supplies novel materials with intriguing and tunable properties subjected not only to fundamental studies but also further to industrial field. This mutual interaction gains more physical insight of material science. In this case, this is physical science in 2D monolayer TMDCs.

In this work, I have successfully grown continuous, large-sized monolayer TMDCs, specifically MoX_2 and their ternary alloys using chemical vapor deposition. The quality of continuous film was confirmed by different analysis techniques such as Raman and photoluminescence spectroscopy, atomic force microscopy, X-ray photoemission. The quality of as-grown specimens is comparable to the mechanically exfoliated specimens. The tunable band-gap monolayers were also synthesized by adopting chemical vapor deposition. I have basically characterized the electrical performance of Metal-Semiconductor-Metal photodetector based on monolayer MoS_2 . Although there is a degradation issue on grain boundaries of continuous MoS_2 that have to be addressed, but its potential use for new-generation fast response and high performance is rather high.

Additionally, I have provided the comprehensive study on NLO properties of monolayer TMDC. This NLO have been assessed using the low repetition rate pulsed laser and different measurement geometries. Broadband $\chi^{(2)}$ dispersion were estimated for monolayer MoX_2 as well as their ternary alloys. The SHG signals are resonant with excitonic states for pure monolayers grown on different substrates. I also demonstrated that by varying the Se doping concentration in monolayer alloys, the SHG resonance can spectrally tuned in wide spectral range. Finally, I provided preliminary evidences that stacked heterostructures comprised of monolayers $\text{MoS}_{2(1-x)}\text{Se}_{2x}$ can be exploited in order to spectrally stretching the SHG resonance. By designing the 2D Van der Waal heterostructures, I showed that the SHG performance can be improved based on the spectral peak position of intralayer A- and B-exciton. However, there is some technical limitation when using picosecond pulsed laser to measure hetero multilayers. The balance between sufficient signal-to-noise and monitoring beam size without damaging the stacked area is very hard to achieve using low repetition rate laser. Another challenge is that stacked area is smaller than laser beam size. Then, the exact

value of $\chi^{(2)}$ stacked areas could not precisely assessed. Therefore, it is necessary to employ pulsed laser with either higher repetition rate (GHz/MHz) or shorter pulse duration (fs pulsed laser) in the future work.

Publication:

A. Peer reviewed papers

- 1) (In press) Friction Characteristics of Mechanically Exfoliated and CVD-grown Single-layer MoS₂, Dinh Le Cao Ky , Bien-Cuong Tran Khac, Chinh Tam Le, Yong Soo Kim and Koo-Hyun Chung*, Friction (IF 1.405 @2016, ISSN: 2223-7690)
- 2) Growth and Simultaneous Valleys Manipulation of Two-Dimensional MoSe₂-WSe₂ Lateral Heterostructure, Farman Ullah, Yumin Sim, Chinh Tam Le, Maeng-Je Seong, Joon I. Jang,* Sonny H. Rhim, Bien Cuong Tran Khac, Koo-Hyun Chung, Kibog Park, Yangjin Lee, Kwanpyo Kim, Hu Young Jeong and Yong Soo Kim*, ACS Nano 11(9), 8822-8829 (2017) (IF 13.334 @2016, <5%, ISSN: 1477-9234) (DOI: 10.1021/acsnano.7b02914) (2017.09.26)
- 3) Impact of Selenium Doping on Resonant Second Harmonic Generation in Monolayer MoS₂, Chinh Tam Le, Daniel J. Clark, Farman Ullah, Velusamy Senthilkumar, Sonny. H. Rhim, Joon I. Jang*, Yumin Sim, Maeng-Je Seong, Koo. Hyun Chung, Yong Soo Kim*, ACS Photonics 4, 38-44 (2017) (DOI:10.1021/acsp Photonics.6b00530) (ISSN: 2330-4022) (IF 6.756 @2016, <10 % optics catalog) (2017.01.18)
- 4) Pulsed laser deposition assisted grown continuous monolayer MoSe₂, Farman Ullah, Tri Khoa Nguyen, Chinh Tam Le and Yong Soo Kim*, CrystEngComm (Crystal Engineering Communications) 18, 6992-6996 (2016), DOI: 10.1039/C6CE01392A (ISSN: 1466-8033, IF: 3.474 @2016, < 20%, publisher: RSC), (2016.10.07)
- 5) Continuous large area few layers MoSe₂ films by pulse laser deposition and effect of annealing in sulfur environment, Farman Ullah, Velusamy Senthilkumar, S.-H. Kim, Chinh Tam Le, Huh Rock, D. -Y. Lee, S. Park, Ahmed. I. Ali, and Yong Soo Kim*, Journal of Nanoscience and Nanotechnology (J. Nanosci. Nanotech.) 16(10), 10284-10289 (2016) (doi:10.1166/jnn.2016.13145) (IF: 1.339@2013, ISSN: 1533-4880, <60%) (2015. 10. 01)
- 6) Nonlinear optical characteristic of monolaye MoSe₂, Chinh Tam Le, Daniel J. Clark,

Farman Ullah, Velusamy Senthilkuma, Joon I. Jang*, Yumin Sim, Maeng-Je Seong, Koo-Hyun Chung, Hyoyeol Park, and Yong Soo Kim*, *Annalen der Physik (Ann. Phys.)* 528(7-8), 551-559 (2016) (DOI: 10.1002/andp.201600006, Jan. 16, 2016) (IF: 3.039 @2016, ISSN:0003-3804, < 20%, publisher; Wiley-VCH (Backside Cover Picture))

- 7) Temperature dependence of the critical points of monolayer MoS₂ film by ellipsometry, Han Gyeol Park, Tae Jung Kim, Hwa Seob Kim, Chang Hyun Yoo, Nilesh S. Barange, Van Long Le, Hyoung Uk Kim, Velusamy Senthilkumar, Chinh Tam Le, Yong Soo Kim*, Maeng-Je Seong, and Young Dong Kim*, *Applied Spectroscopy Reviews (Appl. Phys. Rev.)* 51(7-9), 621-636 (2016) (DOI: 10.1080/05704928.2016.1166436) (IF: 4.254@2016, < 5%, ISSN 0570-4928) (2016.03.23)
- 8) Erratum: Strong optical nonlinearity of CVD-grown MoS₂ monolayer as probed by wavelength-dependent second, Daniel. J. Clark, Velusamy Senthilkumar, Chinh Tam Le, D. L. Weerawarne, Bonggu Shim, Joon Ik Jang*, J. H. Shim, J. Cho, Yumin Sim, Maeng-Je Seong, Sonny. H. Rhim, A. J. Freeman, Koo. Hyun Chung and Yong Soo Kim*, *Phys. Rev. B* 92, 159901(E) (2015) (DOI:10.1103/PhysRevB.92.159901),(IF: 3.838, @ 2016, <40%) (2015. 10. 12)
- 9) Near bandgap second-order nonlinear optical characteristics for MoS₂ monolayer transferred on transparent substrate, Daniel. J. Clark, Chinh Tam Le, Velusamy Senthilkumar, Farman Ullah, Heung-Yeol Cho, Yumin Sim, Maeng-Je Seong, K. -H. Chung, Y. S. Kim*, and J. I. Jang, *Applied Physics Letters (Appl. Phys. Lett.)* 107, 131113-5 pages (2015) (DOI <http://dx.doi.org/10.1063/1.4932134> (IF: 3.41 @2016, < 20%) (2015.10.01)
- 10) Photosensitive study of metal-semiconductor-metal photodetector based on chemical vapor deposited monolayer MoS₂, Chinh Tam Le, Velusamy Senthilkumar, Yong Soo Kim*, *Journal of Nanoscience and Nanotechnology (J. Nanosci. Nanotech.)* 15, 8133-8138 (2015) (IF: 1.483@2016, ISSN: 1533-4880,<60%, DOI:10.1166/jnn.2015.11255) (2015. 10. 01)
- 11) Direct vapor phase growth process and robust optical properties of large area MoS₂ layer,

V. Senthilkumar, Le C. Tam, Yong Soo Kim,* Yumin Sim, Maeng-Je Seong, Joon I. Jang, Nano Research 7(12), 1759-1768 (2014) (DOI 10.1007/s12274-014-0535-7) (IF: 7.354 @2016, ISSN: 1998-0124, < 10%) (2014.12.01)

12) Strong optical nonlinearity of MoS₂ monolayer as probed by wavelength-dependent second harmonic generation, Daniel. J. Clark, Velusamy Senthilkumar, Chinh Tam Le, D. L. Weerawarne, Bonggu Shim, Joon Ik Jang*, J. H. Shim, J. Cho, Yumin Sim, Maeng-Je Seong, Sonny. H. Rhim, A. J. Freeman, Koo. Hyun Chung and Yong Soo Kim*, Physical Review B 90(12), 121409(R)-5 (2014) (IF: 3.664@2013, ISSN: 1098-0121, <20%)

B. International Conference Meetings

1) (Poster) Monolayered MoSe₂-WSe₂ lateral heterostructure growth and its potential use in valleytronics, Farman Ullah, Chinh Tam Le, Yumin Sim, Maeng-Je Seong, Joon I. Jang, The 22nd International Conference on Electronic Properties of Two-Dimensional Systems (EP2DS-22) and 18th International Conference on Modulated Semiconductor Structures, Penn State University, USA.

2) (Invite Talk) 2D Semiconductor, transitional metal dichalcogenide growth and its application, Yong Soo Kim*, Chinh Tam Le, Farman Ullah, and Joon I. Jang, The 3rd International Workshops on Nano Materials for Energy Conversion (NMEC-2017), NMEC-2017 Programs and Abstract, p.70-73, Ho Chi Minh City, Vietnam.

3) (Poster) Synthesis of high quality monolayer WS₂ using chemical vapor deposition, Chinh Tam Le, Farman Ullah, Jong-Won, Yun, Yong Soo Kim*, American Physical Society March Meeting (APS March Meeting, 2017) Bulletin of the American Physical Society 62(4), p.53, New Orleans, Louisiana, USA.

4) (Oral) Polarization resolved photoluminescence study of pulse laser deposition assisted grown monolayer MoSe₂-WSe₂ lateral heterojunction, Farman Ullah, Chinh Tam Le, Tri Khoa Nguyen, Jong-Won Yun and Yong Soo Kim*, American Physical Society March Meeting (APS March Meeting, 2017), Bulletin of the American Physical Society 62(4), p.48, New Orleans, Louisiana, USA.

5) (Invite Talk) Atomically Thin Semiconductor, Transition Metal Dichalcogenides Growth and Its Nonlinear Optical Characteristics, Velusamy Senthilkumar, Chinh Tam Le,

Farman Ullah, Daniel J. Clark, Joon Ik Jang, and Yong Soo Kim*, SEMICON KOREA, SEMI Technology Symposium (STS) 2017, S2; Advanced Process Technology; Dielectric, Metals and other Materials, COEX, Seoul, Korea.

6) (Poster) Hydrogen Evolution Reaction Enhancement of CVD-growth Continuous Monolayer MoS₂ Film using a Pretreated Substrate, Heung-Yeol Cho, Tri Khoa Nguyen, Chinh Tam Le and Yong Soo Kim*, JSAP (The Japan Society of Applied Physics) Kyushu Annual Meeting 2016 Int'l Session; Tsushima, Japan, p. 11.

7) (Poster) Hydrogen evolution reaction enhancement of CVD-growth continuous monolayer MoS₂ film using a pretreated substrate, Heung-Yeol Cho, Tri Khoa Nguyen, Chinh Tam Le, Farman Ullah, Jong-Won Yun and Yong Soo Kim, 3rd International Symposium on Frontier in Materials Science, FMS2016, 2016, Hanoi, Vietnam

8) (Oral) Plasma treated MoS₂ basal planes for application in hydrogen evolution reaction, Tri Khoa Nguyen, Chinh Tam Le, Farman Ullah, Yong Soo Kim*, 3rd International Symposium on Frontier in Materials Science, FMS2016, Sep. 28-30, 2016, Hanoi, Vietnam

9) (poster) Spectroscopic Ellipsometry Study on the Temperature Dependent Optical Properties of Monolayer MoS₂ from 35 to 350 K, Hwa Seob Kim, Han Gyeol Park, Tae Jung Kim, Le Van Long, Chinh Tam Le, Yong Soo Kim, Maeng-Je Seong, and Young Dong Kim, 33rd International Conference on the Physics of Semiconductors (ICPS2016), Beijing China, Abstract, p.532

10) (Oral) Se doping-induced tunability of second harmonic generation of monolayer, Chinh Tam Le, Daniel J. Clark, Velusamy Senthilkumar, Joon Ik Jang and Yong Soo Kim*, 33rd International Conference on the Physics of Semiconductors (ICPS2016) Beijing China, Abstract, p.374

11) (Oral) Tunable second harmonic generation of monolayer MoS₂ by Se doping, Chinh Tam Le, Daniel J.Clark, Velusamy Senthilkumar, Joon Ik Jang, Heung-Yeol Cho, and Yong Soo Kim, American Physical Society March Meeting (APS March Meeting, 2016), Baltimore, ML, USA, p 657.

12) (Poster) Temperature dependence of critical points of monolayer MoS₂ film by ellipsometry, Han Gyeol Park, Tae Jung Kim, Hwa Seob Kim, Chang Hyun Yoo, Nilesh S. Barange, Le Van Long, Hyoung Uk Kim, Yong Soo Kim, Velusamy Senthilkumar, Chinh Tam Le, Young Dong Kim, The 2nd International conference & exhibition for Nanopia,

Nanopia 2015

13) (Poster) Ellipsometric Study on the Temperature Dependent Dielectric Function of Monolayer MoS₂, Hwa Seob Kim, Han Gyeol Park, Tae Jung Kim, Chang Hyun Yoo, Velusamy Senthilkumar, Yong Soo Kim, Chinh Tam Le, Young Dong Kim, The 9th International Conference on Advanced Materials and Devices (ICAMD 2015), p86, Jeju, Korea.

14) (Poster) Strong optical nonlinearity of CVD-grown Mo(S,Se)₂ monolayer as probed by wavelength-dependent second harmonic generation, Chinh Tam Le, Yong Soo Kim*, The 9th International Conference on Advanced Materials and Devices (ICAMD 2015), p.76, Jeju, Korea.

15) (Poster) Synthesis of band-gap tunable monolayered-MoS₂xSe_{2(1-x)} alloys, Chinh Tam Le, Velusamy Senthilkumar, Yumin Sim, Mae -Je Seong and Yong Soo Kim*, International Workshop on Nanoscience and Nanotechnology and Joint 4th Asia-Pacific Chemical and Biological Microfluidics Conference (IWNN-PCBM 2015), Danang, Vietnam.

16) (Invite talk) Next generation MoX₂ (X; S, Se) monolayer-based nanoscale nonlinear optics devices, Chinh Tam Le, Velusamy Senthilkumar, Daniel J. Clark, Joon Ik Jang and Yong Soo Kim*, International Workshop on Nanoscience and Nanotechnology and Joint 4th Asia-Pacific Chemical and Biological Microfluidics Conference(IWNN-PCBM 2015), Danag, Vietnam.

17) (poster) Critical Points of Monolayer MoS₂ Film by Spectroscopic Ellipsometry, Han Gyeol Park, Tae Jung Kim, J. C. Park, K. H. Nam, Le Van Long, Yong Soo Kim, Velusamy Senthilkumar, Chinh Tam Le, and Young Dong Kim, The 21st International Conference on Electronic Properties of Two-Dimensional Systems (EP2DS-21) and 17th International Conference on Modulated Semiconductor Structures, Sendai, Japan.

18) (poster) Controlled synthesis of single layer MoSe₂ by chemical vapor deposition, Chinh Le Tam, V. Senthilkumar, Y. Sim, M.-J. Seong, Yong Soo Kim*, International Symposium on Nano-Materials, Technology and Application (NANOMATA 2014), Hanoi, Vietnam, p125-126

19) (poster) Wafer-level uniform few-layer MoS₂ by chemical vapor deposition, Chinh Le Tam, V. Senthilkumar, Y. Sim, M.-J. Seong, Yong Soo Kim*, The 12th Int. National Symposium & Nano-convergence Expo. (Nano-Korea 2014), Seoul, Korea, p. 72.

() Domestic Conference Meetings

1) (Invite Talk) 2D Semiconductor, Transition Metal Dichalcogenides Growth and Its Applications, Yong Soo Kim*, Chinh Tam Le, Farman Ullah, Joon. I. Jang, 한국자기학회 2017 년도 임시총회 및 하계학술연구발표대회, 논문개요집, p.43, 부산, 한화리조트 해운대 티블리

2) (Oral) Tuning resonant second harmonic generation of monolayer MoS₂ by selenium doping, Chinh Tam Le, Farman Ullah, Sonny H. Rhim, Joon Ik Jang, Koo Hyun Chung, Maeng-Je Seong, Sungkyun Park, Yong Soo Kim, 한국물리학회 2016 년 가을 학술논문발표회 및 임시총회 (한국물리학회), 한국물리학회 회보 34(2), p.32, 김대중컨벤션센터.

3) (Oral) Synthesis and Characterization of Three Monolayer Thick Continuous Uniform Tungsten Selenide Film, Farman Ullah, Chinh Tam Le, Heung-Yeol Cho, Ahmed I. Ali, Yong Soo Kim*, 한국물리학회 2016 년 봄 학술논문발표회 및 제 92 회 정기총회 (한국물리학회), 한국물리학회 회보 34(1), p.65, 대전컨벤션센터.

4) (Oral) Polarized Raman and Photoluminescence spectroscopy with differing angles of laser incidence on a single layer MoS₂, Hyun-Jai, Ahn, Velusamy Senthilkumar, Chinh Tam Le, Yong Soo Kim, Maeng-Je Seong, 한국물리학회 2016 년 봄 학술논문발표회 및 제 92 회 정기총회 (한국물리학회), 한국물리학회 회보 34(1), p.43, 대전컨벤션센터.

5) (Poster) Highly crystalline monolayer MoSe₂ flakes and continuous film by selenization of pre-deposited Molybdenum trioxide (MoO₃) thin film by pulse laser deposition, Farman Ullah, Chinh Tam Le, V. Senthilkumar, Sun Ho Kim, and Yong Soo Kim*, 한국물리학회 2015 년 가을 학술논문발표회 및 제 92 회 임시총회 (한국물리학회), 한국물리학회 회보 33(2), p.105, 화백컨벤션센터.

6) (Poster) Controllable Grain Size Distribution and Readily Transferable Growth of

MoS₂ Monolayer Flakes Using a Seed of PTAS by CVD Process. H.-Y. Cho, Chinh Tam Le, Velusamy Senthilkumar, and Yong Soo Kim*, 한국물리학회 2015 년 가을 학술논문발표회 및 제 92 회 임시총회 (한국물리학회), 한국물리학회 회보 33(2), p.147, 화백컨벤션센터.

7) Second harmonic generation of monolayer CVD-grown MoSe₂, Chinh Tam Le, Daniel J. Clark, Velusamy Senthilkumar, Joon Ik Jang, 조홍열, Yong Soo Kim*, 2015 년 봄 학술논문발표회 및 제 91 회 정기총회 (한국물리학회), 한국물리학회 회보 33(1), p.117 대전컨벤션센터(DCC).

8) Polarized Raman Spectroscopy with Differing Angles of Laser Incidence on a Few Layers of MoS₂ GeunHeo, Velusamy Senthilkumar, Tam Le Chinh, Maeng-Je Seong and Yong Soo Kim, 2014 년 봄 학술논문발표회 및 제 50 회 정기총회 (한국물리학회), 한국물리학회 회보 32(1), p.53 (2014.04.23-25), 대전컨벤션센터(DCC).

References

- [1] Vogel, E. M.; Robinson, J. A. *Mater. Res. Bull.* **2015**, 40, 558-563.
- [2] Joensen, P.; Frindt, R.; Morrison, S. R. *Mater. Res. Bull.* **1986**, 21, 457-461.
- [3] Xu, M.; Liang, T.; Shi, M.; Chen, H. *Chem. Rev.* **2013**, 113, 3766-3798.
- [4] Shi, Y.; Zhang, H.; Chang, W.-H.; Shin, H. S.; Li, L.-J. *Mater. Res. Bull.* **2015**, 40, 566-576.
- [5] Chhowalla, M.; Voiry, D.; Yang, J.; Shin, H. S.; Loh, K. P. *Mater. Res. Bull.* **2015**, 40, 585-591.
- [6] Acerce, M.; Voiry, D.; Chhowalla, M. *Nat. nanotechnol.* **2015**, 10, 313-318.
- [7] Koster, G. F. *Properties of the thirty-two point groups*. The MIT Press: 1963; Vol. 24.
- [8] Ye, J.; Zhang, Y.; Akashi, R.; Bahramy, M.; Arita, R.; Iwasa, Y. *Science* **2012**, 338, 1193-1196.
- [9] Castellanos-Gomez, A.; Barkelid, M.; Goossens, A.; Calado, V. E.; van der Zant, H. S.; Steele, G. A. *Nano Lett.* **2012**, 12, 3187-3192.
- [10] Lu, X.; Utama, M. I. B.; Zhang, J.; Zhao, Y.; Xiong, Q. *Nanoscale* **2013**, 5, 8904-8908.
- [11] Liu, Y.; Nan, H.; Wu, X.; Pan, W.; Wang, W.; Bai, J.; Zhao, W.; Sun, L.; Wang, X.; Ni, Z. *ACS nano* **2013**, 7, 4202-4209.
- [12] Yu, Y.; Li, C.; Liu, Y.; Su, L.; Zhang, Y.; Cao, L. *Sci. Rep.* **2013**, 3.
- [13] Xia, J.; Huang, X.; Liu, L.-Z.; Wang, M.; Wang, L.; Huang, B.; Zhu, D.-D.; Li, J.-J.; Gu, C.-Z.; Meng, X.-M. *Nanoscale* **2014**, 6, 8949-8955.
- [14] George, A. S.; Mutlu, Z.; Ionescu, R.; Wu, R. J.; Jeong, J. S.; Bay, H. H.; Chai, Y.; Mkhoyan, K. A.; Ozkan, M.; Ozkan, C. S. *Adv. Funct. Mater.* **2014**, 24, 7461-7466.
- [15] Chernikov, A.; van der Zande, A. M.; Hill, H. M.; Rigosi, A. F.; Velauthapillai, A.;

-
- Hone, J.; Heinz, T. F. *Phys. Rev. Lett.* **2015**, 115, 126802.
- [16] Cheiwchanchamnangij, T.; Lambrecht, W. R. *Phys. Rev. B* **2012**, 85, 205302.
- [17] He, K.; Kumar, N.; Zhao, L.; Wang, Z.; Mak, K. F.; Zhao, H.; Shan, J. *Phys. Rev. Lett.* **2014**, 113, 026803.
- [18] Qiu, D. Y.; Felipe, H.; Louie, S. G. *Phys. Rev. Lett.* **2013**, 111, 216805.
- [19] Hanbicki, A.; Currie, M.; Kioseoglou, G.; Friedman, A.; Jonker, B. *Solid State Commun.* **2015**, 203, 16-20.
- [20] Perkins, F. K.; Friedman, A. L.; Cobas, E.; Campbell, P.; Jernigan, G.; Jonker, B. T. *Nano Lett.* **2013**, 13, 668-673.
- [21] Hsu, W.-T.; Zhao, Z.-A.; Li, L.-J.; Chen, C.-H.; Chiu, M.-H.; Chang, P.-S.; Chou, Y.-C.; Chang, W.-H. *ACS nano* **2014**, 8, 2951-2958.
- [22] Pospischil, A.; Furchi, M. M.; Mueller, T. *Nat. nanotechnol.* **2014**, 9, 257-261.
- [23] Lee, C.-H.; Lee, G.-H.; Van Der Zande, A. M.; Chen, W.; Li, Y.; Han, M.; Cui, X.; Arefe, G.; Nuckolls, C.; Heinz, T. F. *Nat. nanotechnol.* **2014**, 9, 676-681.
- [24] Molina-Sánchez, A.; Sangalli, D.; Hummer, K.; Marini, A.; Wirtz, L. *Phys. Rev. B* **2013**, 88, 045412.
- [25] Kośmider, K.; González, J. W.; Fernández-Rossier, J. *Phys. Rev. B* **2013**, 88, 245436.
- [26] Behnia, K. *Nat. nanotechnol.* **2012**, 7, 488.
- [27] Radisavljevic, B.; Radenovic, A.; Brivio, J.; Giacometti, i. V.; Kis, A. *Nat. nanotechnol.* **2011**, 6, 147-150.
- [28] Lee, C.; Yan, H.; Brus, L. E.; Heinz, T. F.; Hone, J.; Ryu, S. *ACS Nano* **2010**, 4, 2695-2700.
- [29] Novoselov, K. S.; Jiang, D.; Schedin, F.; Booth, T. J.; Khotkevich, V. V.; Morozov, S. V.; Geim, A. K. *Proc. Natl. Acad. Sci. U S A* **2005**, 102, 10451-3.

-
- [30] Splendiani, A.; Sun, L.; Zhang, Y.; Li, T.; Kim, J.; Chim, C. Y.; Galli, G.; Wang, F. *Nano Lett.* **2010**, 10, 1271-1275.
- [31] Zeng, H.; Dai, J.; Yao, W.; Xiao, D.; Cui, X. *Nat. Nanotechnol.* **2012**, 7, 490-493.
- [32] Wu, S.; Huang, C.; Aivazian, G.; Ross, J. S.; Cobden, D. H.; Xu, X. *ACS Nano* **2013**, 7, 2768-72.
- [33] Li, Y.; Rao, Y.; Mak, K. F.; You, Y.; Wang, S.; Dean, C. R.; Heinz, T. F. *Nano Lett.* **2013**, 13, 3329-3333.
- [34] Yin, Z.; Li, H.; Li, H.; Jiang, L.; Shi, Y.; Sun, Y.; Lu, G.; Zhang, Q.; Chen, X.; Zhang, H. *ACS Nano* **2012**, 6, 74-80.
- [35] Tsai, D. S.; Liu, K. K.; Lien, D. H.; Tsai, M. L.; Kang, C. F.; Lin, C. A.; Li, L. J.; He, J. H. *ACS Nano* **2013**, 7, 3905-3911.
- [36] Shanmugam, M.; Durcan, C. A.; Yu, B. *Nanoscale* **2012**, 4, 7399-7405.
- [37] Liu, K. K.; Zhang, W.; Lee, Y. H.; Lin, Y. C.; Chang, M. T.; Su, C. Y.; Chang, C. S.; Li, H.; Shi, Y.; Zhang, H.; Lai, C. S.; Li, L. J. *Nano Lett.* **2012**, 12, 1538-1544.
- [38] Wang, X.; Feng, H.; Wu, Y.; Jiao, L. *J. Am. Chem. Soc.* **2013**, 135, 5304-7.
- [39] Lee, Y. H.; Zhang, X. Q.; Zhang, W.; Chang, M. T.; Lin, C. T.; Chang, K. D.; Yu, Y. C.; Wang, J. T.; Chang, C. S.; Li, L. J.; Lin, T. W. *Adv. Mater.* **2012**, 24, 2320-2325.
- [40] Tsai, D. S.; Lien, D. H.; Tsai, M. L.; Su, S. H.; Chen, K. M.; Ke, J. J.; Yu, Y. C.; Li, L. J.; He, J. H. *Ieee Journal of Selected Topics in Quantum Electronics* **2014**, 20.
- [41] Najmaei, S.; Liu, Z.; Zhou, W.; Zou, X.; Shi, G.; Lei, S.; Yakobson, B. I.; Idrobo, J. C.; Ajayan, P. M.; Lou, J. *Nat. Mater.* **2013**, 12, 754-759.
- [42] van der Zande, A. M.; Huang, P. Y.; Chenet, D. A.; Berkelbach, T. C.; You, Y.; Lee, G. H.; Heinz, T. F.; Reichman, D. R.; Muller, D. A.; Hone, J. C. *Nat. Mater.* **2013**, 12, 554-561.

-
- [43] Li, S. L.; Miyazaki, H.; Song, H.; Kuramochi, H.; Nakaharai, S.; Tsukagoshi, K. *ACS Nano* **2012**, 6, 7381-7388.
- [44] Yu, Y.; Li, C.; Liu, Y.; Su, L.; Zhang, Y.; Cao, L. *Sci. rep.* **2013**, 3, 1866.
- [45] Yu, H.; Talukdar, D.; Xu, W.; Khurgin, J. B.; Xiong, Q. *Nano Lett.* **2015**, 15, 5653-5657.
- [46] Sze, S. M.; Lee, M. K. *Semiconductor devices, physics and technology*. 3rd ed.; Wiley: Hoboken, N.J., 2012; p ix, 578 p.
- [47] Lai, S. K.; Tang, L. B.; Hui, Y. Y.; Luk, C. M.; Lau, S. P. *J. Mater. Chem. C* **2014**, 2, 6971-6977.
- [48] Lopez-Sanchez, O.; Lembke, D.; Kayci, M.; Radenovic, A.; Kis, A. *Nat. Nanotechnol* **2013**, 8, 497-501.
- [49] Wang, Q. H.; Kalantar-Zadeh, K.; Kis, A.; Coleman, J. N.; Strano, M. S. *Nat. nanotechnol.* **2012**, 7, 699-712.
- [50] Sarkar, D.; Xie, X.; Kang, J.; Zhang, H.; Liu, W.; Navarrete, J.; Moskovits, M.; Banerjee, K. *Nano Lett.* **2015**, 15, 2852-2862.
- [51] Mak, K. F.; He, K.; Shan, J.; Heinz, T. F. *Nat. nanotechnol.* **2012**, 7, 494-498.
- [52] Zeng, H.; Dai, J.; Yao, W.; Xiao, D.; Cui, X. *Nat. nanotechnol.* **2012**, 7, 490-493.
- [53] Butun, S.; Tongay, S.; Aydin, K. *Nano Lett.* **2015**, 15, 2700-2704.
- [54] Lee, G.-H.; Yu, Y.-J.; Cui, X.; Petrone, N.; Lee, C.-H.; Choi, M. S.; Lee, D.-Y.; Lee, C.; Yoo, W. J.; Watanabe, K. *ACS nano* **2013**, 7, 7931-7936.
- [55] Bessonov, A. A.; Kirikova, M. N.; Petukhov, D. I.; Allen, M.; Ryhänen, T.; Bailey, M. *J. Nat. Mater.* **2015**, 14, 199.
- [56] Jariwala, D.; Sangwan, V. K.; Lauhon, L. J.; Marks, T. J.; Hersam, M. C. *ACS nano* **2014**, 8, 1102-1120.

-
- [57] Feng, Q.; Zhu, Y.; Hong, J.; Zhang, M.; Duan, W.; Mao, N.; Wu, J.; Xu, H.; Dong, F.; Lin, F. *Adv. Mater.* **2014**, 26, 2648-2653.
- [58] Lee, Y. H.; Zhang, X. Q.; Zhang, W.; Chang, M. T.; Lin, C. T.; Chang, K. D.; Yu, Y. C.; Wang, J. T. W.; Chang, C. S.; Li, L. J. *Adv. Mater.* **2012**, 24, 2320-2325.
- [59] Schmidt, H.; Wang, S.; Chu, L.; Toh, M.; Kumar, R.; Zhao, W.; Castro Neto, A.; Martin, J.; Adam, S.; Özyilmaz, B. *Nano Lett.* **2014**, 14, 1909-1913.
- [60] Yin, X.; Ye, Z.; Chenet, D. A.; Ye, Y.; O'Brien, K.; Hone, J. C.; Zhang, X. *Science* **2014**, 344, 488-490.
- [61] Malard, L. M.; Alencar, T. V.; Barboza, A. P. M.; Mak, K. F.; de Paula, A. M. *Phys. Rev. B* **2013**, 87, 201401.
- [62] Li, Y.; Rao, Y.; Mak, K. F.; You, Y.; Wang, S.; Dean, C. R.; Heinz, T. F. *Nano letters* **2013**, 13, 3329-3333.
- [63] Kumar, N.; Najmaei, S.; Cui, Q.; Ceballos, F.; Ajayan, P. M.; Lou, J.; Zhao, H. *Physical Review B* **2013**, 87, 161403.
- [64] Trolle, M. L.; Seifert, G.; Pedersen, T. G. *Phys. Rev. B* **2014**, 89, 235410.
- [65] Zhang, L.; Liu, K.; Wong, A. B.; Kim, J.; Hong, X.; Liu, C.; Cao, T.; Louie, S. G.; Wang, F.; Yang, P. *Nano Lett.* **2014**, 14, 6418-6423.
- [66] Jones, R. J.; Ye, J. *Opt. Lett.* **2002**, 27, 1848-1850.
- [67] Paschotta, R.; Fiedler, K.; Kürz, P.; Mlynek, J. *Appl. Phys. B* **1994**, 58, 117-122.
- [68] Smith, R. *IJQE* **1970**, 6, 215-223.
- [69] Nemes-Incze, P.; Osváth, Z.; Kamarás, K.; Biró, L. *Carbon* **2008**, 46, 1435-1442.
- [70] Lee, C.; Yan, H.; Brus, L. E.; Heinz, T. F.; Hone, J.; Ryu, S. *ACS nano* **2010**, 4, 2695-2700.
- [71] Wu, S.; Huang, C.; Aivazian, G.; Ross, J. S.; Cobden, D. H.; Xu, X. *ACS Nano* **2013**,

7, 2768-2772.

[72] Conley, H. J.; Wang, B.; Ziegler, J. I.; Haglund Jr, R. F.; Pantelides, S. T.; Bolotin, K. I. *Nano Lett.* **2013**, 13, 3626-3630.

[73] Kim, D. H.; Lim, D. *J. Korean Phys. Soc.* **2015**, 66, 816-820.

[74] Lu, X.; Utama, M. I.; Lin, J.; Gong, X.; Zhang, J.; Zhao, Y.; Pantelides, S. T.; Wang, J.; Dong, Z.; Liu, Z.; Zhou, W.; Xiong, Q. *Nano Lett.* **2014**, 14, 2419-2425.

[75] Bloembergen, N.; Pershan, P. *Phys. Rev.* **1962**, 128, 606.

[76] Shen, Y. *ARPC* **1989**, 40, 327-350.

[77] Hopfield, J.; Thomas, D. *Phys. Rev.* **1963**, 132, 563.

[78] Boyd, R. W. *Nonlinear optics*. Academic press: 2003.

[79] Wang, Q. H.; Kalantar-Zadeh, K.; Kis, A.; Coleman, J. N.; Strano, M. S. *Nat. Nanotechnol.* **2012**, 7, 699-712.

[80] Wilson, J. A.; Yoffe, A. D. *Adv. Phys.* **1969**, 18, 193-335.

[81] Splendiani, A.; Sun, L.; Zhang, Y.; Li, T.; Kim, J.; Chim, C. Y.; Galli, G.; Wang, F. *Nano lett.* **2010**, 10, 1271-1275.

[82] Mak, K. F.; Lui, C. H.; Shan, J.; Heinz, T. F. *Phys. Rev. Lett.* **2009**, 102, 256405.

[83] Cao, L. *Mater. Res. Bull.* **2015**, 40, 592-599.

[84] Janisch, C.; Wang, Y.; Ma, D.; Mehta, N.; Elias, A. L.; Perea-Lopez, N.; Terrones, M.; Crespi, V.; Liu, Z. *Sci. Rep.* **2014**, 4, 5530.

[85] Malard, L. M.; Alencar, T. V.; Barboza, A. P. M.; Mak, K. F.; de Paula, A. M. *Phys. Rev. B* **2013**, 87, 201401(R).

[86] Kim, D. H.; Lim, D. *J. Korean Phys. Soc.* **2015**, 66, 816-820.

[87] Li, Y.; Rao, Y.; Mak, K. F.; You, Y.; Wang, S.; Dean, C. R.; Heinz, T. F. *Nano lett.* **2013**, 13, 3329-3333.

-
- [88] Kumar, N.; Najmaei, S.; Cui, Q. N.; Ceballos, F.; Ajayan, P. M.; Lou, J.; Zhao, H. *Phys. Rev. B* **2013**, 87.
- [89] Clark, D. J.; Senthilkumar, V.; Le, C. T.; Weerawarne, D. L.; Shim, B.; Jang, J. I.; Shim, J. H.; Cho, J.; Sim, Y.; Seong, M. J.; Rhim, S. H.; Freeman, A. J.; Chung, K. H.; Kim, Y. S. *Phys. Rev. B* **2014**, 90.
- [90] Lopez-Sanchez, O.; Lembke, D.; Kayci, M.; Radenovic, A.; Kis, A. *Nat. Nanotechnol.* **2013**, 8, 497-501.
- [91] Mak, K. F.; He, K.; Shan, J.; Heinz, T. F. *Nat. Nanotechnol.* **2012**, 7, 494-498.
- [92] Zeng, H.; Dai, J.; Yao, W.; Xiao, D.; Cui, X. *Nat. Nanotechnol.* **2012**, 7, 490-493.
- [93] Clark, D. J.; Le, C. T.; Senthilkumar, V.; Ullah, F.; Cho, H.-Y.; Sim, Y.; Seong, M.-J.; Chung, K.-H.; Kim, Y.; Jang, J. *Appl. Phys. Lett.* **2015**, 107, 131113.
- [94] Liu, N.; Kim, P.; Kim, J. H.; Ye, J. H.; Kim, S.; Lee, C. J. *ACS Nano* **2014**, 8, 6902-6910.
- [95] Wang, X.; Gong, Y.; Shi, G.; Chow, W. L.; Keyshar, K.; Ye, G.; Vajtai, R.; Lou, J.; Liu, Z.; Ringe, E.; Tay, B. K.; Ajayan, P. M. *ACS Nano* **2014**, 8, 5125-5131.
- [96] Shaw, J. C.; Zhou, H. L.; Chen, Y.; Weiss, N. O.; Liu, Y.; Huang, Y.; Duan, X. F. *Nano Res.* **2014**, 7, 511-517.
- [97] Kang, K.; Xie, S.; Huang, L.; Han, Y.; Huang, P. Y.; Mak, K. F.; Kim, C.-J.; Muller, D.; Park, J. *Nature* **2015**, 520, 656-660.
- [98] Tsirlina, T.; Feldman, Y.; Homyonfer, M.; Sloan, J.; Hutchison, J.; Tenne, R. *Fullerene Sci. Technol.* **1998**, 6, 157-165.
- [99] Wu, W.; Wang, L.; Li, Y.; Zhang, F.; Lin, L.; Niu, S.; Chenet, D.; Zhang, X.; Hao, Y.; Heinz, T. F. *Nature* **2014**, 514, 470.
- [100] Rhim, S.; Freeman, A. *Appl. Phys. Lett.* **2015**, 107, 241908.

-
- [101] Wang, G.; Gerber, I.; Bouet, L.; Lagarde, D.; Balocchi, A.; Vidal, M.; Palleau, E.; Amand, T.; Marie, X.; Urbaszek, B. *2D Materials* **2015**, 2, 045005.
- [102] Tongay, S.; Zhou, J.; Ataca, C.; Lo, K.; Matthews, T. S.; Li, J.; Grossman, J. C.; Wu, J. *Nano Lett.* **2012**, 12, 5576-5580.
- [103] Lu, X.; Utama, M. I. B.; Lin, J.; Gong, X.; Zhang, J.; Zhao, Y.; Pantelides, S. T.; Wang, J.; Dong, Z.; Liu, Z. *Nano Lett.* **2014**, 14, 2419-2425.
- [104] Ross, J. S.; Wu, S.; Yu, H.; Ghimire, N. J.; Jones, A. M.; Aivazian, G.; Yan, J.; Mandrus, D. G.; Xiao, D.; Yao, W.; Xu, X. *Nat. Commun.* **2013**, 4, 1474.
- [105] Ugeda, M. M.; Bradley, A. J.; Shi, S.-F.; Felipe, H.; Zhang, Y.; Qiu, D. Y.; Ruan, W.; Mo, S.-K.; Hussain, Z.; Shen, Z.-X. *Nat. Mater.* **2014**, 1091-1095.
- [106] MacNeill, D.; Heikes, C.; Mak, K. F.; Anderson, Z.; Kormanyos, A.; Zolyomi, V.; Park, J.; Ralph, D. C. *Phys. Rev. Lett.* **2015**, 114, 037401.
- [107] Wang, K.; Wang, J.; Fan, J.; Lotya, M.; O'Neill, A.; Fox, D.; Feng, Y.; Zhang, X.; Jiang, B.; Zhao, Q. *ACS nano* **2013**, 7, 9260-9267.
- [108] Zhang, H.; Lu, S.; Zheng, J.; Du, J.; Wen, S.; Tang, D.; Loh, K. *Opt. Express* **2014**, 22, 7249-7260.
- [109] Boyd, R. W. **2008**.
- [110] Bloembergen, N. *IEEE J. Quantum Electron. QE* **1974**, 10, 375-386.
- [111] Holway Jr, L. H.; Fradin, D. *J. Appl. Phys.* **1975**, 46, 279-291.
- [112] Sparks, M.; Mills, D.; Warren, R.; Holstein, T.; Maradudin, A.; Sham, L.; Loh Jr, E.; King, D. *Phys. Rev. B* **1981**, 24, 3519.
- [113] Brant, J. A.; Clark, D. J.; Kim, Y. S.; Jang, J. I.; Weiland, A.; Aitken, J. A. *Inorg. Chem.* **2015**, 54, 2809-2819.
- [114] Yan, R.; Simpson, J. R.; Bertolazzi, S.; Brivio, J.; Watson, M.; Wu, X.; Kis, A.; Luo,

-
- T.; Hight Walker, A. R.; Xing, H. G. *ACS nano* **2014**, 8, 986-993.
- [115] Dempsey, W. P.; Fraser, S. E.; Pantazis, P. *Bioessays* **2012**, 34, 351-360.
- [116] Fine, S.; Hansen, W. P. *Appl. Opt.* **1971**, 10, 2350-2353.
- [117] Wang, Q. H.; Kalantar-Zadeh, K.; Kis, A.; Coleman, J. N.; Strano, M. S. *Nat. nanotechnol.* **2012**, 7, 699-712.
- [118] Mak, K. F.; Lee, C.; Hone, J.; Shan, J.; Heinz, T. F. *Phys. Rev. Lett.* **2010**, 105, 136805.
- [119] Clark, D.; Le, C.; Senthilkumar, V.; Ullah, F.; Cho, H.-Y.; Sim, Y.; Seong, M.-J.; Chung, K.-H.; Kim, Y.; Jang, J. *Appl. Phys. Lett.* **2015**, 107, 131113.
- [120] Le, C. T.; Clark, D. J.; Ullah, F.; Senthilkumar, V.; Jang, J. I.; Sim, Y.; Seong, M. J.; Chung, K. H.; Park, H.; Kim, Y. S. *Ann. Phys. (Berl.)* **2016**.
- [121] Janisch, C.; Wang, Y. X.; Ma, D.; Mehta, N.; Elias, A. L.; Perea-Lopez, N.; Terrones, M.; Crespi, V.; Liu, Z. W. *Sci. Rep.* **2014**, 4.
- [122] Kang, J.; Tongay, S.; Li, J. B.; Wu, J. Q. *J Appl Phys* **2013**, 113, 143703.
- [123] Wang, C. Y.; Guo, G. Y. *J. Phys. Chem. C* **2015**, 119, 13268-13276.
- [124] Paradisanos, I.; Kymakis, E.; Fotakis, C.; Kioseoglou, G.; Stratakis, E. *Appl. Phys. Lett.* **2014**, 105.
- [125] Seyler, K. L.; Schaibley, J. R.; Gong, P.; Rivera, P.; Jones, A. M.; Wu, S. F.; Yan, J. Q.; Mandrus, D. G.; Yao, W.; Xu, X. D. *Nat. nanotechnol.* **2015**, 10, 407-411.
- [126] Feng, Q.; Mao, N.; Wu, J.; Xu, H.; Wang, C.; Zhang, J.; Xie, L. *ACS Nano* **2015**, 9, 7450-7455.
- [127] Li, H.; Duan, X.; Wu, X.; Zhuang, X.; Zhou, H.; Zhang, Q.; Zhu, X.; Hu, W.; Ren, P.; Guo, P.; Ma, L.; Fan, X.; Wang, X.; Xu, J.; Pan, A.; Duan, X. *J. Am. Chem. Soc.* **2014**, 136, 3756-9.

-
- [128] Zhang, M.; Wu, J. X.; Zhu, Y. M.; Dumcenco, D. O.; Hong, J. H.; Mao, N. N.; Deng, S. B.; Chen, Y. F.; Yang, Y. L.; Jin, C. H.; Chaki, S. H.; Huang, Y. S.; Zhang, J.; Xie, L. M. *ACS Nano* **2014**, 8, 7130-7137.
- [129] Jadczyk, J.; Dumcenco, D. O.; Huang, Y. S.; Lin, Y. C.; Suenaga, K.; Wu, P. H.; Hsu, H. P.; Tiong, K. K. *J. Appl. Phys.* **2014**, 116.
- [130] Su, S.-H.; Hsu, W.-T.; Hsu, C.-L.; Chen, C.-H.; Chiu, M.-H.; Lin, Y.-C.; Chang, W.-H.; Suenaga, K.; He Jr, -. H.; Li, L.-J. *Front. in Energy Res.* **2014**, 2, 27.
- [131] Gong, Y.; Liu, Z.; Lupini, A. R.; Shi, G.; Lin, J.; Najmaei, S.; Lin, Z.; Elías, A. L.; Berkdemir, A.; You, G. *Nano Lett.* **2013**, 14, 442-449.
- [132] Kang, J.; Tongay, S.; Li, J.; Wu, J. *J. Appl. Phys.* **2013**, 113, 143703.
- [133] Clark, D. J.; Senthilkumar, V.; Le, C. T.; Weerawarne, L.; Shim, B.; Jang, J. I.; Shim, J. H.; Cho, J.; Sim, Y.; Seong, M. J.; Rhim, S. H.; Freeman, A. J.; Chung, K. H.; Kim, Y. S. *Phys. Rev. B* **2015**, 92.
- [134] Clark, D.; Senthilkumar, V.; Le, C.; Weerawarne, D.; Shim, B.; Jang, J.; Shim, J.; Cho, J.; Sim, Y.; Seong, M.-J. *Phys. Rev. B* **2014**, 90, 121409.
- [135] Yoshida, S.; Kobayashi, Y.; Sakurada, R.; Mori, S.; Miyata, Y.; Mogi, H.; Koyama, T.; Takeuchi, O.; Shigekawa, H. *Sci. Rep.* **2015**, 5.
- [136] Huang, S. X.; Ling, X.; Liang, L. B.; Kong, J.; Terrones, H.; Meunier, V.; Dresselhaus, M. S. *Nano Lett.* **2014**, 14, 5500-5508.
- [137] Chen, Y.; Xi, J.; Dumcenco, D. O.; Liu, Z.; Suenaga, K.; Wang, D.; Shuai, Z.; Huang, Y.-S.; Xie, L. *ACS Nano* **2013**, 7, 4610-4616.
- [138] Echeverry, J.; Urbaszek, B.; Amand, T.; Marie, X.; Gerber, I. *Phys. Rev. B* **2016**, 93, 121107.
- [139] Dmitriev, V. G.; Gurzadyan, G. G.; Nikogosyan, D. N. *Handbook of nonlinear*

optical crystals. Springer: 2013; Vol. 64.

- [140] Jackson, A.; Ohmer, M.; LeClair, S. *Infrared Phys. Technol.* **1997**, 38, 233-244.
- [141] Hsu, W.-T.; Chen, Y.-L.; Chen, C.-H.; Liu, P.-S.; Hou, T.-H.; Li, L.-J.; Chang, W.-H. *Nature communications* **2015**, 6.
- [142] Ye, Y.; Xiao, J.; Wang, H.; Ye, Z.; Zhu, H.; Zhao, M.; Wang, Y.; Zhao, J.; Yin, X.; Zhang, X. *Nat. nanotechnol.* **2016**, 11, 598-602.
- [143] Kim, C.-J.; Brown, L.; Graham, M. W.; Hovden, R.; Havener, R. W.; McEuen, P. L.; Muller, D. A.; Park, J. *Nano Lett.* **2013**, 13, 5660-5665.
- [144] Paradisanos, I.; Kymakis, E.; Fotakis, C.; Kioseoglou, G.; Stratakis, E. *Appl. Phys. Lett.* **2014**, 105, 041108.
- [145] Zhu, B.; Chen, X.; Cui, X. *Sci. Rep.* **2015**, 5.
- [146] Hill, H. M.; Rigosi, A. F.; Roquelet, C.; Chernikov, A.; Berkelbach, T. C.; Reichman, D. R.; Hybertsen, M. S.; Brus, L. E.; Heinz, T. F. *Nano Lett.* **2015**, 15, 2992-2997.
- [147] Xiao, J.; Ye, Z.; Wang, Y.; Zhu, H.; Wang, Y.; Zhang, X. *Light: Sci. Appl.* **2015**, 4, e366.
- [148] Wang, G.; Marie, X.; Gerber, I.; Amand, T.; Lagarde, D.; Bouet, L.; Vidal, M.; Balocchi, A.; Urbaszek, B. *Phys. Rev. Lett.* **2015**, 114, 097403.
- [149] Le, C. T.; Clark, D. J.; Ullah, F.; Senthilkumar, V.; Jang, J. I.; Sim, Y.; Seong, M. J.; Chung, K. H.; Park, H.; Kim, Y. S. *Ann. Phys. (Berlin)* **2016**, 528, 551-559.
- [150] Le, C. T.; Clark, D. J.; Ullah, F.; Jang, J. I.; Senthilkumar, V.; Sim, Y.; Seong, M.-J.; Chung, K.-H.; Kim, J. W.; Park, S. *ACS Photonics* **2016**, 4, 38-44.
- [151] Wan, Y.; Zhang, H.; Zhang, K.; Wang, Y.; Sheng, B.; Wang, X.; Dai, L. *ACS Appl. Mater. Interfaces* **2016**, 8, 18570-18576.
- [152] Feng, Q.; Mao, N.; Wu, J.; Xu, H.; Wang, C.; Zhang, J.; Xie, L. *ACS nano* **2015**, 9,

7450-7455.

[153] Gong, Y.; Lin, J.; Wang, X.; Shi, G.; Lei, S.; Lin, Z.; Zou, X.; Ye, G.; Vajtai, R.; Yakobson, B. I. *Nat. Mater.* **2014**, 13, 1135-1142.

[154] Li, H.; Zhang, Q.; Yap, C. C. R.; Tay, B. K.; Edwin, T. H. T.; Olivier, A.; Baillargeat, D. *Adv. Funct. Mater.* **2012**, 22, 1385-1390.

[155] Nemes-Incze, P.; Osvath, Z.; Kamaras, K.; Biro, L. P. *Carbon* **2008**, 46, 1435-1442.

[156] Wang, K.; Huang, B.; Tian, M.; Ceballos, F.; Lin, M.-W.; Mahjouri-Samani, M.; Boulesbaa, A.; Poretzky, A. A.; Rouleau, C. M.; Yoon, M. *ACS nano* **2016**, 10, 6612-6622.

[157] Huang, S.; Ling, X.; Liang, L.; Kong, J.; Terrones, H.; Meunier, V.; Dresselhaus, M. S. *Nano lett.* **2014**, 14, 5500-5508.

[158] Clark, D. J.; Le, C. T.; Senthilkumar, V.; Ullah, F.; Cho, H. Y.; Sim, Y.; Seong, M. J.; Chung, K. H.; Kim, Y. S.; Jang, J. I. *Appl. Phys. Lett.* **2015**, 107.

[159] Zhao, M.; Ye, Z.; Suzuki, R.; Ye, Y.; Zhu, H.; Xiao, J.; Wang, Y.; Iwasa, Y.; Zhang, X. *Light: Sci. Appl.* **2016**, 5, 16131.